AFRL-AFOSR-VA-TR-2021-0072

Characterizing Dusty Plasmas Formed by Hypervelocity Impacts Through Experiments and Particle-In-Cell (PIC) Simulations

Close, Sigrid
LELAND STANFORD JUNIOR UNIVERSITY
450 SERRA MALL
STANFORD, CA,
US

07/12/2021
Final Technical Report

Air Force Research Laboratory
Air Force Office of Scientific Research
Arlington, Virginia 22203
Air Force Materiel Command

REPORT DOCUMENTATION PAGE

Form Approved
OMB No. 0704-0188

1. REPORT DATE *(DD-MM-YYYY)*	**2. REPORT TYPE**	**3. DATES COVERED** *(From - To)*
12-07-2021	Final	15 Jan 2018 - 14 Jan 2021

4. TITLE AND SUBTITLE
Characterizing Dusty Plasmas Formed by Hypervelocity Impacts Through Experiments and Particle-In-Cell (PIC) Simulations

5a. CONTRACT NUMBER

5b. GRANT NUMBER
FA9550-18-1-0117

5c. PROGRAM ELEMENT NUMBER

6. AUTHOR(S)
Sigrid Close

5d. PROJECT NUMBER

5e. TASK NUMBER

5f. WORK UNIT NUMBER

7. PERFORMING ORGANIZATION NAME(S) AND ADDRESS(ES)
LELAND STANFORD JUNIOR UNIVERSITY
450 SERRA MALL
STANFORD, CA
US

8. PERFORMING ORGANIZATION REPORT NUMBER

9. SPONSORING/MONITORING AGENCY NAME(S) AND ADDRESS(ES)
AF Office of Scientific Research
875 N. Randolph St. Room 3112
Arlington, VA 22203

10. SPONSOR/MONITOR'S ACRONYM(S)
AFRL/AFOSR RTB1

11. SPONSOR/MONITOR'S REPORT NUMBER(S)
AFRL-AFOSR-VA-TR-2021-0072

12. DISTRIBUTION/AVAILABILITY STATEMENT
A Distribution Unlimited: PB Public Release

13. SUPPLEMENTARY NOTES

14. ABSTRACT
One component of the space environment that has yet to be fully understood is the plasma that forms when a hypervelocity particle, such as a meteoroid or piece of space debris, impacts a spacecraft. Plasma is generated both from thermal ionization and from pressure ionization and can range from weakly to fully ionized, depending on the particle's velocity. Because the plasma density within the impact crater is on the same order of magnitude as the number density of the solid target, this type of matter is called warm dense matter (WDM) or non-ideal plasma. This plasma can also contain a dust component, which is particularly relevant for the lower-velocity range of hypervelocity impacts. We
probed the complex behavior of dusty impact plasma to understand the interaction of radiation with matter and the effect of the space environment on systems and sensors. We developed models to characterize the dusty plasma, and executed an impact experiment at a light-gas gun facility. The primary motivation for this research is to provide significant advances in our knowledge of dusty hypervelocity impact plasmas, which are a key component of the space environment.

15. SUBJECT TERMS

16. SECURITY CLASSIFICATION OF:			**17. LIMITATION OF ABSTRACT**	**18. NUMBER OF PAGES**	**19a. NAME OF RESPONSIBLE PERSON**
a. REPORT	**b. ABSTRACT**	**c. THIS PAGE**			JULIE MOSES
U	U	U	UU	100	**19b. TELEPHONE NUMBER** *(Include area code)* 426-9586

Standard Form 298 (Rev.8/98)
Prescribed by ANSI Std. Z39.18

Characterizing Dusty Plasmas Formed by Hypervelocity Impacts Through Experiments and Particle-In-Cell (PIC) Simulations

Final report: AFOSR grant FA9550-18-1-0117

Sigrid Close (PI)
Nicolas Lee, Benjamin Estacio
Isaac Matthews, Gil Shohet, Sean Young

Space Environment and Satellite Systems
Dept. of Aeronautics and Astronautics
496 Lomita Mall
Stanford University
Stanford, CA 94305-4035
sess.stanford.edu
June 18, 2021

Abstract

One component of the space environment that has yet to be fully understood is the plasma that forms when a hypervelocity particle, such as a meteoroid or piece of space debris, impacts a spacecraft. Plasma is generated both from thermal ionization and from pressure ionization and can range from weakly to fully ionized, depending on the particle's velocity. Because the plasma density within the impact crater is on the same order of magnitude as the number density of the solid target, this type of matter is called warm dense matter (WDM) or non-ideal plasma. This plasma can also contain a dust component, which is particularly relevant for the lower-velocity range of hypervelocity impacts. We probed the complex behavior of dusty impact plasma to understand the interaction of radiation with matter and the effect of the space environment on systems and sensors. We developed models to characterize the dusty plasma, and executed an impact experiment at a light-gas gun facility. The primary motivation for this research is to provide significant advances in our knowledge of dusty hypervelocity impact plasmas, which are a key component of the space environment.

Contents

1 Introduction

Within the space environment lie complex plasmas with a wide range of densities and temperatures that can have profound impacts on satellite survivability and operations. Well known deleterious effects of space environment interactions include geomagnetic activity that can interfere with satellite-to-ground communications, high-energy particles that can cause single event upsets in onboard logic systems or deep dielectric discharges, and the ambient plasma that can cause potential differences between external surfaces resulting in discharges. Notably, one component of the space environment that has yet to be fully understood is the plasma that forms when a hypervelocity particle, such as a meteoroid or piece of space debris, impacts a spacecraft. Plasma is generated both from thermal ionization and from pressure ionization and can range from weakly to fully ionized, depending on the particle's velocity. Because the plasma density within the impact crater is on the same order of magnitude as the number density of the solid target, this type of matter is called warm dense matter (WDM) or non-ideal plasma. This plasma can also contain a dust component, which is particularly relevant for the lower-velocity range of hypervelocity impacts. Therefore, the threat from these plasmas cannot be fully characterized without considering dusty plasma effects, which are ubiquitous but poorly understood.

1.1 Project goals

Unlike previous work where the plume was fully vaporized, this project studies hypervelocity impacts that produce a large amount of initially neutral macro-ejecta, referred to as dust, that then gains a charge from collisions with the plasma. We theorize that this dust component can significantly affect the properties of the plasma, and therefore RF emission, through the creation of a so-called "dusty plasma". In order to produce impacts that contain a significant dust component in the plume, more massive impactors, on the order of 1 mg in mass, were used. To produce hypervelocity impacts using these larger impactors, a two-stage light gas gun was utilized. The vacuum facilities for this gun had a non-negligible background gas at pressures of ≥ 0.5 Torr. Impacts using light gas guns with similar background pressures have been studied [16, 34, 45, 47], but none focused on the interaction between impact-produced dust and plasma. The background pressure of the chamber in the experiments is orders of magnitude higher than the vacuum of space. As such, to understand how produced dust influences hypervelocity impact plume dynamics and associated RF emission in space, the gas dynamics, and any influence they have on RF emission, need to be resolved.

There are a number of unknowns when it comes to hypervelocity impacts and the effects they can have. The goal of this research is to push forward the state of the art of the understanding of hypervelocity impacts. Primarily this research is focused on experimentally producing a hypervelocity impact with dust content and characterizing the effect of the dust. This includes designing sensors to make measurements, analyzing data, and performing simulations to better understand the system. As will be shown, this also requires an understanding of how the experimental conditions influenced the results. Secondly, this research aims to continue to work towards understanding the threat hypervelocity impacts pose to spacecraft. Mainly this is about the EMP that is produced, understanding how it is produced, and what threat is poses. The EMP is not the only means by

which this impacts pose a threat though and it is worth characterizing other dangers to spacecraft such as dangers from dust.

1.2 Major results

The major results include design and development of new RF, plasma and witness plate sensors, including an RF sensor designed to characterize the polarization of the emitted radiation, a Faraday cup to capture the distribution of charge the expanding plasma plume, and witness plates to characterize the dust distribution. These sensors were deployed in a light gas gun experiment at NASA Ames, which was funded through this research. We also developed new models, including an orbital motion limited (OML) model, as well as fluid and plasma models. Our major findings include the following:

1. The background gas slowed the expanding plasma plume from approximately 16 km/s to 10 km/s, which resulted in generation of a Rayleigh-Taylor instability. Using high-speed imagery, we found that the expanding, charged dust ring pulled the plasma, causing the plasma duration to increase by a factor of 10. The dusty plasma was highly negative with current densities up to 0.1 A/m^2, which is 1000 times denser than previously predicted. This has profound implications for spacecraft safety due to RF emission from dusty plasmas.

2. The dust distribution for regolith simulant followed power law with a D-value of 1.69, which is in agreement with results from disruption studies on solid basalt. We observed a transition with increasing ejecta size from circular to more irregular shapes, which provides information about the phase of the material.

3. Through extension of the OML theory, we were able to characterize the evolution of ejecta interactions with the background, accounting for physical terms important in high energy density environments, such as thermionic emission and radiation. The model outputs the charge, momentum, energy and mass flux across a range of physical regimes spanned by the expanding plasma.

The publications and presentations resulting from this research are the following:

- Lee, N. (2019) Meteoroid impact plasma and atmospheric density, *CEDAR Workshop*, Santa Fe, NM, 21 Jun.

- Lee, N. (2019), Meteoroids, impact plasma, and atmospheric density, special seminar, Jicamarca Radio Observatory, Lima, Peru, 10 Oct.

- Young, S. A. Q., Close, S., and Lee N. (2019), The Space Environmental Electrical Power Subsystem (SEEPS): Energy Harvesting Supporting Microsatellite Exploration of the Outer Solar System, *presented at 70th International Astronautical Congress*, Washington, DC, 21—25 Oct.

- Estacio, B., Lee, N., Shohet, G., Young, S. A. Q., Matthews, I., Bassette, R., Banerjee, S., and Close, S. (2019), Characterization of the Plasma Plume Produced by Dust and Meteoroid Impact of Different Materials, Abstract P21B-07, presented at *2019 Fall Meeting*, AGU, San Francisco, CA, 9–13 Dec.

- Matthews, I., Lee, N., Shohet, G., Young, S. A. Q., Bassette, R., Banerjee, S., Szybunka, H., and Close, S. (2019), Characterization of Optical Emission from Ground-Based Hypervelocity Impact Experiments, Abstract P23C-3518, presented at *2019 Fall Meeting*, AGU, San Francisco, CA, 9–13 Dec.

- Shohet, G., Lee, N., Estacio, B., Matthews, I., Young, S. A. Q., Bassette, R., Banerjee, S., and Close, S. (2019), Dusty plasma effects in hypervelocity impacts on the ground and in space, Abstract P23C-3519, presented at *2019 Fall Meeting*, AGU, San Francisco, CA, 9–13 Dec.

- Young, S. A. Q., Lee, N., Estacio, B., Matthews, I., Shohet, G., Bassette, R., Banerjee, S., and Close, S. (2019), Electric Field Polarization of Electromagnetic Radiation from Micrometeoroid and Dust Impacts on Spacecraft, Abstract P23C-3520, presented at *2019 Fall Meeting*, AGU, San Francisco, CA, 9–13 Dec.

- Estacio, B. and S. Close (2020), Dust and atmospheric effects on light gas gun hypervelocity impact experiments, *XXXIII URSI General Assembly and Scientific Symposium*, Rome, Italy, 29 Aug–05 Sep.

- Shohet, G., N. Lee, and S. Close (2020), Dust charge modeling and ejecta measurements for hypervelocity impacts on aluminum and powdered regolith simulant targets, *XXXIII URSI General Assembly and Scientific Symposium*, Rome, Italy, 29 Aug–05 Sep.

- Young, S., N. Lee, and S. Close (2020), Harvesting electromagnetic energy from hypervelocity impacts for solar system exploration, *XXXIII URSI General Assembly and Scientific Symposium*, Rome, Italy, 29 Aug–05 Sep.

- Shohet, G., Estacio, B., Young, S. A. Q., Matthews, I., Lee, N., Close, S. (2020), Ejecta charging and dynamics in meteoroid impacts on asteroids and comets, Abstract P015-0008, presented at *2020 Fall Meeting*, AGU, virtual, 1–17 Dec.

- Estacio, B. et al. (2020), Dust and atmospheric influence on plasma properties observed in light gas gun hypervelocity impact experiments, *International Journal of Impact Engineering*, 151, 103833.

- Shohet, G., Estacio, B., Matthews, I., Young, S. A. Q., Lee, N., and Close, S. (2021), Microscopic ejecta measurements from hypervelocity impacts on aluminum and powdered regolith targets, *International Journal of Impact Engineering*, 152, 103840.

Finally, this award supported 2 masters research projects, 3 PhD theses, including Ben Estacio, who was directly supported by this award, as well as Sean Young and Gil Shohet, who used the data from the experiment that was funded by this award. Ben Estacio also received 3rd place in the International URSI Student Paper Competition. The PhD theses include the following:

- Ben Estacio, "Characterizing Dusty Hypervelocity Impact Plasma Plume Dynamics and Effects", 2021.

- Gil Shohet, "Dusty Plasma Effects in Hypervelocity Impacts", 2021.

- Sean Young, "Harnessing Energy in the Space Environment for Spacecraft Operations", 2021.

2 Experimental campaign

We executed an experimental campaign in early 2019 to study the production of dust on various impact materials and to characterize its effect on the expanding plasma plume. This chapter describes the facility used to conduct these experiments, the impact targets and environmental conditions at the facility, and the sensors deployed to observe the impact events.

2.1 Facility

The Ames Vertical Gun Range (AVGR) in Moffett Field, California, uses a light-gas gun to launch projectiles at speeds ranging from 0.5 to 7 km/s. Single projectiles can range from 1.5 to 6.4 mm diameter, or clusters of smaller projectiles can be launched simultaneously, corresponding to typical space debris speeds and sizes. Projectiles are typically metallic or glass, and are launched into a vacuum chamber approximately 2.5 m in diameter. The chamber can be evacuated to 0.1 Torr, corresponding to a mean free path on the order of 1 mm. These parameters allow for a dusty, collisional plasma.

2.1.1 Targets and Conditions

During the experimental campaign the chamber pressure, projectile size, and projectile velocity were kept as constant as possible, in order to examine plasma properties as a function of target material and bias. The projectiles were approximately 1.6 mm diameter aluminum spheres. All targets were impacted with shots normal to their surface, or 90° from the horizontal. The shots used for data in this paper are summarized in Table 2.1 where mass refers to the projectile mass. Shot 0 was a preliminary test without the full suite. As such, only camera data will be discussed from this shot. Aluminum was chosen as the baseline target due to its high temperature and pressure behavior, such as its Hugoniot curve and conductivity, being well characterized. This is especially the case in comparison to higher Z materials or materials consisting of multiple elements. Tungsten was chosen due to its high potential for charge production on impact. The other materials were selected to represent spacecraft materials or an asteroid surface in the case of the regolith simulant target of dolomite ($CaMg(CO_3)_2$) and azomite ($NaK_2Ca_5Al_3Si_{21}O_{70} \cdot 6H_2O$).

Table 2.1: Shot summary for the experimental campaign at AVGR.

Shot	Material	Bias (V)	Mass (mg)	Pressure (Torr)	Speed (km/s)
0	Cu	Float	6	.49	3.96
1	Al	0V	5.8	.67	4.38
2	Al	0V	5.9	.69	5.38
3	Al	+50	5.6	.5	5.88
4	Al	+300	6	.54	5.19
5	Al	-50	5.9	.54	4.97
6	Al	-100	5.8	.58	5.38
7	Al	-300	6	.55	5.41
8	Cu	0V	5.9	.56	5.09
9	W	0V	5.9	.55	5.46
10	Al	-300	5.9	.52	5.44
11	FR4	0V	5.9	.54	5.66
12	Dolomite and Azomite	0V	5.9	.49	5.56
13	Glass	0V	5.9	.52	5.59

All targets were mounted with countersunk bolts so as to not impede the expansion of the plasma with mounting hardware. Metallic targets, other than shot 0 which was 1 mm thick, were 5 $\times$ 5 cm with thicknesses between 0.635 and 1 cm. FR4 — the glass epoxy found on printed circuit boards — also had a target area of 5 $\times$ 5 cm but was 1.27 cm thick. The Dolomite and Azomite shot used a container that had a diameter of 10 cm and a depth of 5 cm. Finally, the glass was 6 $\times$ 11.5 cm with a depth of 2 cm. Except for shot 0, these dimensions were all chosen such that the targets could be approximated as semi-infinite.

Target charging between $\pm$50 V and $\pm$300 V was applied using aluminum targets to simulate various levels of spacecraft charging. This was accomplished by applying a voltage relative to the chamber walls on a 0.46 m diameter circular plate surrounding the target by means of a high voltage supply through an RC circuit, creating an approximately uniform electric field around the target. The data and observations from these shots will be presented in the next chapter.

2.2 Sensors

We have designed a sensor suite to take simultaneous measurements of the impact event over a wide spectrum to fully characterize the event. High-speed cameras are used to characterize the dust component through spatial and temporal measurements. Plasma sensors are used to make a direct measurement of the charge population produced, including density and individual dust detections. RF sensors detect emission from the impact and expanding plasma. Optical sensors measure the temperature of the impact flash. Finally, witness plates provide a characterization of the dust size distribution. Figure 2.1 shows the layout of the chamber including all the sensor locations.

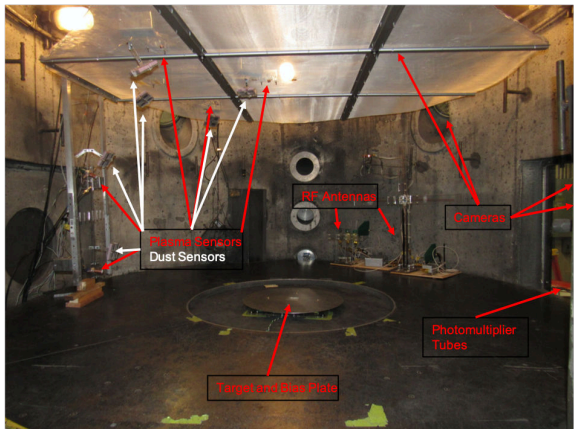

Figure 2.1: Overview of the test chamber layout at AVGR including the locations of all of the sensors. In the middle of the chamber floor is the target. The shelf that the upper sensors were mounted on is visible at the top of the figure. The plasma sensors are located at 4 elevation angles. The 4 cameras are separated into two different views.

2.2.1 Optical sensors

A set of high-speed cameras was used, including two Shimadzu cameras that took CCD images at 1 million frames per second with an exposure time of 0.5 μs and two Phantom cameras that recorded

at 51k frames per second in color with an exposure time of 19 μs. Both camera types were used to view the impact event at angles roughly perpendicular and parallel to the impact plane.

The optical diagnostic suite also included a fast-response photodiode mounted to a transimpedance amplifier and three Hamamatsu HC124-series photo-multiplier tubes (PMTs) with mounted RGB (600nm, 550nm, 450nm) monochromatic filter lenses.

2.2.2 Plasma sensors

Direct measurements of the plasma inherently modify the plasma itself. This complicates measuring the plasma at the point in time and space that RF is generated. Therefore, we performed far-field and remote measurements with the goal of inferring the earlier properties of the plasma. To do this, a set of Faraday cup plasma sensors and accompanying single-stage transimpedance amplifier circuits were designed and manufactured for these experiments.

Multiple plasma sensors were implemented to measure the spatial density and charge distribution of the plasma plume, as well as the time of flight of the plasma at different elevations. The sensors were positioned in the AVGR chamber at 4 different elevation angles: 10°, 30°, 60°, and 90° measured from the floor of the chamber. This corresponded to distances from the target of 0.914, 1.067, 1.168, and 0.94 meters respectively. Two sensors were used at the 60° angle, separated by 45°, to characterize the azimuthal variation in the plume.

2.2.3 RF sensors

Several RF sensors used in previous impact campaigns were reused for the 2019 AVGR experiment. In particular, patch antennas tuned to 169 MHz, 315 MHz, and 916 MHz were used alongside new sensors. Patch antennas, also known as planar antennas, provide narrowband measurements of the power spectral density around their central frequencies.

New for the 2019 experimental campaign at AVGR, several sensors were developed to probe different aspects of the EMP: a log-periodic monopole antenna (LPMA) to capture a wide band of the signal power spectral density, a polarization sensor (PolH/PolV) to determine the electric field direction, and a prototype energy harvesting sensor (EHar) designed to rectify the EMP into a DC signal.

The LPMA bandwidth ranged from 0.9–1.8 GHz, covering a range of frequencies unexplored by the patch antennas. The sensor was printed onto a PCB using microstrip antenna guidelines published in [94]. A printed monopole antenna designed for the GHz range provided a small factor, relatively simple design, and cheap manufacture. Log-periodic antennas are nominally frequency-independent, in the sense that they appear identical in impedance to a broad range of frequencies due to their geometry [10]. This feature grants them a flat frequency response in their design bandwidth, making spectrogram interpretation simple and providing a good sample of the power spectral density over that range. A monopole design prevailed over a similar dipole design since the asymmetry between the antenna elements and the ground plane simplify the interface with a transmission coaxial cable. Namely, this means that, unlike a dipole antenna, the inclusion of a balun — a balanced-to-unbalanced signal converter — was unnecessary. Both the LMPA and the patch antennas were mounted on an acrylic structure. The structure separated them from the chamber floor and protected the circuit boards from impingement by the incident plasma. The structure was manufactured using laser-cut, thin acrylic sheets, secured together suing nylon fasteners. The use of plastics in the structure ensured minimal interference with the electromagnetic signals.

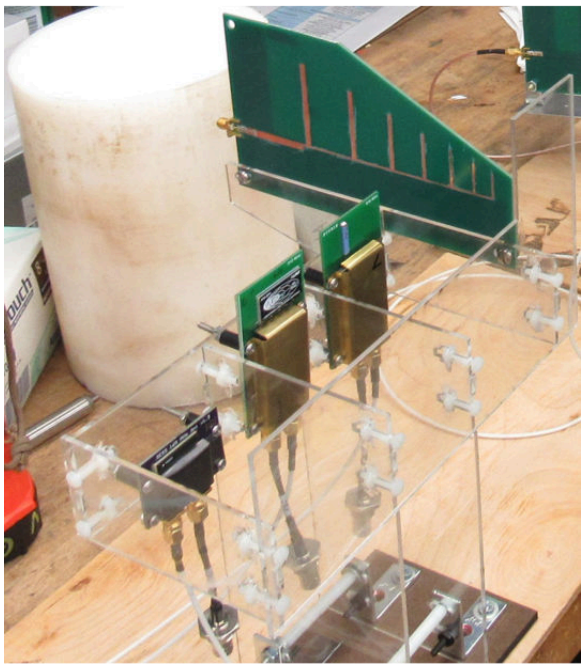

Figure 2.2: View of the LPMA and Patch Antennas mounted in their acrylic stand. From the bottom left to top right: 169 MHz patch, 315 MHz patch, 916 MHz patch, and LPMA.

EHar is an identical LPMA mounted to a rectifier circuit to turn the rapidly varying EMP signal to a DC output, forming a broadband rectenna. Rectenna technology and RF energy harvesting on Earth has significant heritage and numerous applications. Harvesting energy from HVI-EMPs is a challenging problem. Terrestrial signals tend to be continuous rather than impulsive, so most energy harvesting research focuses on either tapping into extant continuous signals such as WiFi, Bluetooth, or radio communications, or from purpose-built RF sources [82]. Further, the raw EMP signals are anticipated to be on the order of or small relative to the typical diode threshold voltage, so boosting the voltage level must be boosted through a charge pump or similar mechanism.

Harvesting from transient sources remains a challenge. For efficient operation, the coupling capacitors used in the rectifier need time to charge. Recent work into minimizing the start-up transients of continuous RF harvesters [63, 62] inspires a solution to the problem, but the short timescale of the EMP means that, as is, these solutions are ineffective. Several rectification topologies were considered, most variants on the Dickson charge pump [22] or the Cockroft-Walton [13]. The rectifier chosen was an enhanced Dickson rectifier [2] designed to operate in the middle of the LPMA bandwidth.

PolH and PolV, shown in fig. 2.3 are two 250 MHz, orthogonally oriented dipole antennas, designed to measure the horizontal and vertical electric field component respectively. The antenna elements were made of copper rods, connected to bazooka baluns [9], and terminated in SMA connectors. Coaxial cables conduct the signal from the antenna assembly, through a 20 dB LNA, to the chamber pass-through, and to the exterior oscilloscopes. The choice of the central frequency was motivated by a few factors. Results from previous experimental campaigns and theoretical work suggest an inverse square frequency dependence of the EMP signal power spectral density [12]. Lower frequency antennas therefore detect stronger signals than higher frequency ones and have

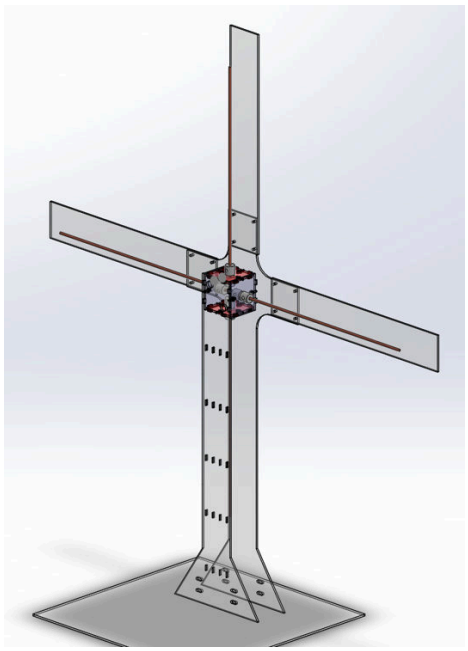

(a) CAD visualization of the PolH and PolV antennas from behind.

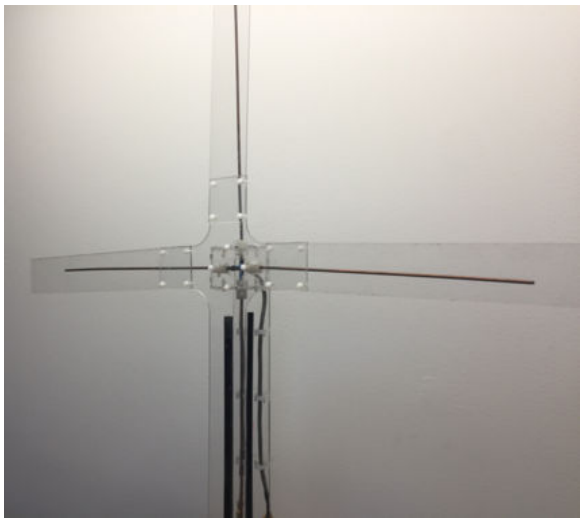

(b) Photograph of completed antenna from the front.

Figure 2.3: Polarization antenna, showing the antenna elements and acrylic mounting structure.

better signal-to-noise ratio (SNR). Larger antennas would not fit in the test chamber and would also see enhanced near-field effects. The bazooka balun was constructed from EMI copper shielding, sleeved over the exterior of the coaxial cable. The sleeve end closest to the antenna elements terminates in air, while the opposite end is soldered to the coax shielding conductor just before the SMA connector. An acrylic mounting structure was laser cut and used to mount the elements horizontally and vertically.

2.2.4 Dust witness plates

The witness plate design is based on Nakamura et al. [70], where ejecta were characterized by counting holes due to secondary impacts on thin membranes of various thicknesses and materials. We chose PET film (Mylar) for the witness plates for two reasons. First, it is inexpensive and readily available in many micron-scale thicknesses. Second, the low yield strength compared with metal foils makes plastic film ideal for characterizing microscopic ejecta because the minimum ejecta size for penetration is reduced and, for ultra-thin films, the hole size closely approximates the impacting particle [70, 36].

Each witness plate consists of a sheet of film sandwiched between a laser-cut acrylic aperture, approximately 2.5 cm square, and a layer of polyethylene mesh to provide structural integrity. An assembly unit, shown in Figure 2.4, consists of four witness plates of different thickness PET film from 1 to 15 µm, a foam backing to prevent ricochet impacts, and a mounting structure designed for easy swapping of witness plates between shots. We used multiple thicknesses of film with the goal of estimating ejecta velocity based on differential penetration of different thickness films. Due to the distance of the witness plates from the impact site, however, there were insufficient secondary

impacts to enable velocity estimates. We present ejecta size and shape measurements from the 1 µm thick films to minimize the error incurred by assuming the hole profile approximately matches the ejecta profile.

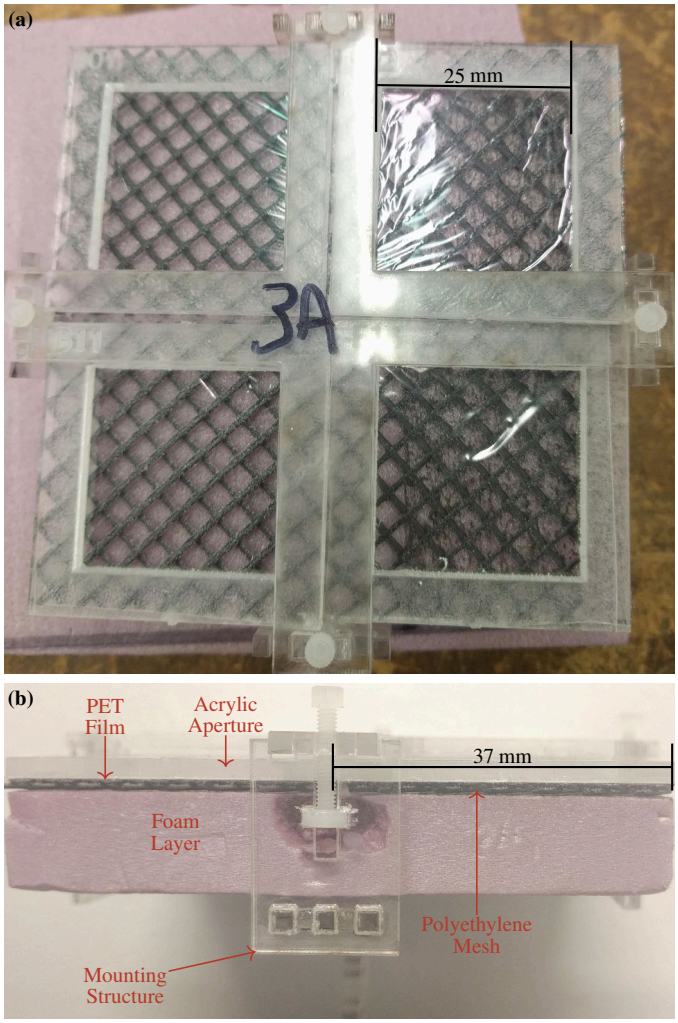

Figure 2.4: **(a)** Top view of the witness plate assembly. Each aperture contains a different thickness of PET film. **(b)** Side view of the witness plate annotated with the assembly components.

3 Measurements and analysis

In this chapter we present a summary of the measurements made using the sensors described in the previous section, as well as post-impact photography of the impact targets.

3.1 Cratering

The differences in cratering for impacts in different materials can explain some of the observed differences in the plumes. Cratering in the target is a dynamic event that influences the angles at which the plume propagates. As the projectile size and velocities were held approximately constant the differences in cratering between the materials is also indicative of their relative properties. For example, softer materials will generally have deeper craters.

Images of the various craters can be seen in Figure 3.1. Aluminum had the deepest cratering out of all of the metals; followed by copper and then tungsten. The crater radius found from equation 4.22 exactly matched with the measured values of 0.25 cm for aluminum. FR4 had the deepest crater of all of the materials. Additionally, FR4 had a cavity that formed below the surface and delamination of the first few layers of material. The regolith analog had a wide but shallow crater, which could have been the result of settling of the material due to its looseness. Finally, glass had a shallow crater similar in depth to tungsten. Cracking and spalling of the target is observed in tungsten and glass well outside of the crater radius which is expected to have produced significant macro-ejecta.

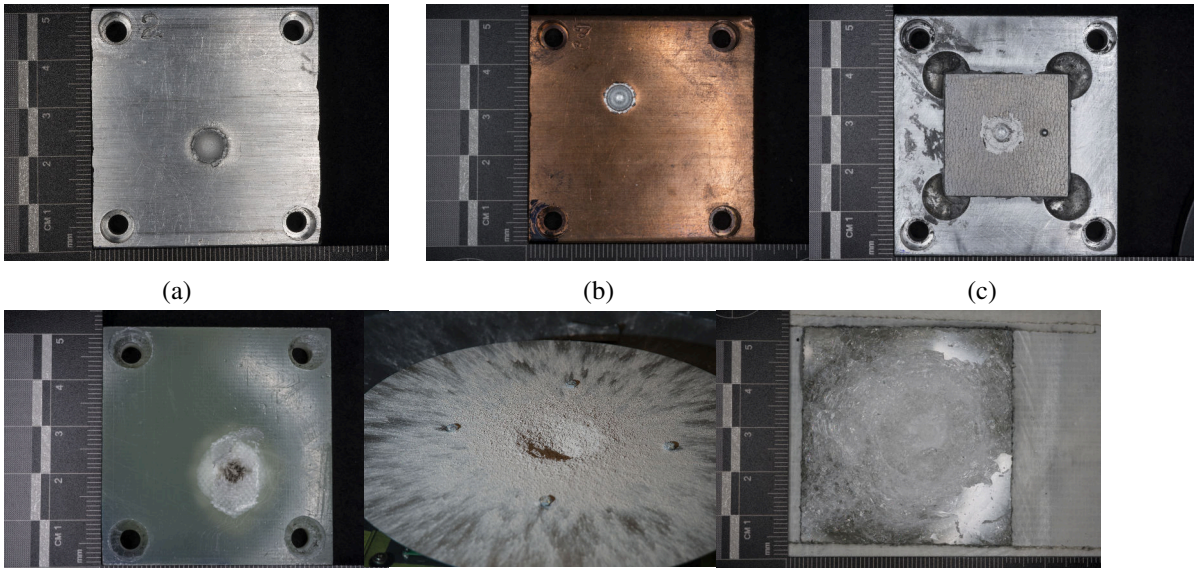

(a) (b) (c)

(d) (e) (f)

Figure 3.1: Cratering in all tested materials.

3.2 Plasma plume expansion

Measuring the plasma plume evolution is done with the goal of understanding the plume properties and eventually ascertaining the source of RF emission. RF was observed during the -300 V biased aluminum shots [100]. Plasma plume evolution is determined from plasma sensor data, which gives far-field measurements and camera data, which is used to infer the distribution of the plume during the first few μs.

Data were successfully recorded by the plasma sensors and cameras for all shots during this experimental campaign. Due to higher noise of the sensors in the AVGR test chamber compared to the lab environment in which they were developed, all plasma measurements were low-pass filtered. A 4^{th} order Chebyshev Type 2 filter with a 2.0 MHz cutoff frequency and a 60 dB attenuation was implemented in Matlab. The Chebyshev filter was chosen due to its steep roll-off with respect to alternatives. An example of the filter is given in Figure 3.2.

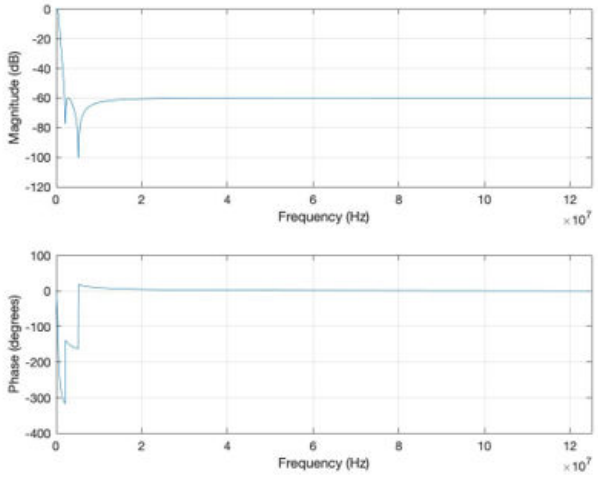

Figure 3.2: Bode plot of the low pass circuit applied to the plasma sensor measurements.

Resulting filtered plasma sensor traces are converted back to current from the voltage signals produced by the transimpedance amplifiers, then divided by the sensor collecting area to produce plots in A/m^2 with respect to time. This choice of units normalizes the data between the two different sensor sizes. Positive currents are positive particle detections, while negative currents are negative particle detections. Finally, it should be noted again that the inner cup of the sensors was unbiased. Therefore, both positive and negative particles impinge on the sensor with equal opportunity or even concurrently. This feature is demonstrated in Figure 3.3, which shows a sensor trace from a shot on unbiased aluminum that has both electron and positive ion detections.

3.2.1 Impacts on Regolith Simulant

Comparing our results from the regolith shot and the dolomite results of Crawford and Shultz [16] serves as a source of validation for the plasma sensor measurements. The elevations where charge is observed and the sign of the charge match their observations. To illustrate this the 90° sensor trace is given in Figure 3.5a which shows mostly postive charge detection and the 10° sensor trace

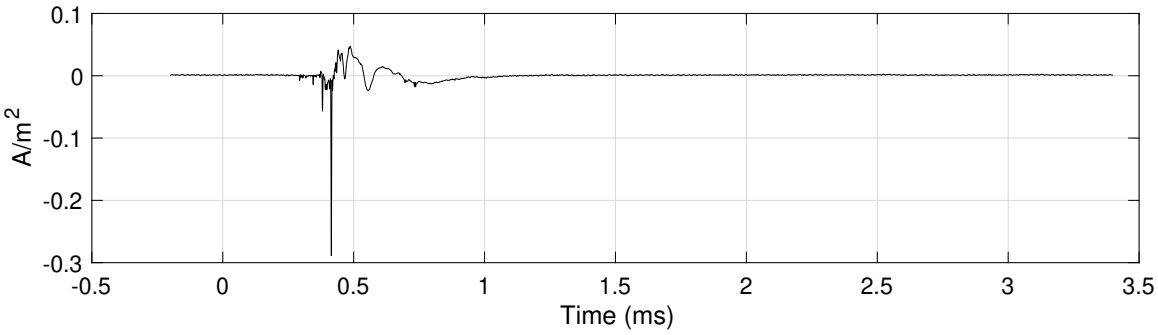

Figure 3.3: 60° sensor trace from an unbiased shot on aluminum (shot 2) that shows detection of both ions and electrons as well as charged dust. Ions are the positive currents while the electrons are negative. Dust detections are the sharp peaks before 0.5 ms and are mostly negative. The impact occurred at 0 ms and the signal lasts until roughly 1 ms.

is given in Figure 3.4 a slight negative detection followed by positive. These signs of charge are as expected and give confidence that species charge can be concluded from the plasma sensor data.

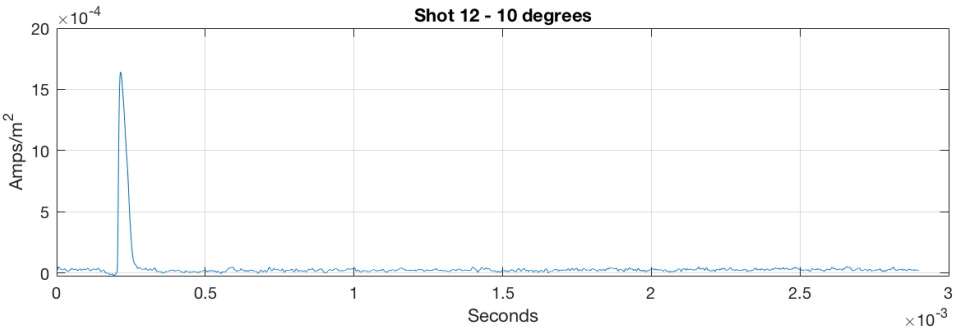

Figure 3.4: 10° sensor trace from the shot on the regolith simulant. A small negative detection then a positive detection is observed.

The regolith simulant shot also gives the clearest evidence of charged dust detection. The 90° sensor trace for this shot can be seen in Figure 3.5a. In this signal multiple narrow, sub μs, signal peaks can be observed. These peaks have rise times equivalent to those measured for the circuit and last 0.1 μs, meaning these peaks are a detection of an impulse of charged particles. Additionally, the spectrogram of this signal is given in Figure 3.5b and the scalogram from a wavelet analysis in Figure 3.5c. Both show narrow detections in the MHz range that are separate from the main kHz signal, suggesting further that these signals are impulses of charge on top of the detected plasma. This impulse of charge is what was expected to be seen from a charged dust grain detection. A piece of dust saturated by electrons or ions would, in theory, instantly - subject to the rise time of the system - deposit that charge upon impact with the sensor surface, creating a pulse of charge detection. Although plasma was detected on the 10° sensor, dust was only seen on the 90° sensor as can be observed.

The peaks with larger widths in Figure 3.5a are theorized to be different ion species. In this case the ions are positive, but negative ions have been detected in previous experiments [57]. A time of flight difference for different species of a plasma could result from differential drag with the

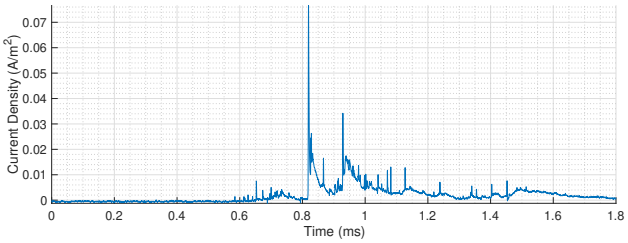

(a)

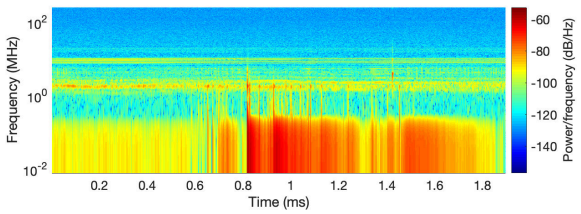

(b)

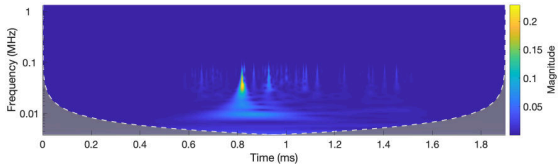

(c)

Figure 3.5: (a) trace from the 90° plasma sensor from the regolith simulant shot that shows charged dust. The sharp peaks indicate charged dust. In this shot ion detections dominate. Time is from the moment of impact. (b) spectrogram of the same sensor trace where frequency peaks from charged dust are visible. These peaks from the dust are separate from the main plasma. (c) scalogram from a wavelet analysis of the regolith simulant shot. This analysis confirms that the dust cause impulsive signals separate from the main plasma signal.

background gas, internal electric fields separating out species by mass, or by differences in thermal velocities even if all of the ions are at the same temperature. For this later case, species time of flight to the sensor can be approximated using the thermal velocity given in Equation 3.1, where K_B is the Boltzmann constant, m_i is the ion mass, and T_i is the ion temperature taken to be 0.2 eV, which was found to be the best fit to the data.

$$v_{th} = \sqrt{\frac{K_B T_i}{m_i}} \tag{3.1}$$

This calculation, assuming an isothermal expansion, for some of the most common elements in the dolomite/azomite impact (oxygen, silicon, magnesium, lithium, carbon, potassium, and aluminum) results in times of flight that approximately match the peaks that the sensor recorded. It is unlikely that all ion species will have identical temperatures, as each element has a different ionization energy and collision rate. However, this result suggests the possibility of using hypervelocity impacts to study the composition of regolith bodies, and possibly even the impactors, without the use of external fields.

3.2.2 Impacts on Aluminum

Aluminum shots also exhibit the signature of charged dust. In contrast to the regolith shot, which detected dust on the 90° sensor, the detection of charged dust in aluminum occurred in the 60° elevation sensors, which matches dust ejection angles previously observed for aluminum [73, 1]. This can be seen in the sensor trace of Figure 3.3 which exhibits similar impulsive detections, through sharp peaks, as the regolith simulant. As further evidence that these detections are indeed dust, the dust curtain that was the source of these detections is clearly visible in the camera data. An example of this is shown in Figure 3.6. In this figure the visible cone-like structure at the center of the plume has an angle of 60° with respect to the horizontal, the same angle as the dust detections. Also of note is that the sensors that detected dust always detected electrons and recorded a near identical velocity of 4 km/s, based on detection time after impact, for plasma to initially impinge on the sensor. The detections of electrons and particle velocity were consistent no matter the bias that was applied to the target. However, we expected that biasing would change the time of flight and charge of the signal at all angles due to the electric field's influence on the plasma. This showcases the dominant role in the plume dynamics that dust played in the aluminum shots as dust appears to have more influence on the plume than the external fields do.

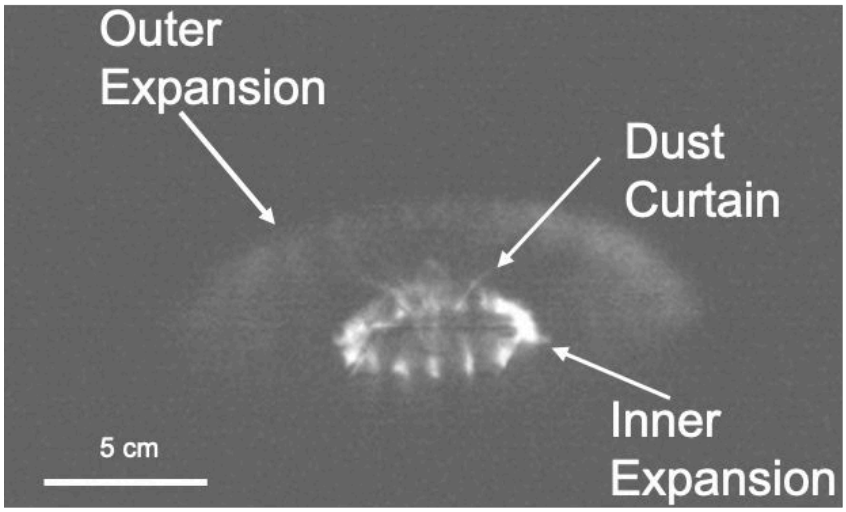

Figure 3.6: Single frame from the Shimadzu high-speed footage of an impact on an aluminum target. The dust curtain as well as both the inner and outer expansions of the plume are clearly visible. The inner plume is unstable, with a periodic structure. Dust in this high-speed video frame is at 60 ° from the horizontal.

Figure 3.6 also shows the general observed geometry of the metallic target impacts. The bulk of the plume is primarily horizontal with most of the vertical component resulting from the dust. Based on the high-speed footage it appears that the dust pushes up through a region of plasma, gaining charge as it collides with particles in the plasma, and ultimately pulling some of the plasma along its trajectory through fluid drag and electromagnetic forces. The possibility that macroscopic charge separation exists is strengthened as a result of this plasma and dust interaction. As the dust pulls mainly electrons along its trajectory for the aluminum shots, based on the plasma sensor data

and likely resulting from the higher collision frequency of electrons on the dust. This transport of negative charge leaves behind a positive charge in the main plume, creating a separation of charge. The amount of plasma brought up to the upper sensors is not negligible. For all shots, plasma is detected on the upper sensors for much longer than it is on the lower sensors, usually on the order of 1 ms for the upper sensors and 0.1 ms for the lower sensors. These timescales are seen in Figures 3.3 and 3.13, which are plasma results at the 60° and 10° sensors respectively. Additionally, the peak charge density recorded on the upper sensors is either equal to or greater than that on the lower. The current density is nominally 0.01 to 0.1 A/m^2 for the upper sensors and 1×10^{-4} to 0.01 on the lower.

As further evidence of the effect of the dust on the plasma plume, biasing was observed to influence both the time of flight and charge detection on the lower sensors. Figure 3.7 shows a comparison of the 10° sensor for an unbiased, -300 V, and 300 V biased shot. The electrostatic force from biasing the target separated and accelerated the plasma species. For unbiased shots the average velocity of the plasma based on time of arrival at the sensor is around 10-15 km/s, while for biased shots the velocities were 20-30 km/s. The plasma sensors at the 30° elevation showed similar responses to biasing. Clearly, biasing had an influence on the plume, but this influence was not seen where dust was detected, suggesting dust effects dominated.

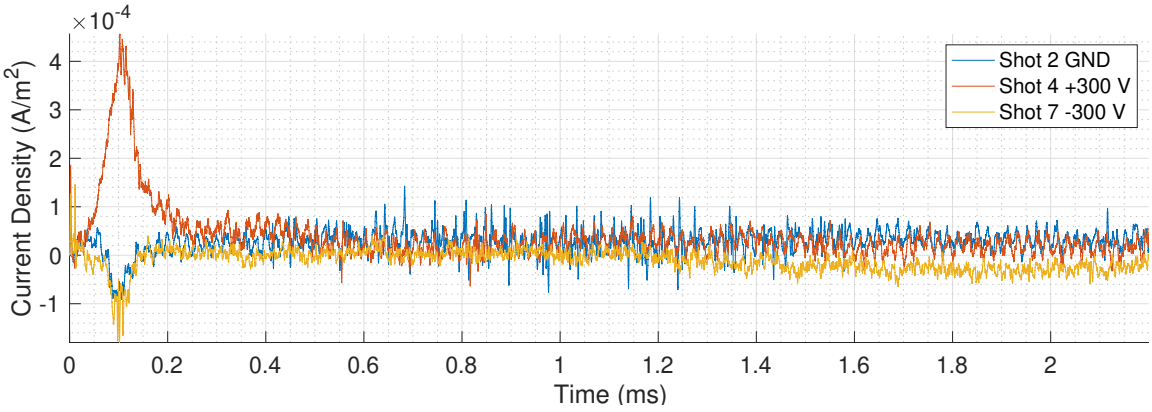

Figure 3.7: Comparison of the 10° sensor traces for an unbiased, +300V, and -300V bias on aluminum. Positive biasing causes ions to be detected, as expected. The start of the detection for the biased shots is slightly sooner than for the grounded shot, by a few μs.

A comparison of 60°, 30°, and 10° sensor traces for all of the metallic shots is provided in Figure 3.8 through 3.10. No discernible pattern for how the 60° detections change with biasing can be observed for the aluminum shots. The difference in detections seems more to be the results of shot to shot variability in impact location and speed. Lower sensor signals are clearly affected by biasing, as described above.

Further evidence of the distribution changing due to biasing is provided by the high-speed video footage. As biasing increases in either polarity, the number of frames with visual plasma increases. For the 300 volt biased cases this increase is 10 microseconds over the grounded shots. This is due to an increase in collisions between the ions and electrons due to the trajectories of charged particles being altered by the induced electric field. It is also observed that the plume in the negative bias cases has a slightly more vertical component than the other cases, coinciding with the increased electron signal seen on the upper sensors.

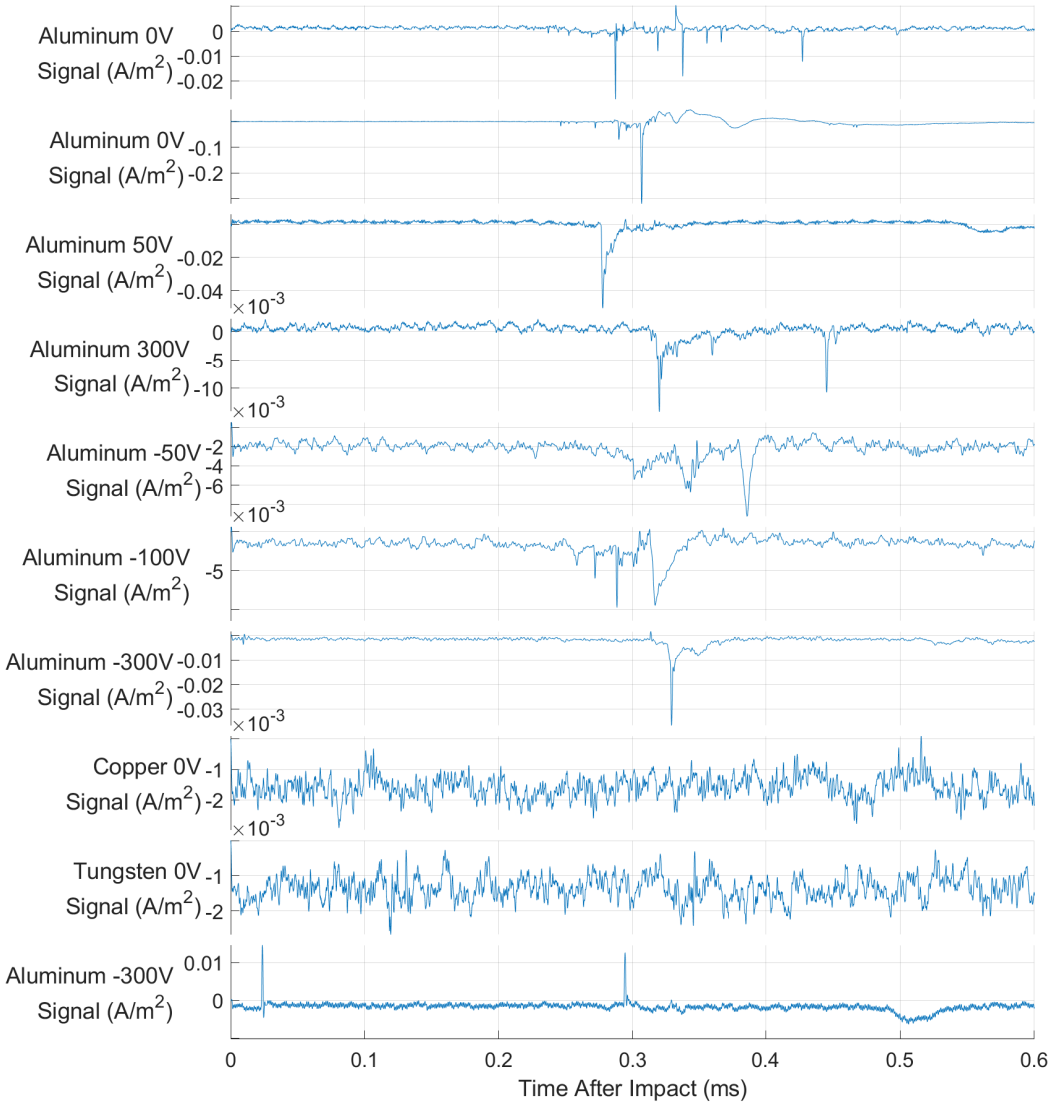

Figure 3.8: All sensor traces from one of the 60° sensors for all metal shots. Dust is clearly visible. The signal arrival time is very consistent for all aluminum shots regardless of bias. The differences in signal likely result from differences in impact location leading to different parts of the plume being captured.

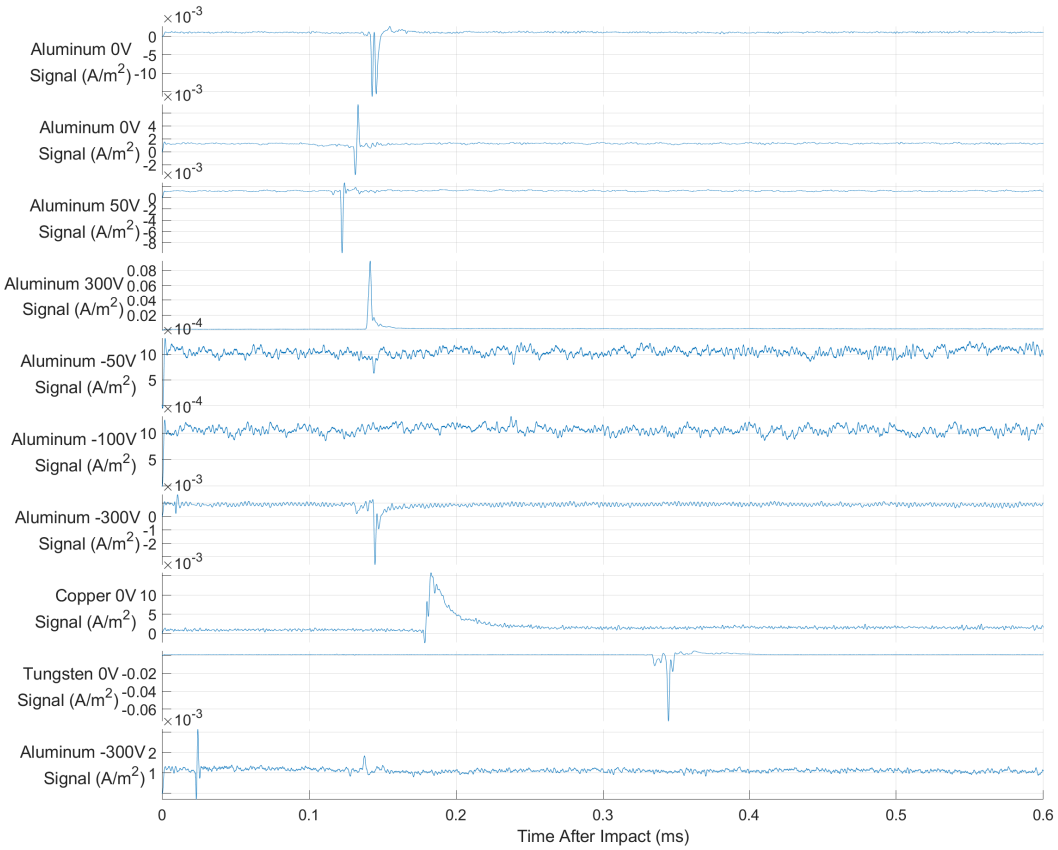

Figure 3.9: All sensor traces from the 30° sensor for all metal shots.

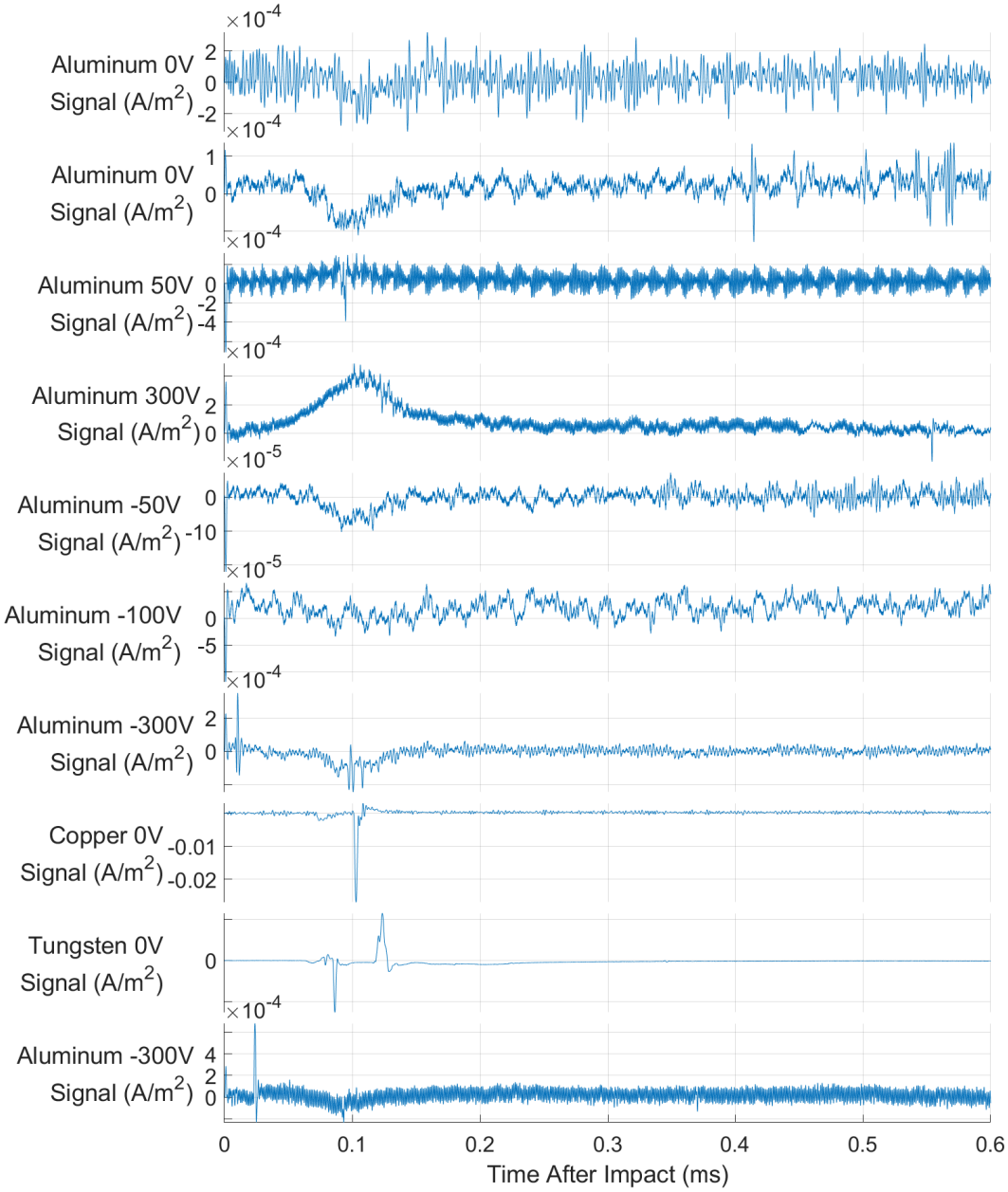

Figure 3.10: All sensor traces from the 10° sensor for all metal shots. Late time signals can be observed in the -300 V aluminum and tungsten shots.

The previously mentioned notion of a quasi-neutral plasma inducing a quasi-zero current is seen in Figure 3.8. No extended ion or electron signal is recorded in the current trace, but both species are clearly detected. In addition, the signal on the spectrogram in Figure 3.11 lasts 0.5 ms longer than that on the faraday cup trace. This is due to the cup's detection of a quasi-neutral plasma. Given that the ion and electron signals balance out for essentially all detection time, it is concluded that the species arrived at the same time. Detection of quasi-neutrality for the non-biased shots shows further evidence of particle separation due to biasing. No signal like this was detected from the biased traces or their spectrograms. The only other traces where this was observed is the 10 degree sensor traces on the copper and tungsten shots.

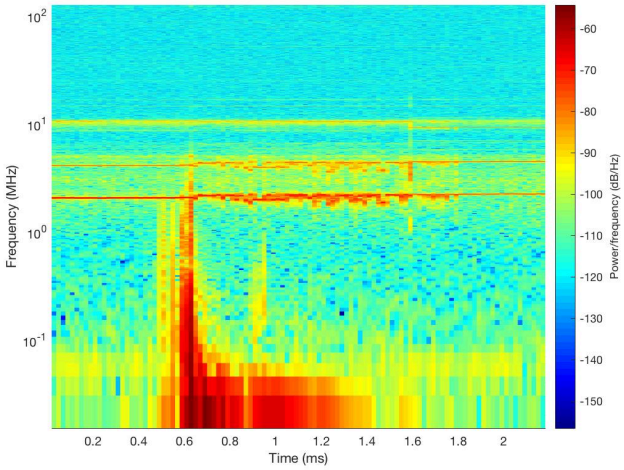

Figure 3.11: Frequency content of recorded signal at 60° of shot 2

These observations of dust and charge distribution have significant implications for spacecraft. First of all, the macroscopic charge separation induced by the dust is a possible source of RF emission. Secondly, the dust carries large amounts of plasma at elevations where the vaporized plume would not normally travel. Meaning, in the case of an impact that produces dust, electronics that are not immediately in the vicinity of the impact point could still suffer electrical effects from plasma impingement and discharges if they are in the path of the dust. Additionally, as this dust is traveling at least 4 km/s, secondary hypervelocity impacts are possible. These new impacts will occur in the plasma that the dust dragged along with it, creating regions of high charge density. Impacts on negatively biased targets have been shown to have increased frequency of RF emission [56]; the electrons that the dust caries may have the same effect. That being said, if there is nothing above the point of impact, then the dust may actually make electrical effects less likely by carrying a significant portion of the plasma off into space.

There is further evidence of dust from the high speed imaging during the aluminum impacts in addition to the dust being visible in the plume. What appears to be secondary ionizing impacts on the upper shelf can be viewed at later times. Flashes of light such as these appear in all of the aluminum tests and appear in the same general elevation as the plasma sensor and the expected angle of the dust. Some flashes are far away from the plasma sensors, meaning that this phenomena is not a result of something with the sensor. The fact that light is emitted seems to indicate that these are ionizing events. Pet-g, the material of the upper shelf, has a speed of sound of roughly 2300 m/s.

Therefore, these impacts would be around that velocity or faster. Further evidence of these flashes being impacts can be found by looking at the shelf itself. Upon close inspection various pock marks can be observed with scorching around them.

The potential for secondary ionizing impacts is important for spacecraft safety. Some forms of glass have speeds of sound not much faster than the pet-g, meaning these impacts could easily ionize glass, especially if the initial impact velocity is faster. Additionally, the velocity of the dust ejected should be faster in space, as there is less of a background to slow the dust down and the plume density is expected to be lower.

The target voltage reading for the aluminum impacts did not behave as it was expected to. As plasma was accelerated away the target voltage should have tended towards 0 as the potential from the plasma varied. This has been observed in measurements on spacecraft such as Cassini and in related ground based experiments. What was actually observed, in all cases apart from one, was that the target voltage increased or moved away from zero volts. To illustrate this three measurements for three different negatively biased shots are given in Figure 3.12.

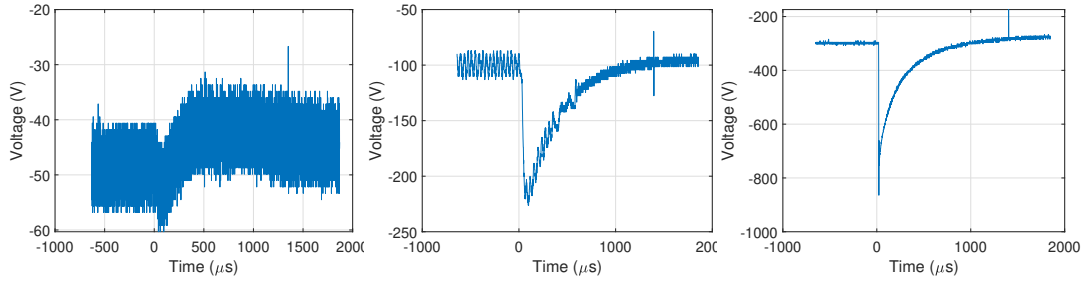

Figure 3.12: Measured target voltage change as a function of target bias for 3 of the negatively biased targets.

As can be seen, the amount of change does appear to increase with increasing target bias meaning the effect is coupled to the biasing. Likely, due to the late time of the signal, this is the result of a sheath escaping off the edge of the target. In the case of a negatively biased target the sheath would be made of ions. Therefore, if this sheath rapidly leaves the target the target will see a decrease in positive charge and therefore become more negative, as observed.

3.2.3 Impacts on Copper and Tungsten

Ejecta was visible in the high-speed camera data for the tungsten shot, but none was measured on any of the plasma sensors. It should be noted that the tungsten target was sintered, which could result in more granular ejecta from spalling of the sintered surface. Tungsten was already expected to have more solid ejecta as it is a brittle metal and is therefore more susceptible to tensile fracture. Significant spalling of this target from outside of the main crater area and conforming to the sintering grains was observed that was not present in the other metallic targets. That said, not all of the dust came from spalling. As can be seen in Figure 3.6, dust can clearly be seen to come from the crater itself.

The evolution of the tungsten plume is shown in Figure 3.17. Although dust can be clearly seen in the last frame, that frame is 30 μs after impact, meaning the dust was traveling slowly compared

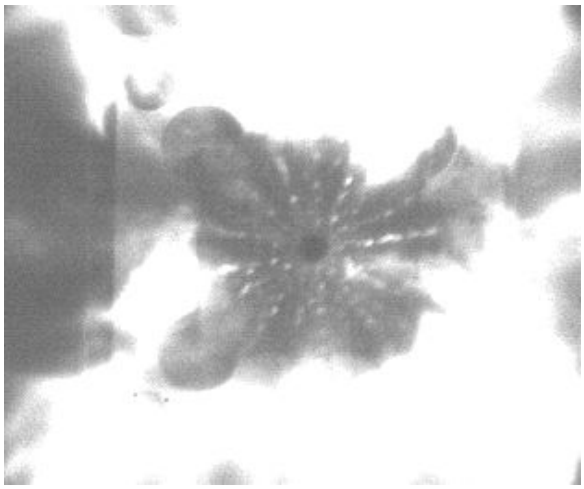

Figure 3.13: Ejected dust from the tungsten crater visible in the high speed imaging. Discrete dust jets are visible.

to the dust from aluminum. This frame also shows plasma is concentrated at this later time around the dust. Based on the larger apparent grain size, low density, and slow speed of this dust, it is likely from spalling of the target, instead of incomplete vaporization of the target. The plume itself is very horizontal as the dust did not induce much vertical displacement of plasma.

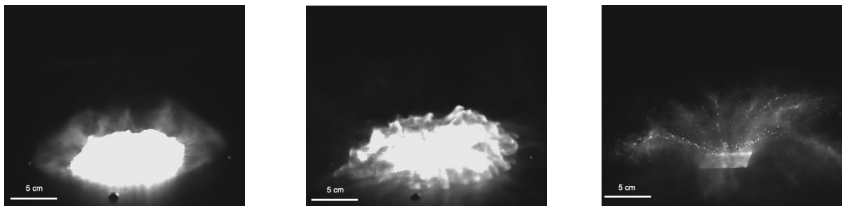

(a) (b) (c)

Figure 3.14: Shimadzu high-speed video frames from an impact on tungsten, 10, 20, and 30 μs after impact. The inner and outer expansion geometry is observed just as it was in aluminum. This plume appears to be turbulent. At the later time plasma can be seen to be concentrated around the visible macro-ejecta.

In contrast, dust was not observed on either the plasma sensors or the high-speed images for the copper shot. That is, no spectrogram or wavelet transform from the copper detections showed the expected features for dust detection. Copper likely did produce dust, it just did not hit any of the sensors or interact with the plume in a visible way. For comparison to aluminum, a frame from the camera footage of the copper shot is given in Figure 3.15.

Plasma measurements for the 10° sensor for both copper and tungsten are in Figure 3.16 which shows that 100 times as much plasma was measured for this angle than for aluminum. Interestingly, both electrons and positive ions were detected at this elevation for these shots. Electrons arrive first, as expected due to their mobility, followed later by positive ions. This charge separation is typical for plasma expansion into a vacuum [68], but is complicated by the background gas. Both shots recorded positive ion detections at multiple times which, like the regolith analog shot, could

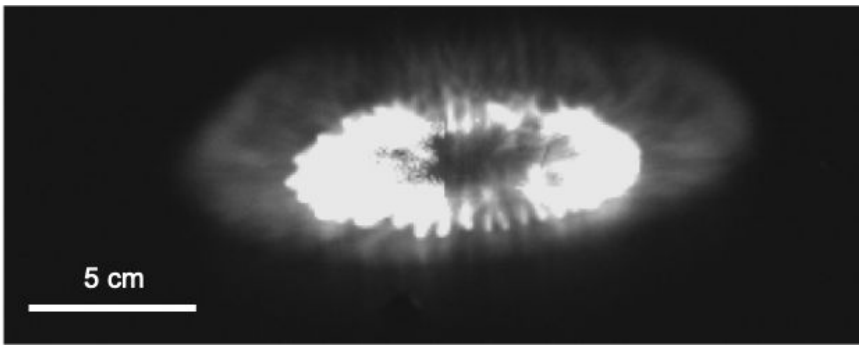

Figure 3.15: Frame from the Shimadzu high-speed footage of the copper target shot. This plume is also unstable and showcases the two separate plume fronts. Copper resulted in the most horizontal plume, as can be seen in this figure.

be indicative of species separation which could be used for identification.

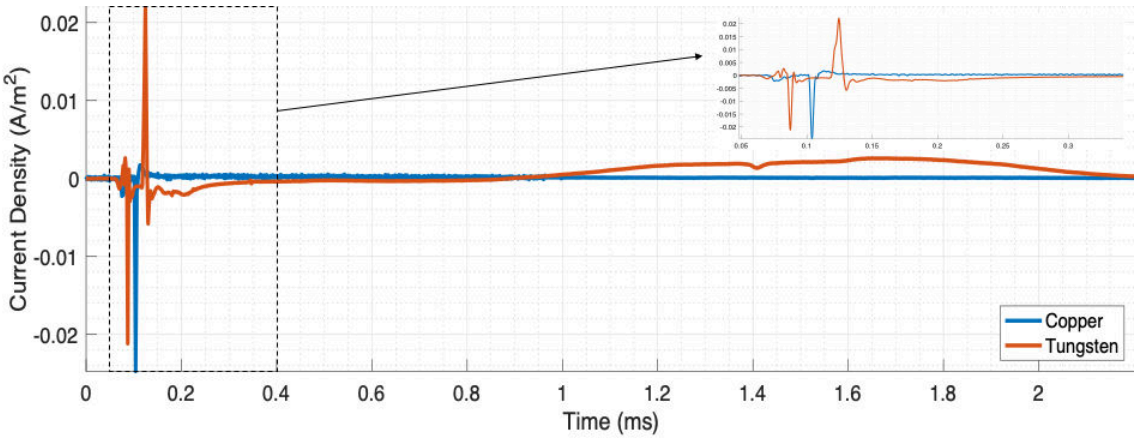

Figure 3.16: Comparison of the 10° sensor traces for copper and tungsten. Both show electron and positive ion detections.

The dense horizontal plume observed in these shots poses a significant threat to spacecraft electronics in the region of the impact. In contrast to the aluminum shots, there is no mechanism moving the plasma away from the surface of the spacecraft. This means that there is an increased chance of plasma impingement on some part of the spacecraft. Additionally, the impact plasma will interact with the plasma that forms a sheath around spacecraft due to the background space plasma and spacecraft charging. Interaction between these plasmas has the potential to cause instabilities, such as streaming instabilities, which can be a source of electromagnetic radiation. This is in addition to the charge separation observed during these shots, which again can be a source of RF emission.

3.2.4 Impacts on FR4 and Glass

The FR4 and glass targets were chosen to directly emulate spacecraft components: circuit boards and solar panel coverings respectively. This allows for direct assessment of the danger this class of

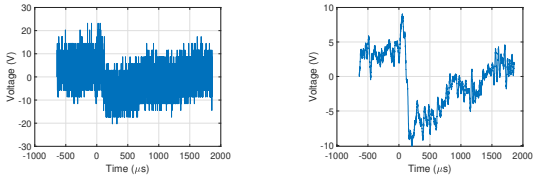

(a) (b)

Figure 3.17: Shimadzu high-speed video frames from an impact on tungsten, 10, 20, and 30 μs after impact. The inner and outer expansion geometry is observed just as it was in aluminum. This plume appears to be turbulent. At the later time plasma can be seen to be concentrated around the visible macro-ejecta.

impacts pose to spacecraft. Measurements of the FR4 plasma had some signals that may have been dust, but no clear detections like in the regolith simulant and aluminum. Glass did not show any signs of charged dust.

Both materials had very unique plume geometries in comparison to the metallic targets. FR4 had a plume that expanded almost completely vertically, with measurements only at the 60° and 90° elevations, as a result of the deep cratering and the porosity of the material. A region of dense plasma was at the center of the plume according to the high-speed footage as shown in Figure 3.18a. This was confirmed by the 90° sensor recording densities upwards of 0.1 A/m^2.

(a) (b)

Figure 3.18: (a) is the plume from the FR4 shot seen with one of the Shimadzu cameras. The plume was very vertical with a concentration of vertically moving plasma at the center of the plume. This image is roughly 10 μs after impact. (b) is the glass shot plume also seen from one of the Shimadzu cameras. It is the most hemispherical plume that was observed. This image is roughly 8 μs after impact.

The glass impact resulted in the most hemispherical plume out of all of the tested materials, as shown in Figure 3.18b. This was the only shot where plasma was detected on every sensor. Positive currents were recorded on the 60° and 90° sensors while negative currents were recorded on the lower elevation sensors. This suggests an elevation based separation of charge, similar to what was seen in the regolith analog. These detections were not long, lasting only a few μs, but the peak densities were 0.2 A/m^2 as seen in Figure 3.19.

No evidence of radial charge separation was seen in either shot, but the high density plasmas that result from these impacts pose a direct danger to the sensitive electronics on circuit boards and solar panels.

Observations and measurements of the plume from the different shots presented in this section have significant implications for using hypervelocity impacts as science tools as well as understand-

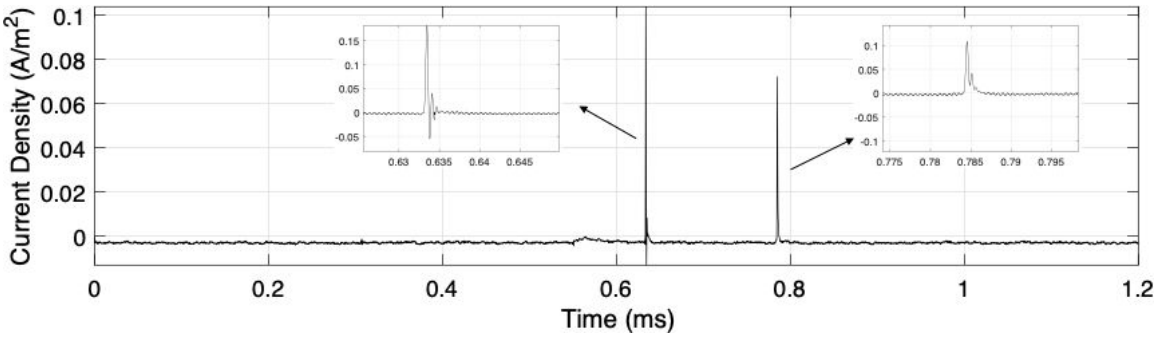

Figure 3.19: 60° sensor trace from a shot on glass. The detected peaks are very high but very short. They are longer than the detections of dust.

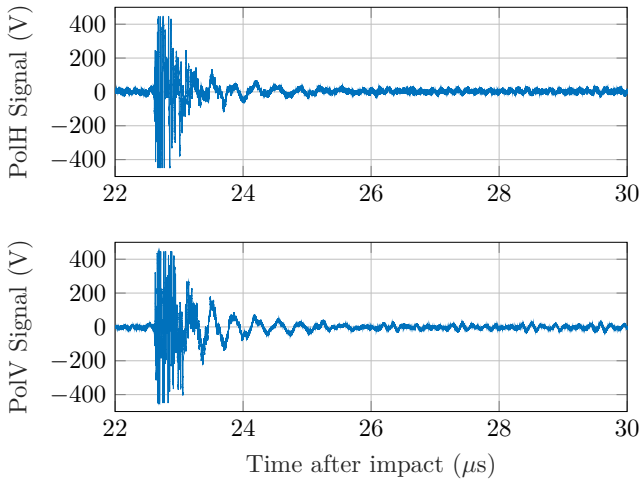

Figure 3.20: Raw traces of the Polarization sensor from shot 10 of the AVGR experimental campaign. Both signals are clipped at about ±450 mV.

ing the risks they pose to spacecraft.

3.3 Radio frequency emission

Data from the PolH and PolV antennas from shot 10 are shown in Figure 3.20. The EMP arrives at the antenna nearly 23 µs after impact. Although the oscilloscopes were adjusted from the previous shot with RF (Shot 7) the signals are still clipped. Data in the clipped regions can either be excised from the data set, providing no polarization information, or approximately reconstructed using techniques from seismology [101]. Also present in the data are sources of significant periodic noise. As seen in fig. 3.21, spectrograms of these raw traces show several indications of RF interference, notably at 5 GHz (WiFi), 880 MHz, 750 MHz, and 500 MHz. Since the noise is periodic, blind source separation techniques like prior constrained source separation (PCSS) [74] can remove these sources of noise.

After denoising with a PCSS algorithm, the polarization vector can be found by plotting the

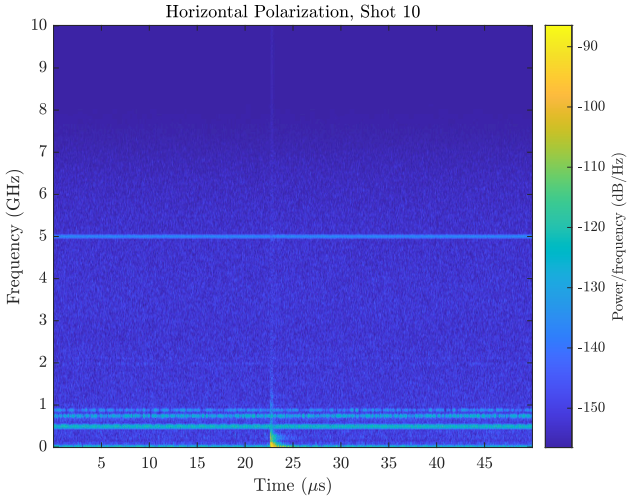

(a) Horizontal

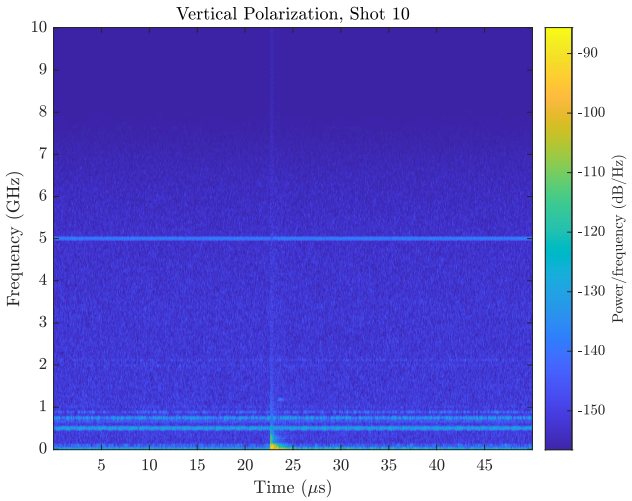

(b) Vertical

Figure 3.21: Spectrogram of the shot 10 polarization antenna data shortly after impact.

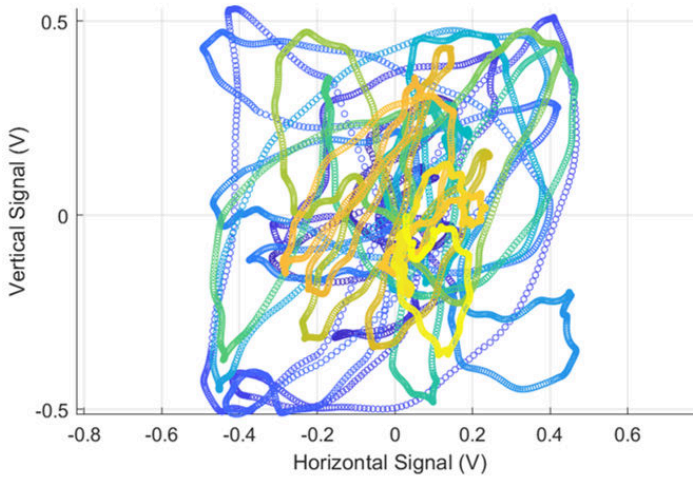

Figure 3.22: Electromagnetic pulse electric field polarization from Shot 10. Color indicates time, running from blue at the beginning of the EMP signal to yellow, about 20 µs later.

horizontal and vertical signals as a parametric curve as seen in fig. 3.22. Initially, the field appears to spiral inward, indicating circular polarization, however, the vector rotation changes direction several times, somewhat erratically. The results therefore suggest no significant directionality to the electric field. We considered the possibility of unwanted correlations between the two antennas given their proximity, however attempts to calibrate for this effect proved ineffective and further tests are needed to fully characterize this.

3.3.1 Target charging EMP

The theory for a target charging EMP from a hypervelocity impact came from the observation of the target charge. Presented again in Figure 3.23 are the target voltage measurements for shots 7 and 10, but now zoomed in. Now being zoomed in we can see that shot 10 does have movement towards 0, but it is after the move away from 0.

Curiously, the rapid movement of the target towards ground occurs at the same time that the RF sensors recorded an EMP event. This move towards ground is the direction that the target was expected to go due to the biasing of the target. In both shots the rise time of this signal is faster than the sampling frequency of the scope used. The entire voltage swing takes exactly 1 μs according to the oscilloscope, so the swing is likely faster. This timing of the target signal is the first part of what we expect to see during a target charging EMP, the other is consistent frequency content.

Shot 7 and 10 were very similar. Bias on the target was -300V in both cases and everything was configured the same. There is one slight difference in that the target in shot 10 was a few mm above the bias plate while the target in shot 7 was a few mm below. This can be seen in the high speed imagery. It is possible that this difference and the difference it causes in plume propagation is responsible for the timing differences between the two EMPs. Even though the timing is different the frequency content is roughly the same. Samples of the frequency content of the EMP for shots 7 and 10 are presented in Figure 3.24.

The frequency content recorded is constant between different antennas and similar between the two shots, at least in terms of the dominant frequencies. This suggests that the EMP came from a

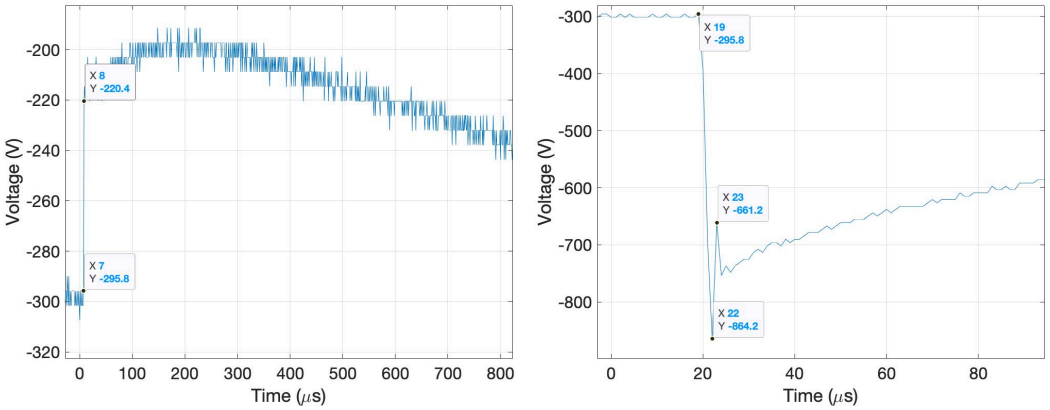

(a) (b)

Figure 3.23: (a) Zoomed in view of the target voltage measurement for shot 7 showing the time of the EMP (b) zoomed in view of the target voltage measurement for shot 10 showing the time of the EMP.

constant radiative source. Further evidence of this being a constant radiative source can be found for shot 10. For this shot a monopole antenna was placed outside of the chamber to try and measure some shot noise that was appearing at a constant time. This antenna had no amplifier and was not connected to the chamber in any way. It was merely an antenna, BNC cable, then oscilloscope. As can be seen in Figure 3.25, this antenna picked up the same frequencies as the other antennas, although it was sampled at a much lower frequency. This eliminates the signal being cross talk or effects of electronics.

For the experiments there are two things that could be radiating, the plate or the wiring of the plate. Frequencies of these two can be approximated by

$$f \approx \frac{c}{2\pi d_{plate}} \tag{3.2}$$

for the plate and

$$f \approx \frac{c}{(2)l} \tag{3.3}$$

where the (2) is used for a dipole and the (2) is ignored for monopole operation. Here l is the length of the wire that is radiating and d_{plate} is the diameter of the bias plate. Plugging in the geometry of the plate and wiring yields frequencies around 0.19 GHz for the plate and between 0.07 and 0.3 GHz for the wiring, depending on what wires are radiating and if the wire is assumed to behave as a dipole or monopole. This is close to the observed frequencies. The ambiguity over monopole vs dipole arises due to the geometry of the target wiring. All wiring is parallel to the chamber floor or goes through it, both of which complicate the apparent antenna geometry.

Further evidence of the EMP being a result of target charging can be obtained through the high-speed imagery of shot 10. There is a slight gap between the target and the bias plate that can be observed in the images that have been presented. At the same time of the EMP what appears to be a discharge event can be seen in this gap, as shown in Figure 3.26.

A discharge is not expected as the bias plate and the target should be at the same voltage. The most likely way this discharge could result is a large current pulse on the edge of the plate, leading

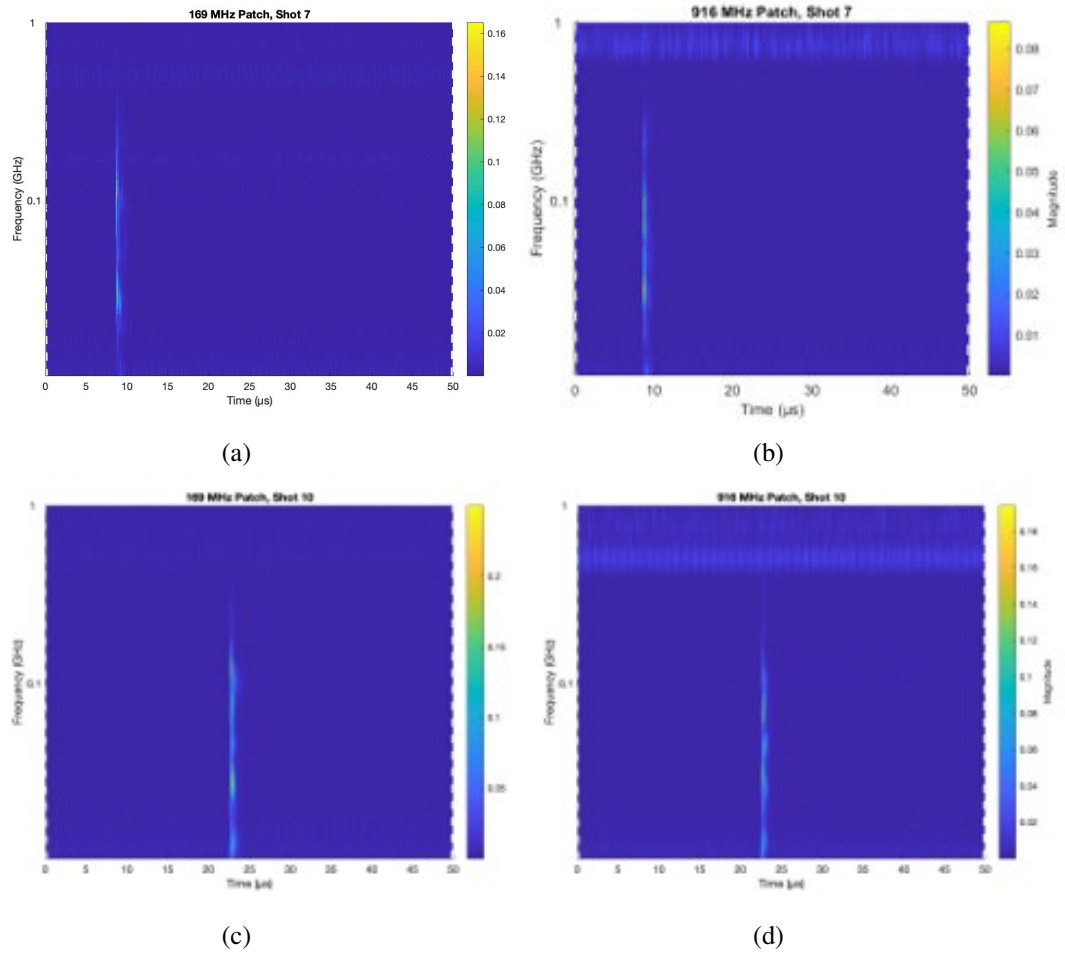

Figure 3.24: Spectrograms of two of the patch antennas for shot 7 and shot 10.

to charge imbalance on the plate as this current pulse is propagating. This would lead to the bias plate being at a different voltage than the target as the wiring that connects the bias plate to the target to implement the constant bias is longer than the radius of the plate. Based on an asymptotic velocity of roughly 10 km/s, an EMP timing of 22 μs means the outer expansion has just reached the edge of the bias plate. The target initially goes more negative as the positive charge in the sheath escapes off the edge of the plate then goes rapidly positive as positive charge is pulled back to the target and negative charge is electrostatically accelerated away.

An EMP from the outer expansion, which appears to be the case based on the timing in shot 10, means that the EMP resulted from the plasma formed during the jetting process. Therefore, the gas dynamics likely had a limited effect on the EMP as the majority of the gas dynamics involved the inner expansion. Without the gas dynamic influence the EMP may be stronger and more plasma would be allowed to freely expand instead of bunching in the contact surface.

Shot 7 and 10 were very similar. The bias on the target was -300V in both cases. Shot 10 had a 0.03 km/s faster impactor speed, a 0.03 Torr lower background pressure, and 0.1 mg less massive impactor in comparison to shot 7. Additionally, the target in shot 10 was approximately 1 mm above the bias plate while the target in shot 7 was approximately 1 mm below the bias plate. It is possible

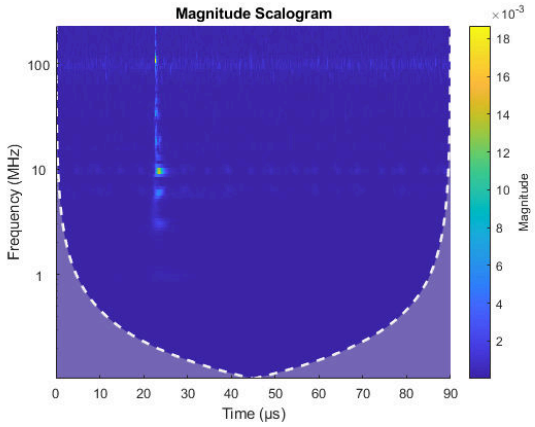

Figure 3.25: Signal from the monopole antenna during shot 10.

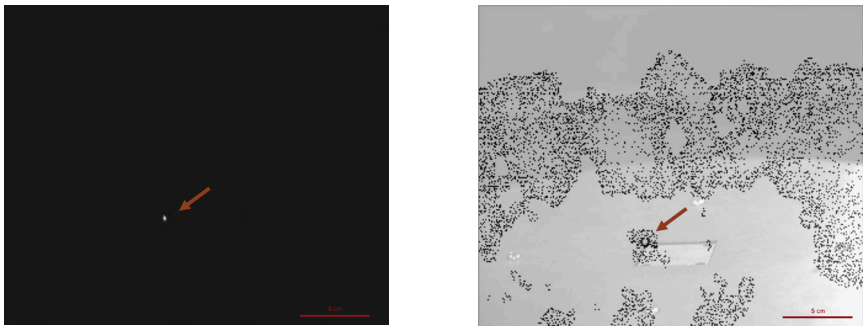

(a) (b)

Figure 3.26: (a) is an image of the second shot at a -300V target, roughly 20 μs after impact. This time after impact is when the target charging and EMP are observed for this shot. The bright dot pointed to by the red arrow is assumed to be an ESD event. (b) is also of the second shot at a -300V target, but with higher contrast, sharpness, and brightness. In this image it can be seen that the bright spot is at the upper left corner of the target interface with the bias plate. The plume is still on the bias plate.

that this height difference and the difference it causes in plume propagation is responsible for the timing differences between the two EMPs. In shot 7 the initial plume and runaway electrons can be observed to interact with the bias plate edge in the first few μs after impact. This interaction between the plume and bias plate was not observed in shot 10. For shot 7 the contact surface is just crossing the interface between the target and bias plate at the time of the EMP. It is possible that an ESD event is viewable in the high-speed imagery at this time, but it is not clear enough to make any conclusions. Likely, due to the interaction with the bias plate at the edge of the target the plasma density of the plume was slightly less, leading to a lower Debye length. This caused the charge acceleration event to happen sooner and with less plasma as evidenced by the smaller voltage change in the target in comparison to shot 10.

Other biased shots exhibited a target voltage response but no RF was observed. In these other shots, as viewed in Figure 3.12, the signal rise time is much slower and the amplitude is less. This strengthens the argument that the observed RF is a due to rapid target charging as it seems a fast

rise time and large amplitude is necessary.

Shot 8, the unbiased tungsten shot, also exhibited some RF behavior. It again corresponded to the target voltage response in time, but the frequency content was slightly different than previously observed, as seen in Figure 3.27. Only the high frequency part of the RF seen in shots 7 and 10 is present here and the signal lasts much longer. The timing of the RF for this shot exactly corresponds to the start and end of the target going negative. Again, this is pointing towards the RF being coupled to the target. For this shot it is likely that the potential on the target was rapidly varying. The timing of the RF corresponds to when the dust is visible in the high speed images. So the oscillation of the plasma around the dust could be altering the potential on the target, causing it to radiate. Further work is needed to fully understand what occurred during this shot, but initial data points to a dust created RF emission coupled with the target.

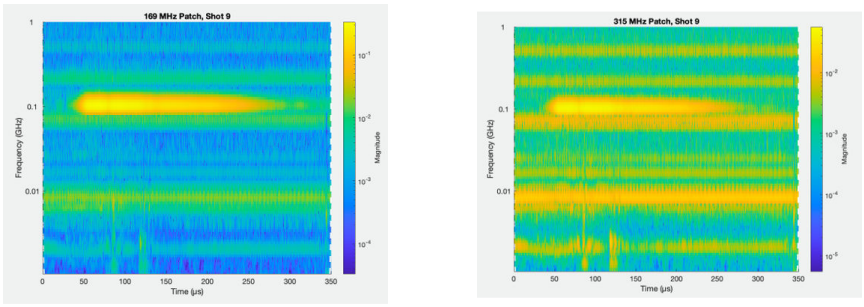

(a) (b)

Figure 3.27: RF emission seen on two different antennas during the shot on the tungsten target.

3.4 Dust population

We imaged the witness plates using a digital camera mounted in the trinocular port of a polarizing microscope equipped with a 20x objective lens with numerical aperture of 0.45. Based on the diffraction limit, this configuration can theoretically resolve features as small as approximately 0.7 µm, although differentiating holes from optical artifacts and obtaining accurate measurements is difficult near the diffraction limit. We imaged a subset of the surface by taking approximately 700 photographs of each witness plate analyzed. To prevent repeated counts and obtain as complete a sample as possible, we imaged each witness plate in a single session taking care to advance the microscope table sufficiently between images to avoid overlap. The optical configuration resulted in vignetting, with each image containing a vignette circle approximately 580 µm in diameter. In practice, a circular region about 480 µm in diameter is sufficiently well-focused to reliably identify holes. After processing, the total area analyzed for hole counting purposes corresponds to approximately 20% of the unobstructed surface of each witness plate.

We processed and analyzed the images using OpenCV with a combination of automated preprocessing and manual hole identification. We first pre-processed the images using a simple algorithm that identifies the vignette circle and well-focused region via thresholding, crops images to the vignette circle, and improves clarity by aligning the color channels to correct for errors introduced by the optical apparatus and camera sensor. Automated hole identification proved unreliable, so we manually identified holes in each image, defining a bounding box around each hole. Finally,

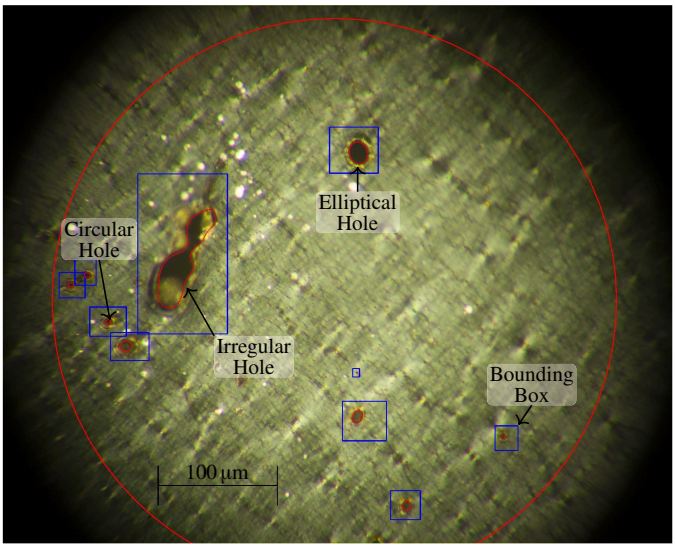

Figure 3.28: Witness plate micro-photograph with holes identified and outlined. We note representative examples of a circular, elliptical, and irregularly shaped hole, as well as the bounding boxes used in identifying holes for measurement. The red circle indicates the boundary of the well-focused region, inside of which we search for holes.

we measured the area of each hole, in pixels, by magnifying the bounding box regions, identifying points on the boundary, and fitting a bounded curve. We fit circular and elliptical holes using a least-squares method, and irregularly-shaped holes using closed cubic spline curves. Figure 3.28 shows a processed micro-photograph with holes identified. We converted pixel measurements to real units by calibration against an object of known size.

A rigorous discussion and quantification of error sources and uncertainties is lacking in many studies. In this study we attempted to quantify uncertainties to the greatest extent possible, and to propagate these errors in our estimates of the particle size distribution. First, we made multiple calibration measurements, and found a minor uncertainty ($<1\,\%$) in the conversion from pixels to real units. Second, by analyzing a subset of 100 images from each witness plate over five independent trials, we built an uncertainty model to account for human error in hole identification and measurement. Third, we found a systematic undercount of small holes near the boundaries of the vignette circles due to variable focus and brightness in the images.

We account for the measurement uncertainties by treating each measured hole area as an independent random variable and resampling the areas of all measured holes over 10,000 independent trials. During each trial, we first resample the pixel to real unit conversion based on the calibration uncertainty, and then account for human error by independently resampling the size of each hole assuming the relative error is a Gaussian random variable with variance $\sigma^2(A) = \sigma_{\mathrm{m}}^2(A) + \sigma_{\mathrm{id}}^2$. The relative measurement uncertainty $\sigma_{\mathrm{m}}(A)$ depends on the area because an equivalent absolute error results in a larger relative error in small holes compared to large holes. In practice, a constant relative error term σ_{id} well approximates the uncertainty due to human error identifying holes. After resampling, we apply a correction to each trial to conservatively correct for the under-counting.

In addition to the aforementioned errors, the cumulative distribution suffers from finite count effects, with small number statistics especially important for large holes. Given a set of holes with

areas $\{A\}_i$ corresponding to trial i from the resampled data, the number of holes with area greater than A is $N_i(>A)$. We model $N(>A)$, the true count of holes with area greater than A, as a Poisson-like process, allowed to be continuous for numerical reasons. Under these assumptions, if we apply the Bayes theorem with a uniform prior, the number of holes with area greater than A is a random variable with cumulative distribution [43]

$$F_i(x, N_i(>A)) = \frac{\Gamma(x, N_i)}{\Gamma(x)} \tag{3.4}$$

where $\Gamma(x)$ is the gamma function and $\Gamma(x, N_i(>A))$ is the upper incomplete gamma function. By linearity, averaging over the $M = 10000$ independent trials, the cumulative distribution of $N(>A)$ is estimated by $F(x) = \frac{1}{M} \sum_{i=1}^{M} F_i(x, N_i(>A))$. Finally, we numerically invert F to obtain an estimate for $N(>A)$ and associated uncertainty band for a given hole area A.

Beyond the error sources we are able to quantify, there are some sources we were unable to model explicitly. For example, the assumption of the hole size being equal to the incoming ejecta may be violated for particles approaching the film thickness. Quantifying this error is difficult, however, without an accurate material model and knowledge of the velocities of the microscopic ejecta. Moreover, individual witness plates only cover a small portion of the ejecta cone, so spatial variations in the ejecta density may influence results. Nevertheless, such errors plague virtually every study, and we do not expect excessive influence on the overall nature of the results.

3.4.1 Ejecta size distributions

We present the solid-angle normalized ejecta size distributions for the regolith simulant and aluminum impacts in Figures 3.30 and 3.31, respectively. We limit our analysis to holes at least 1 μm in diameter because the assumption of the hole cross-section matching that of the particle is violated for particles smaller than the film thickness and measuring holes reliably becomes difficult near the diffraction limit. We present results in the form of the cumulative distribution $n(>A)$, defined as the solid-angle-normalized number of particles producing holes with cross-sectional area greater than A. For comparison with the literature, we define the equivalent diameter d_{eq} such that $\pi d_{\text{eq}}^2/4 = A$, and we recast the power law as $n(>A) \propto A^{-D/2}$ to compare our results with D-values from previous studies.

Based on our measurements, we also compute the expected cumulative number of detections for a plasma sensor with cross-section 1.6 mm^2. For the co-located plasma sensor, we predict approximately 250 secondary impacts by ejecta at least 1 μm in diameter for the regolith simulant impact, and approximately 25 for the aluminum impacts. To compare with plasma measurements, we processed the filtered Faraday cup data with a continuous wavelet transform using Morlet wavelets [88] with non-dimensional frequency $\omega_0 = 6$. Secondary impacts by charged dust deposit their charge on a time scale much faster than the plasma sensor response time and are detected as impulses. Such impulses in the plasma data manifest as thin vertical bands in Figure 3.29, which shows the wavelet-transformed data for the regolith simulant impact and one representative aluminum impact. We found order of magnitude agreement with predicted dust impacts, counting approximately 5–10 such bands in a given aluminum impact, and approximately 40–50 from the regolith simulant impact. The discrepancy from the prediction may simply be due to spatial variations, but the difference suggests ejecta smaller than approximately 2–3 μm may not be detectable by the plasma sensors used in the experiment.

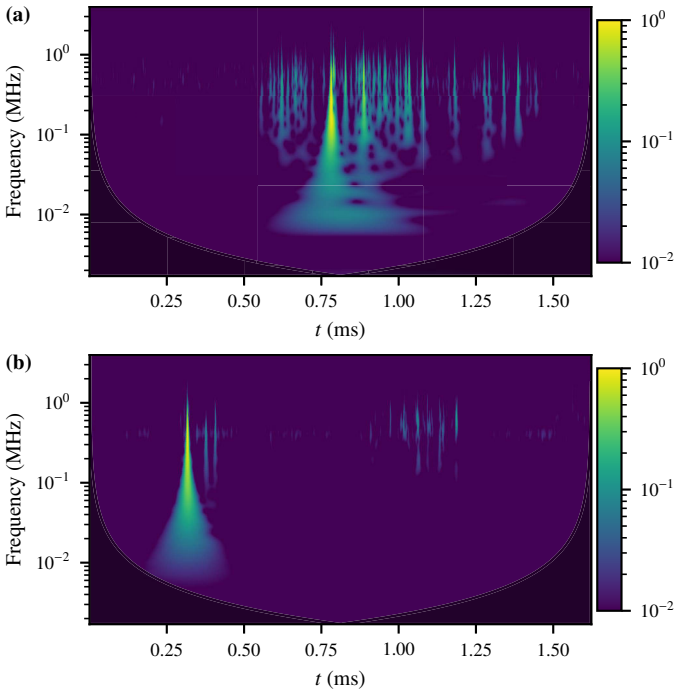

Figure 3.29: Wavelet transforms of Faraday cup plasma measurements from sensors located in the ejecta curtain. **(a)** Regolith simulant impact (90° from the horizontal). **(b)** Aluminum impact (90° from the horizontal). Thin vertical bands indicate impulsive observations, which likely correspond to dust detections due to secondary impacts by charged ejecta. The magnitudes are normalized by the maximum value observed for each shot.

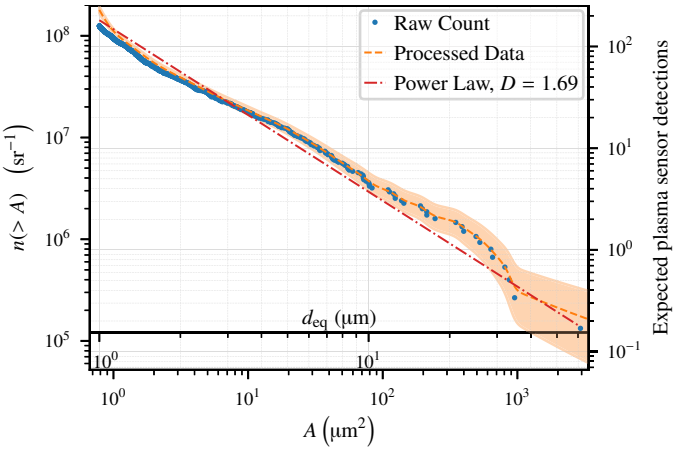

Figure 3.30: Solid-angle normalized particle size distribution for the powdered regolith simulant impact. Blue dots show the raw measurements. The orange line indicates the estimated distribution after resampling using the uncertainty model, applying corrections, and accounting for finite-count effects, with the shaded region indicating the 1-σ uncertainty band. The dashed-dotted red line shows the best fit D-value of 1.69.

The predicted particle flux to a sensor in the regolith simulant ejecta curtain is only 10 times greater than the predicted flux to a sensor in the aluminum ejecta curtain, despite the regolith simulant ejecting 400 times the material by mass. This is because the aluminum debris are concentrated in a much narrower band than the regolith ejecta. Based on the trend observed we predict a larger number of secondary impacts by particles on the order of ~0.5–1 μm. A basic drag analysis, however, suggests the 0.5 Torr neutral background in the test chamber will prevent particles much smaller than 0.5 μm from reaching the sensors, and the plasma may also ablate these nano-scale particles.

For the impact on the regolith simulant, after data processing and uncertainty analysis, we computed $D = 1.69^{+0.04}_{-0.03}$. After impact, we found a net change in the target mass of 14 g, or 3.3 % of the initial 420 g. Most hypervelocity impact studies on planetary materials have observed larger D-values, but the value does fall in the range observed for impacts on basalt slightly below the critical specific energy [11, 84, 27]. It is unclear how to define a critical specific energy for a powdered target, but the specific impact energy of $Q = 0.22$ falls in the transition range where targets are neither semi-infinite nor completely destroyed. Previous studies of other materials show D-values of 1.5–2 in that regime. Of course, for the powdered target, the level of compaction and pre-impact grain size distribution likely play major roles in determining the ejecta properties. For ejecta 1–50 μm in diameter, the measured quantity per solid angle agrees well with disruption experiments of basalt with normal impact angle [70].

For the aluminum impacts, the observed cratering is in good agreement with previous experiments, e.g. [72]. The average quantity of material ejected was 43 mg, about 7 times the projectile mass and 0.07 % of the target mass. Our results support the observation by Nishida et al. [72] that the NASA breakup model [44] significantly overestimates the relative abundance of ejecta below a certain size. We found, however, the bilinear exponential form used by Nishida et al. for macroscopic ejecta was also poor fit to our data, significantly underestimating the relative abundance of microscopic particles. We found a power law to be the best fit to the data and, after data process-

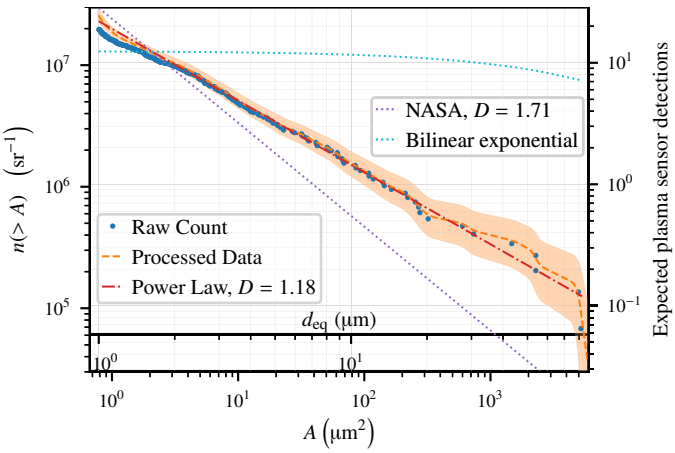

Figure 3.31: Solid-angle normalized particle size distribution for the aluminum impacts. Blue dots show the raw measurements. The orange line indicates the estimated distribution after resampling using the uncertainty model, applying corrections, and accounting for finite-count effects, with the shaded region indicating the 1-σ uncertainty band. The dash-dotted red line shows the best fit D-value of 1.18. Fitting to the NASA breakup model [44] D-value of $D = 1.71$ (dotted purple), overestimates the relative abundance of fine ejecta. Fitting to the bilinear exponential with exponent values proposed by Nishida et al. [72] (dotted cyan), significantly underestimates the relative abundance of fine ejecta.

ing and uncertainty analysis, computed $D = 1.18^{+0.10}_{-0.07}$. Note that the smallest particles measured by Nishida et al. ($\sim$500 μm) are larger than the largest ejecta we recorded ($\sim$100 μm), and further study is needed to patch the transition between macroscopic debris visible to the naked eye and microscopic debris on the order of or smaller than the material grain size.

3.4.2 Ejecta shape

We use two simple metrics to characterize the shape of debris particles. For a hole with area A and perimeter P, we define a simple, dimensionless circularity metric $4\pi A/P^2$, which is unity for a circle and less than one for any other shape. For comparison with the results of Nishida et al. [71] examining macroscopic ejecta from aluminum targets, we also consider the axis ratio b/a, where a is the major axis and b is the minor axis. For irregularly shaped holes, we compute b/a based on the axis ratio of the best fit ellipse. In Figure 3.32, we show the circularity metric versus hole area and in Figure 3.33 the cumulative distribution of axis ratios, $N(\geq b/a)$, defined as the number of holes with axis ratio at least b/a. We find that secondary impacts from larger particles result in holes with less circular and more irregular cross sections. Note in practice we generally classified holes with $d_{\mathrm{eq}} \lesssim 1.5\,\mu$m as circular because it is difficult to resolve the shape near the diffraction limit, but the trend for holes larger than approximately 2 μm is clear. We considered the possibility of irregular holes resulting from multiple overlapping secondary impacts, but at the $\sim$1 m distance, the ejecta density is sufficiently small that overlapping impacts are improbable.

The regolith simulant impact shows a more obvious trend towards less circular ejecta for $d_{\mathrm{eq}} \gtrsim 3\,\mu$m compared with the aluminum impact, where there is a mixture of nearly circular and highly irregular ejecta for the range of $2 \lesssim d_{\mathrm{eq}} \lesssim 15\,\mu$m. In agreement with [71], we find that the bulk of

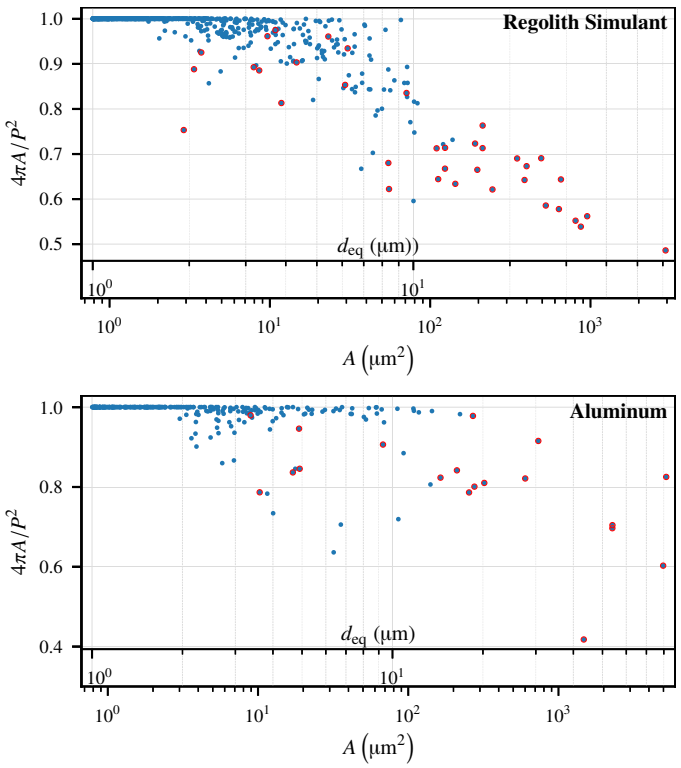

Figure 3.32: Hole circularity metric versus hole size for the regolith simulant and aluminum impacts. A red outline indicates the hole is irregularly shaped.

aluminum debris have $0.8 \lesssim b/a \lesssim 0.95$, in contrast to the regolith ejecta, where the distribution of axis ratios is more uniform. Holes with cross-sectional area $A \gtrsim 100\,\mu m^2$ are predominantly irregular in shape for both the regolith simulant and aluminum impacts.

A key question is whether we can glean anything about the material phase based on the shape of ejecta. Highly non-circular or irregular ejecta likely correspond to solid material ejected from the impact crater, and particles that produce smooth, nearly circular cross-sections more likely correspond to material ejected as liquid-phase droplets. Possibly due to aluminum fragments on the order of the material grain size having highly irregular shapes, a larger proportion of ejecta from the aluminum impact made irregular impressions compared with ejecta from the regolith simulant impact. At the same time, the impact process in solid aluminum produces a larger fraction of molten material. We suspect the existence of a significant population of nearly spherical ejecta up to almost 20 µm in diameter is due to liquid droplets ejected from the aluminum target. Drawing such conclusions for the regolith simulant impact is more difficult because the target is composed of a granular medium. A large volume of solid particles is ejected on impact and observations depend strongly on the initial target composition.

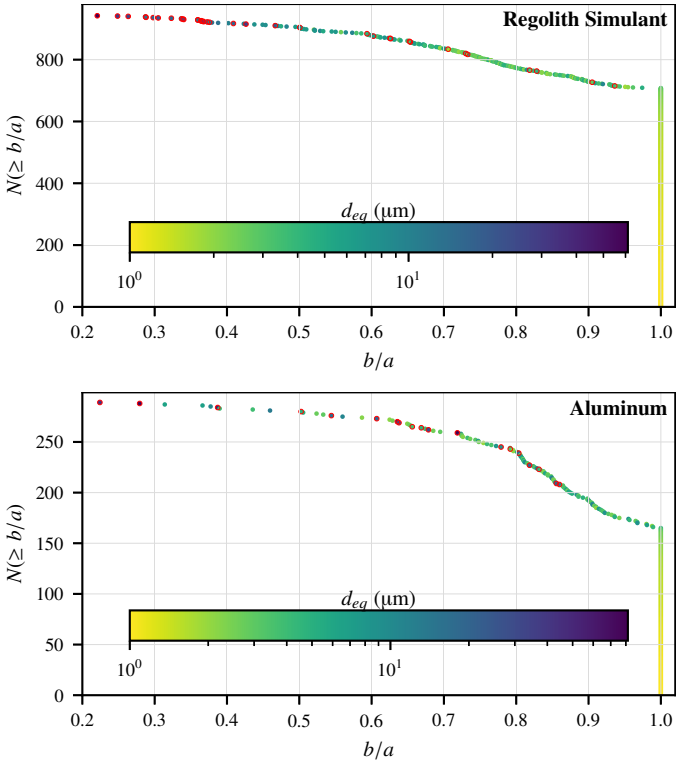

Figure 3.33: Cumulative distribution of minor-to-major axis ratios of holes due to debris from the regolith simulant and aluminum impacts. Points are shaded by equivalent diameter, d_{eq}, and a red outline indicates an irregularly shaped hole.

4 Modeling

This chapter outlines the modeling efforts that were undertaken to interpret the measurements described in the previous chapter. Primarily, these models focused on understanding the gas dynamic effects from hypervelocity impact plasmas expanding into a collisional background atmosphere, as was the case with the AVGR facility, and on the charge imparted to dust particles generated by the impact and traveling through the plasma.

4.1 Gas Dynamic Influence

For a background pressure of 0.5 Torr, as was used in these experiments, the mean free path is approximately 0.1 mm. To be a true vacuum, the mean free path should have been at least on the order of the size of the chamber, 1 m, if not greater. The remainder of this section will focus on the gas dynamics of the aluminum shots with three goals. First, we will identify the main gas dynamic effects. Second, we will calculate properties of the plume from analytic models of these dynamics.

4.1.1 Plume Features

In the high speed images from AVGR numerous plume shape features that can be observed. It should be noted that the plume is only visible when the plume is hot enough to emit visible light and dense enough for there to be enough light to be seen. Other processes such as recombination can also emit light [33]. These plume structures are the consequence of complex gas dynamics including instabilities and shocks. Onset and severity of these features depends on the material of the plume, speed of plume, and background gas density. A clear example of the influence of these variables was observed during our prior 2015 AVGR campaign, as shown in Figure 4.1.

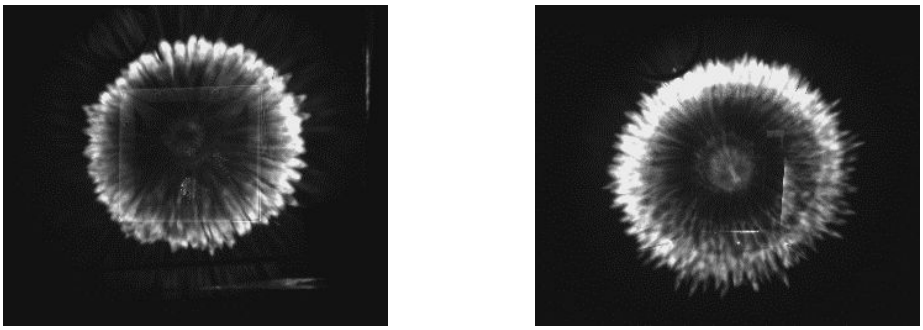

(a) (b)

Figure 4.1: (a) plume from an impact on a cubesat analogue (b) plume from an impact on a solar-cell and support structure

As can be seen in these images, the plume shape is very different between the two shots, even though the projectile speed and background density are roughly similar. Both images are at roughly the same time after impact (within 1 μs due to uncertainty in the image timing), and both plumes

are at roughly the same position indicating that the plume velocities are similar. As such, the observed differences are due to the differences in materials and densities of the plumes. The left picture is primarily aluminum and has more rounded plume features while the right is predominantly silicate material and has jagged features. This showcases the importance of material on the plume properties. These features themselves are the result of an instability in the plume.

Both a Richtmyer-Meshkov instability (RMI) and Rayleigh-Taylor instability (RTI) appear to have occurred based on the high speed footage for all of the metallic shots. The characteristic bubble and spike geometry on the contact surface can be seen in many of the high-speed footage frames presented so far. As additional evidence the top-down view of the evolution of the plume for shot 7 on aluminum is given in Figure 4.2. In this figure the transition of the bright plume front from a relatively smooth surface with a few contours to multiple triangular spikes can be observed. Triangular spikes such as these arise after the tip of the RTI spikes have undergone a Kelvin-Helmholtz instability.

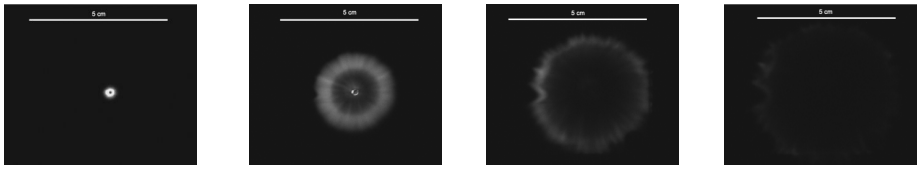

(a) (b) (c) (d)

Figure 4.2: Top down view from the vertical Shimadzu camera of the evolution of an aluminum plume. The contact surface is clearly visible, as are the spikes from the Rayleigh-Taylor instability. The images are roughly 3 through 6 μs after impact.

These instabilities have been reported in laser plasma experiments with similar background pressures [31, 53] to the AVGR tests. The RMI occurs first due to the impulsive initial expansion of the plume into the background gas. The RTI occurs at a later time once the contact surface has propagated some distance into the background and is being decelerated, creating the contact surface and the spikes of the instability. These dynamics have been observed during laser-driven radiative shock experiments [37]. We theorize that the front of electrons, observed in the experiment data, amplifies this instability by accelerating a front of ions from the contact surface through electrostatic forces and observed in the experimental measurements in Chapter 3. Evidence of both instabilities is seen in Figure 4.3 which shows that in all bias cases the plume decelerates (from drag during the RMI) from some value before reaccelerating (from spike acceleration of the RTI and electrostatic acceleration from the electron front) after 2 to 3 cm.

As can be seen, the plume appears to start from high velocity, slow down, and then go back to a roughly constant velocity. This is for the outer plume. The instability itself results from the ”snowplow” effect. As the impact plume expands it sweeps up the background gas causing it to build in density in front of the plume, much like snow builds in front of a plow. Eventually enough background gas has been swept up and compressed that the background density exceeds the density of the impact plume. The impact plume is then the less dense material and, as the impact plume is being decelerated the acceleration vector is pointing from heavy to light material, the Rayleigh-Taylor instability can form. This idea is given in cartoon form in Figure 4.4 to aid in visualization.

As a starting point for understanding what is happening with the gas dynamics during these impacts we can turn to stellar astrophysics. The gas dynamics in these impacts is similar to those observed in supernovas and laser ablation experiments that simulate supernovas. In supernovas a

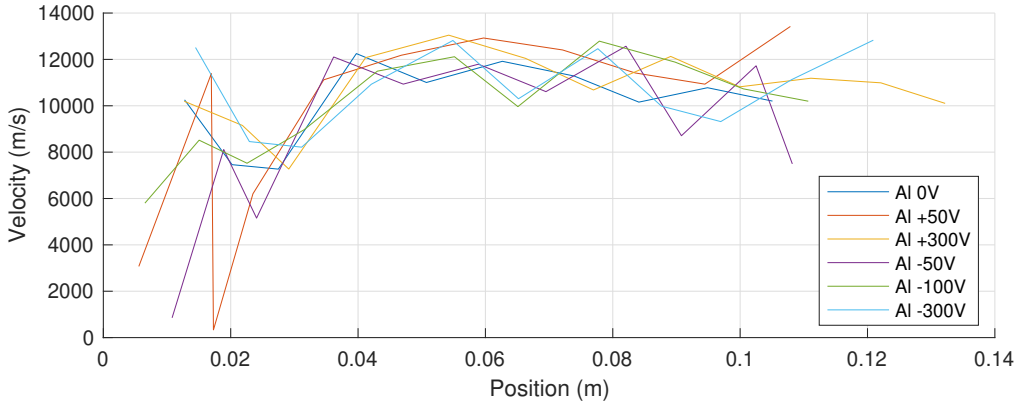

Figure 4.3: Velocity evolution from pixel tracking on the high-speed cameras. Multiple biases are presented for comparison. The plume appears to slow down, and then speed back up. The speeding up is attributed to the onset of the Rayleigh-Taylor instability.

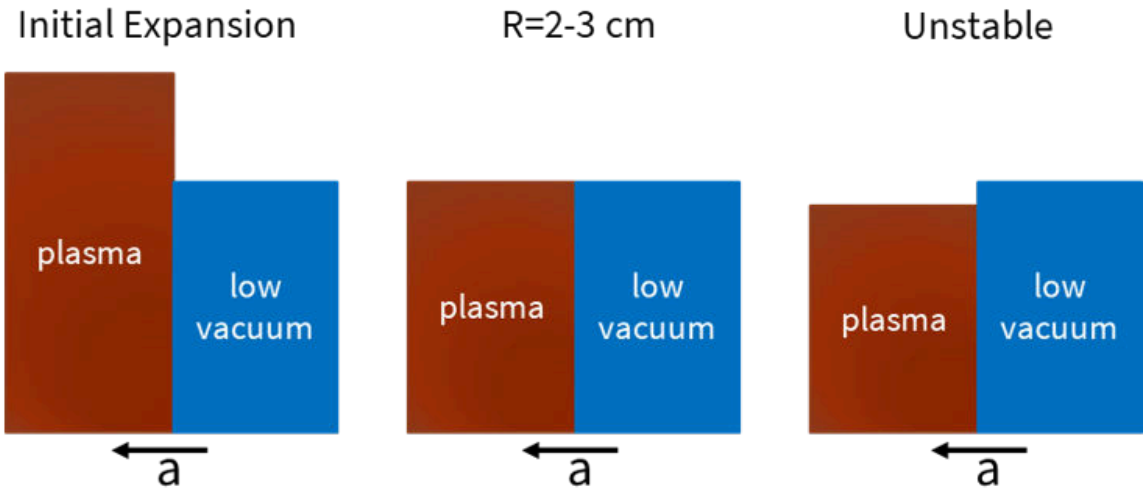

Figure 4.4: Schematic depicting how the correct density relations form for the genesis of the Rayleigh-Taylor instability.

dense and heavy gas - the main stellar matter- expands impulsively outwards into a low density and light gas - the stellar atmosphere of helium -. This impulsive accelaration can initial cause a Richtmyer–Meshkov instability. Over time the light material builds up in front of the plume font, increasing in density, in a process called snowplowing. Eventually enough of the light material has been built up that it is more dense than the bulk stellar matter and a Rayleigh-Taylor instability can form.

The clearest example of the formation of the instability and instability features was seen during the test shot, referred to as shot 0. As can be seen in the top down part of Figure 4.5 the plume clearly has long skinny spikes that then transition into more triangular features. The skinny spikes are the spikes of the RTI and the triangular features are, as mentioned above, the result of those

spikes undergoing another instability. Included in this figure is also a sideview of this plume. In this view the spikes are again visible and they can be seen to be multilayered. This instability is clearly a 3D effect. Also viewable in the side view is the outer plume, as was seen in the other AVGR shots. Out in front of the spikes a blue region can be observed to propagate.

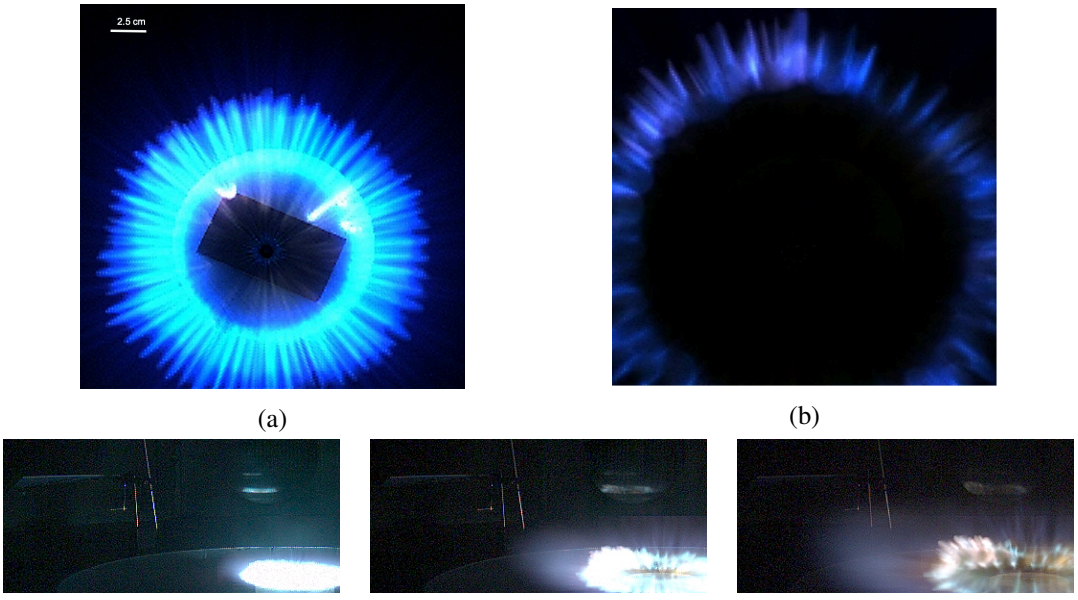

Figure 4.5: (a)-(b) Phantom camera vertical view of the plume from shot 0 on a thin copper plate. The contact surface is the smooth ring from which Rayleigh-Taylor instability spikes originate. (c)-(e) side view of the plume from shot 0.

Additional features in the plume can be viewed by altering the contrast, brightness, and sharpness of the images as shown in Figure 4.6 for aluminum and 4.7 for copper. These aluminum images are the same ones presented in Figure 4.2. Each individual picture has been hand adjusted to bring out the most detail in the plume. In the aluminum images the transition from smooth bumps on the surface to spikes is much more clear with these image changes. The edge of the contact surface itself is distinct in these images. That said, the contact surface is a 3D phenomenon. Therefore, it is impossible to distinguish what is internal to the plume or on the upper surface. It is possible that the darker regions around the early aluminum images are the shock as some material is expected to be in front of the contact surface and behind the shock. The region does appear to grow, but it is not possible to confirm whether this is the shock edge or not. Features are visible inside of the plume for the last aluminum image and the copper image. These features are likely part of the plume resulting from ablation in the crater. The direction of propagation is unclear, but the spike features in the copper image implies horizontal movement. This part of the plume is likely driving the contact surface forward from behind. The periodic pattern internal to the copper image could be a result of the jagged crater edge or due to something like the Wiebel instability causing striations in the density and temperature.

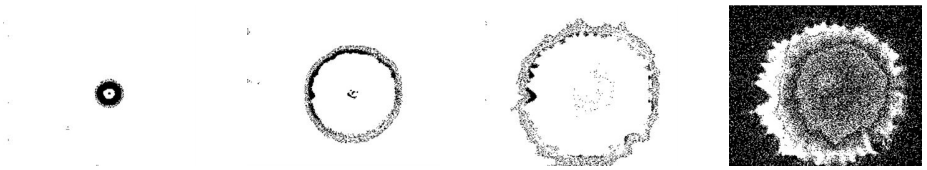

(a) (b) (c) (d)

Figure 4.6: Top down view from the vertical Shimadzu camera of the evolution of an aluminum plume with altered contrast, sharpness, and brightness to highlight plume details. The contact surface is clearly visible, as are the spikes from the Rayleigh-Taylor instability. The images are roughly 3 through 6 μs after impact.

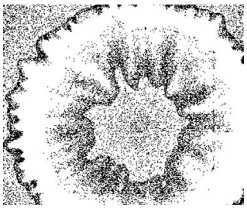

Figure 4.7: Top down view from the vertical Shimadzu camera of the copper shot. The contrast, sharpness, and brightness are altered to highlight plume details.

4.1.2 Jetting Velocity

In order to investigate the gas dynamics and understand their effects we first need to approximate the plume velocities from jetting during impact. Based on projectile size and velocity the impact is approximated to take on the order of 100 ns. The 1 μs resolution of the imaging systems used during these tests limits the precision of the jetting velocity measurements.

Impact jetting is the mechanism that starts the gas dynamics during the impact process. Impulsively accelerated material collides with the background and starts sweeping it up. Specific values for the jetting at AVGR can be calculated using formulations from literature [54, 93]. The velocity of the initial jet and the angle of the initial jet can be found in Figure 4.8.

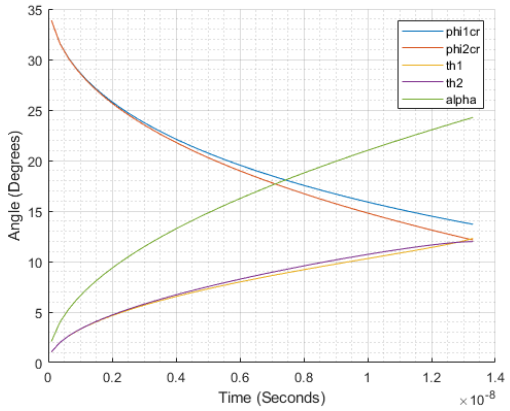

Figure 4.8: Calculation of the jetting onset time and angle for shot 10.

Jetting starts roughly 1.8e-8 seconds after impact with the tangent angle between the projectile and target of around 24° above the horizontal and the jet at an angle of 12° from the horizontal. The jetting will continue until 1.5e-7 seconds after impact when half of the impactor has penetrated the target. Initially the jet can have a velocity upwards of 18 km/s, but the mass during this point of jetting is essentially 0. Mass and an approximate velocity change in the jet can be found in Figure 4.9.

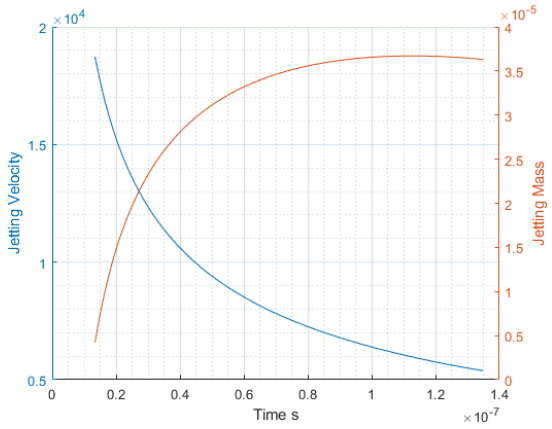

Figure 4.9: Calculation of the jetting mass and velocity for shot 10.

4.1.3 Shock

The high-velocity jetting of a plasma into a non-negligible background pressure is expected to create a shock. In the experiments performed the shock shape and location in the chamber is not exactly known, because the camera systems are unable to detect density gradients and the standard self-similarity formulations do not explicitly hold at these pressures [31]. That said, many laser ablation experiments succesfully use self similar formulations to match the observed dynamics.

Due to their mobility it is expected that electrons would be, at least initially, out in front of the ions and either be entrained in the shock or slightly behind it. This front of electrons can set up an ambipolar electric field which can then accelerate the ions. The influence a shock may have on RF emission is unknown, as the shock may act as a physical barrier impeding electron motion including altering the electron oscillations or it may cause further charge separation by pulling more mobile entrained electrons away from the ions.

4.2 Blast wave analyses

There are a number of first order analyses for gas dynamics that are relevant for this impact system. A few different analyses will be presented and their ability to capture the plume dynamics will be analyzed.

4.2.1 Taylor Blast Wave

Impulse induced blast waves are often analyzed using some form of similarity analysis. Both the impact and the rapidly expanding gas could create a shock in the background material which then

expands self-similarly with respect to the initial geometry. Analytic formulations of a blast wave propagation has been developed by Taylor-Sedoz [87] and Freiwald [25] (updated by Hutchens [38]). It is worth noting that according to the findings of Kapitan [48] and Grun [29] the background pressures used during testing are either lower than or at the edge of applicability for similarity analysis. The reason for this is the width of the shock is on the order of the mean free path of the background gas. Again, the mean free path is approximately a tenth of a millimeter for these experiments.

It is common to model the expansion of a hypervelocity impact or laser ablation plumes (which share a lot of similar evolution traits) as a blast wave [66][31][28]. For the experiments presented here, the speed of expansion of the outer plume was attempted to be described by both the Taylor-Sedov and updated Friewald formulations. For the Taylor-Sedov formulation we find the radius of the expansion in meters, R, using

$$R = \xi \left(\frac{E}{\rho_0}\right)^{1/5} t^{2/5} \tag{4.1}$$

$$\xi = \left(\frac{75}{16\pi} \frac{(\gamma-1)(\gamma+1)^2}{3\gamma-1}\right)^{1/5} \tag{4.2}$$

where ρ_0 is the background gas density,γ is the ratio of specific heats for the background gas, and E is the energy of the blast. In this case E is taken to be 1/2 the impact energy.

This spherical formulation was attempted to track the outer plume as well as the arrival of signal to the lower sensors. Both the classic formulation and the modifications by Mihaly [66] were tried. Results of this analysis can be seen in Figure 4.10.

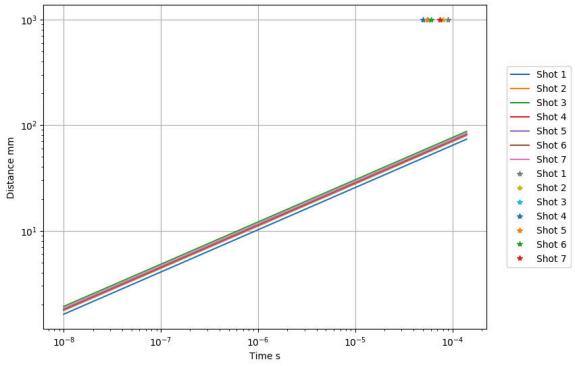

Figure 4.10: Results from the spherical Taylor blast wave analysis.

As Mihaly found, the classic formulation fails to track well but the modifications get close. Unfortunately all this tells us is that the plume evolves self similarly as the modifications break the assumptions that the formulation was derived from. A cylindrical blast was also tried, as shown in Figure 4.11, but this too was not a good match. This is likely because the height of the cylinder is also changing as the plume propagates, breaking the self-similarity. An increase in height of the plume would slow the plume down, which could account for the observed error. A cylindrical blast wave may be a good fit for a few μs at the beginning of the expansion, where the height is not changing much. This though would not allow for the goal of analyzing if the signal of the lower sensors coincided with a propagating shock.

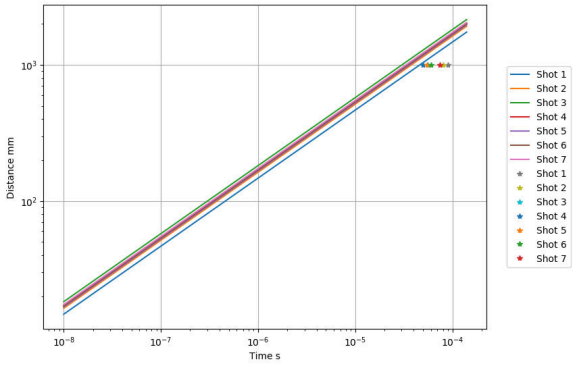

Figure 4.11: Results from the cylindrical Taylor blast wave analysis.

4.2.2 Taylor Blast Wave with Source Mass

An improved extension of blast wave theory is to also include the influence of a source mass. This mass can have inertia and therefore change the propagation of the shock. The Freiwald formulation obtains the radius of the shock over time by numerically integrating the radius growth rate $\dot{R}$ described by

$$\dot{R} = \sqrt{\frac{E}{K_1 + K_2 R^{N+1}}} \tag{4.3}$$

where K_1 and K_2 are coefficients

$$K_1 = \frac{C_N}{N+1} \frac{2\rho_s R_s^{N+1}}{(\gamma_g + 1)^2} \tag{4.4}$$

$$K_2 = \frac{C_N}{N+1} \frac{2\rho_0[(\gamma_g + 2\gamma_d) - 1]}{(\gamma_g + 1)^2(\gamma_d - 1)} \tag{4.5}$$

N is 1 for a cylindrical expansion and 2 for a spherical expansion. C_N is $2\pi L$ for cylindrical and 4π for spherical. The initial density of the expanding gas is ρ_s, while ρ_0 is the initial density of the background gas. R_s is the initial radius of the expanding gas. In all calculations performed the two specific heat ratios, γ, were assumed to be the same. The subscript g is for the background gas while d is for the driving gas.

Spherical and cylindrical expansions were again used with the same goal as in the Taylor blast wave analysis above. The initial density of the expanding gas was taken to be 100 times the plasma density to account for the non-ionized vapor. Both formulations over-predicted the initial expansion rates observed and under-predicted plasma arriving at the sensor as shown in Figure 4.12 and 4.13.

Likely, one of the reasons these formulations and the Taylor blast wave fail to match what is observed is due to the glowing region seen not being coincident with the shock front. Instead, the shock is likely further out from the point of impact at the times where the fit was attempted and the visible portion of the outer plume is likely not the entire extent. Electrons out in the front of the plume would not emit light on their own and a lower density plasma may not emit enough light to actually be observed. Frame 2 of Figure 4.14 is the strongest evidence for the further out plasma from the AVGR experiments. In this frame the edges of the target can be seen to be glowing before the main plume reaches it. This suggests plasma exists at the target edge at this time, even though the main plume does not. This plasma could either be entrained in the shock or a little behind it. This distribution is not without precedent.

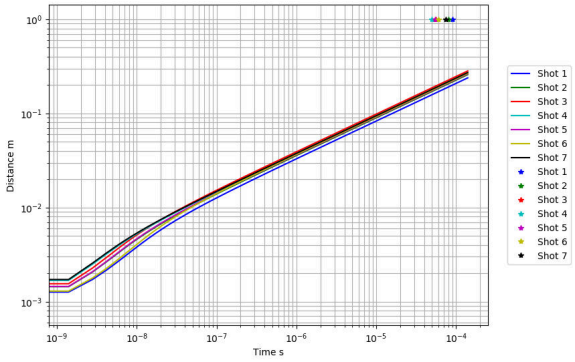

Figure 4.12: Result of the spherical blast wave analysis including source mass.

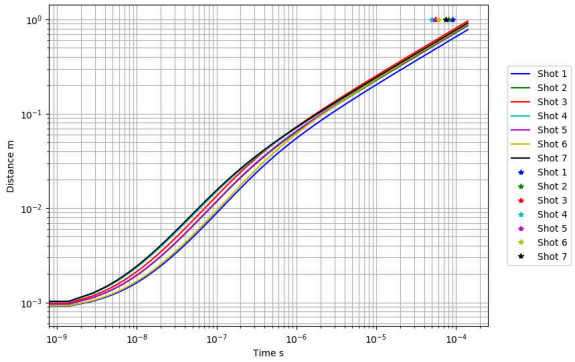

Figure 4.13: Result of the cylindrical blast wave analysis including source mass.

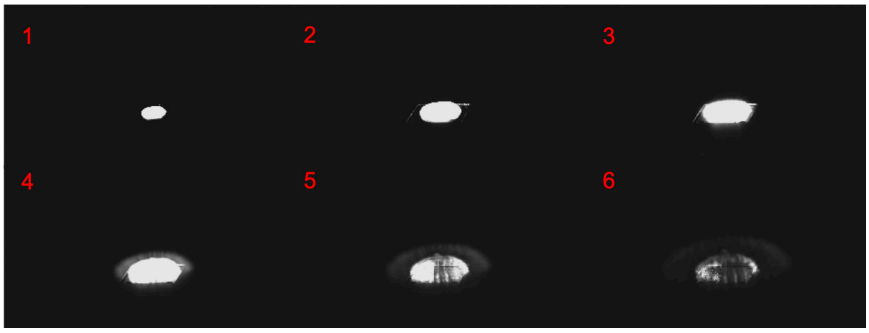

Figure 4.14: Evolution of the aluminum plume as viewed from the side. Each frame is 1 μs apart.

Both theories much better approximate the shock at the glowing edges compared to the expansion of the main plume. At later times the height of the expansion has increased too much that the self-similarity is no longer valid. Additionally, the impact is a time dependent process with material added to the plume over a finite amount of time. For the larger impactors at AVGR the target material is still ablating at 1 μs after impact, adding material to the plume. As such the assumption that all the mass is present at the beginning of the expansion is not valid. A better fit at the early times for these impacts could be achieved by making the mass a function of time. If the impacting mass was smaller the time of the impact dynamics would be less and the self-similar formulations may

be more valid.

4.2.3 Modeling of the Contact Surface

The bright internal expansions seen in the high-speed images, such as Figure 3.6, are the contact surfaces between the background gas and the plume. The ring that is the contact surface is sharply defined in this figure. This contact surface is a region of high mixing and collisions. The brightness is the result of recombination and potentially new ionization from the collisions [34]. Furthermore, this mixing increases electron-neutral interactions, which is one of the possible sources of RF emission, potentially causing a greater amount of RF emission than in a high vacuum environment.

This contact surface can be modeled using the formulation in [67] that derives the temporal evolution of the contact surface radius r_i assuming a cylindrical expansion and a contact surface traveling in a post-shock gas

$$r_i(t) = r_0 \left(\frac{t}{t_0}\right)^{2/\gamma(d+2)} \tag{4.6}$$

$$t_0 = \sqrt{\rho_p/E}\left(\frac{r_0}{\xi}\right)^{(d+2)/2} \tag{4.7}$$

$$\xi = (\gamma+1)^{1/2}\left(\frac{1}{h\pi}\right)^{1/4} \tag{4.8}$$

where r_0 is the radius of the crater which is roughly 0.25 cm for the aluminum shots, t is the time after impact, the parameter t_0 is the time it takes the shock to reach the interface, γ is the specific heat ratio of the background gas, E is the kinetic energy of the impact, ρ_p is the initial density of the plasma multiplied by 100 to account for the un-ionized vapor, d is a parameter that is set to 2 for a cylindrical expansion, and ξ is a shape parameter formulated for a cylindrical expansion. The height h of the cylindrical expansion was assumed to be 1 mm, based on pixel counting from the high-speed footage. Figure 4.15 shows examples of this analysis for three separate shots, as well as the radius of the contact surface from pixel counting. This clear matching between theory and observation, even in the case of a strong bias, shows the strong role gas dynamics play in the evolution of the plume even at these low pressures. Furthermore, these fits can be used to ascertain the initial density of the expanding vapor/plasma ρ_p, as this was not able to be measured directly. This density, converted to a plasma particle density and assuming 1% ionization, was found to be on the order of 10^{23} m^{-3} for the aluminum shots. This density matches the density that is calculated using the impact charge production approximated by Equation 4.9 [65] and assuming the plasma occupies a spherical volume with the radius of the crater. Here m_p is the projectile mass.

$$Q = .1m_p\left(\frac{m_p}{10^{-11}}\right)^{0.02}\left(\frac{v_p}{5}\right)^{3.48} \tag{4.9}$$

In contrast to aluminum, copper expanded much more rapidly. The fit for copper resulted in a density on the order of 10^{21} m^{-3}, two orders of magnitude lower than aluminum. Copper is a harder material, leading to less material being ejected and a higher jetting velocity.

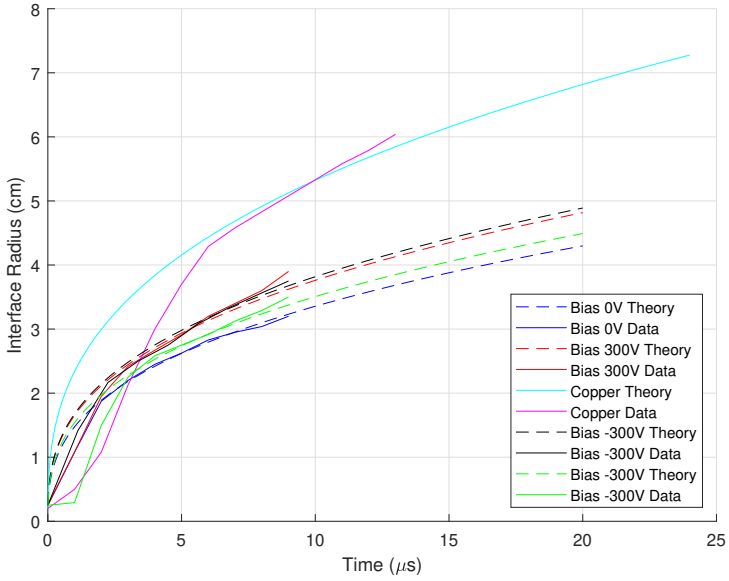

Figure 4.15: Comparison of the evolution of the contact surface found by pixel tracking to the theoretical evolution based on gas dynamics. The theoretical and actual results match up very well. Early time discrepancies can be attributed to the relatively low temporal resolution of the high-speed cameras in comparison to the speed of propagation of the plume. This close fit showcases the dominance of gas dynamics over electromagnetic forces.

4.2.4 Instability Modeling

The RMI is merely a RTI with an impulsive acceleration, in this case from the jetting. This instability develops over approximately the first 1 μs of expansion. As this is the time resolution of the cameras, exact analysis of this instability is difficult. We will therefore focus on analyzing the RTI. Onset of the RTI can be approximated by determining the point of maximum acceleration of the two fluid system using conservation of momentum [31]. Conservation of momentum for a gas at velocity v, assuming a cylindrical expansion, is formulated as

$$\frac{d}{dt}((M + h\pi R^2 \rho_{0,post})v) = 0 \tag{4.10}$$

$$R = \left(\frac{M}{h\pi\rho_{0,post}}\right)^{1/2} \tag{4.11}$$

The mass M of the expanding gas includes the mass of the un-ionized vapor and the plasma and can be found by assuming the plume takes up a cylindrical volume with height h and radius r_0. Substituting the experimental conditions gives an onset radius around 2 to 3 cm for an initial plasma density of 10^{23} m^{-3} as calculated in Section 4.3. This matches the location seen in the high-speed footage, such as Figure 4.2, where the onset of the two expanding fronts occurs and the radius where the plume reaccelerates, as shown in Figure 4.3. The analytic expression therefore gives greater confidence of the initial plasma density calculation and the presence of a RTI.

Existence of a RTI is further supported by the asymptotic velocity behavior seen in Figure 4.3. Both the bubble and spike velocity of a blast-induced RTI approach a roughly constant velocity as the instability evolves. Equation 4.12 gives the spike/bubble height evolution of the RTI as a function of time as derived in [67]

$$\frac{dz(t)}{dt} = \sqrt{\frac{|1-\eta|}{C_D}\lambda g_t(t)} + \beta\frac{z}{t} \tag{4.12}$$

$$g(t) = \frac{r_0}{t_0}\frac{2}{\gamma(2+2)}\left[1-\frac{2}{\gamma(d+2)}\right]\left(\frac{t_0}{t}\right)^{2\left[1-\frac{1}{\gamma(d+2)}\right]} \tag{4.13}$$

where β is a coefficient equal to $2/\gamma$(d+2) for an ideal shock, C_D is the drag coefficient with the value of $2\pi(1.22)$ for a 3D plume, η is the ratio of the plasma to the background density, z is the spike height relative to the contact surface, and γ is taken to be 1.3. Here the acceleration, $g_i(t)$, is that of the contact surface which we have already shown to be a good match to the measured evolution. The total acceleration is, $g_t(t) = g(t)(1 \pm \frac{z}{t}) + g_{em}$ where plus is for bubbles, minus for spikes, and g_{em} is acceleration from electromagnetic forces. From pixel counting the initial spike height is taken to be 1 cm. 40 spikes were counted in the high-speed footage for the second unbiased aluminum shot when the plume was at a radius of 2 cm, corresponding to a wavelength of approximately $\lambda = 2(.02)\pi/40$. Using these parameters a terminal velocity of between 8 and 12 km/s can be recovered. Ambiguity arises because the plume density drops as it expands, the mode number evolves over time, and the exact acceleration, especially the acceleration from electrostatic forces, is unknown. Still, how the RTI evolves in theory matches with what is observed.

The confirmation of both RMI and RTI through the strong correspondences between the analytic formulations and observations has three profound implications for these experiments and how they relate to what would be observed from an impact in space. First, as was shown, the propagation speeds are extremely dependent on the RMI and RTI spike evolution. In a space-like vacuum, it is expected that the plume would instead propagate at a velocity closer to the jetting velocity. Secondly, the spikes and bubbles of the RMI and RTI are regions of high amounts of mixing akin to the contact surface. Therefore these spikes and bubbles can be a source of electromagnetic fields [24]. This is especially the case if the instability enters the turbulent regime, which we did observe. In contrast, this source of RF emission would not be seen in a space environment. Finally, the spike and bubble geometry of this instability creates a periodic structure in the plume that would not be present in a vacuum. This variation could have directly influenced plasma sensor measurements as current and time of flight measurements could differ if a sensor measured a spike or a bubble, such as those shown in the figures in the previous sections above.

Electrons and Gas Dynamics

As shown in the previous section, electrons will move out to the front of the plume due to their mobility. These electrons will then accelerate ions due to the charge separation that is created. This ion acceleration will alter the gas dynamics from the systems that are described by the first order equations. Namely, the slowing down of the plume should be less and the acceleration of spikes should be more.

Furthermore, non-uniformity in the electron temperature can lead to a Weibel instability. This instability can cause density striations in the plume. This may explain the spiky nature of the outer

plume front as well and the periodic structures viewed inside of the plume. This instability would also drive the mode of the Rayleigh-Taylor instability.

4.3 Hydrodynamic Modeling

Although the first order gas dynamics models were somewhat successful in matching the observed dynamics and informing on some of the properties of the plume it is desirable to do better and gain more detailed descriptions. Numerous computer simulations of various types have been performed to try and model hypervelocity impacts. These codes take a number of forms including smoothed particle hydrodynamics, particle in cell codes, and general hydrodynamics codes. Each type of code and each implementation of that type has its own strengths, drawbacks, and stage of the impact process that is the focus. For example, hydrodynamics codes with material models such as iSALE do a good job capturing the crater formation and initial jetting while particle in cell codes capture the plasma dynamics of plume.

For the impacts performed at AVGR we are mainly interested in capturing the plume dynamics, most importantly the instabilities and any shocks that form. Given our low temperatures of around 0.3-0.5 eV we only expect roughly 1% ionization based on the Saha equation. As such, a particle in cell code or magnetohydrodynamics is not appropriate. Smooth particle hydrodynamics code can struggle to accurately capture instabilities if the particles are sized insufficiently, so a pure hydrodynamics code is the best option. We chose to use the FLASH code which is an open source code developed by the University of Chicago.

Within this simulation framework, we are mainly interested in what these simulations can tell us about the impact process, the evolution of the plume, and how the experimental environment influenced the measured results. To do this well, we also need to understand the limitations and caveats of the code to correctly restrict our interpretation. This section will start with an overview of FLASH, present simulations on an approximate top down view of the plume and then present simulations on a 2D impact simulation.

4.3.1 FLASH Code Overview

FLASH is a hydrodynamics and magnetohydrodynamics code written in FORTRAN90 with an adaptive mesh originally intended to be used to model stellar thermonuclear flashes. It has the capability to model partial ionization including different temperatures for ions, electrons, and radiation. Relativistic and non-ideal MHD effects such as the Hall effect can also be modeled. These additional features will not be used for the simulations in this dissertation. There are a number of solvers but we will use the unsplit hydrodynamics solver which is the default solver. This solver will be used to capture the fluid dynamics as well as heat transfer. Another physics unit, the diffuse unit, does exist which gives more control over heat transfer processes but the differences in results was found to be minimal. A complete description of FLASH can be found in the user manual. All results from this code will be presented in CGS units.

4.3.2 Instability Modeling

As stated previously, the instability arises due to the impact plume snowplowing the background gas, eventually creating a scenario where the plume is less dense than the built up background. Due to the high velocity of the initial jetting a shock in the background gas is also expected. The initial

modeling effort in FLASH was intended to show and explore these two ideas. Additionally, the goal was to match the top top down view of the AVGR cameras, or at least explain some of the features.

To capture the instability the plume was assumed to be a two dimensional disk. This is a common assumption made in the modeling of supernova instabilities using hydrocodes. To limit the computational effort only a quarter of the disk was modeled, with the left and bottom sides of the simulation domain set to be reflecting.

The initial radius of the plume was set to be 0.08 cm, or roughly the radius of the projectile. This radius was chosen to allow the initial jetting to start the shock close to the projectile radius. The jetting radius could have been 0.2 cm as that is roughly the distance the initial jetting travels, assuming no drag, during the entire jetting process. This is over double the projectile radius and an order of magnitude further than jetting actually starts from, so this would lead to inaccurate shock development. From 0 to 0.04 cm the density and velocity was set at a constant value to simulate the ablation stage. A linear profile for the density was found to be the best result.

The disk was slowly released over time starting with the outer most regions and working towards the origin. This simulates the addition of material during the impact process, but is merely an approximation. No perturbation was applied to the plume front to start the instability. The jaggedness of the plume front resulting from the Cartesian grid was found to adequately start the instability. The starting profile of the simulation is shown in Figure 4.16.

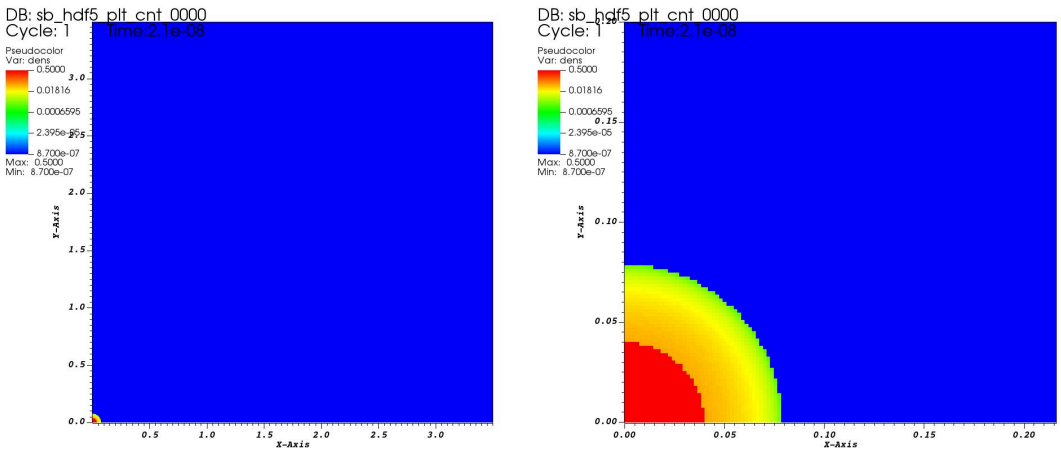

(a) (b)

Figure 4.16: Initial density profile for the disk FLASH simulations.(b) is the same profile as in (a) just zoomed in.

Diatomic nitrogen is used as the background gas with a γ of 1.4. This is accurate for the initial stages of background gas buildup. As will be shown, the temperature rise behind the shock exceeds the dissociation temperature of nitrogen. It is therefore likely that some nitrogen dissociates or even ionizes during the actual experiment. Error will arise in both the gas dynamics, due to the now incorrect γ, and the energy conservation as some energy will be radiated during the dissociation or ionization. Radiation energy can be captured in 3T FLASH simulations. With normal hydrodynamics the assumption is that the radiation energy is small and therefore negligible.

Base Simulation

Simulating shot 7 and 10, as they have similar conditions, was the primary focus. The shot background gas pressure was matched and the simulation was tuned such that the plume location as a function of time matched these shots. Figure 4.17 is a few timesteps of this simulation showcasing the evolution of the plume.

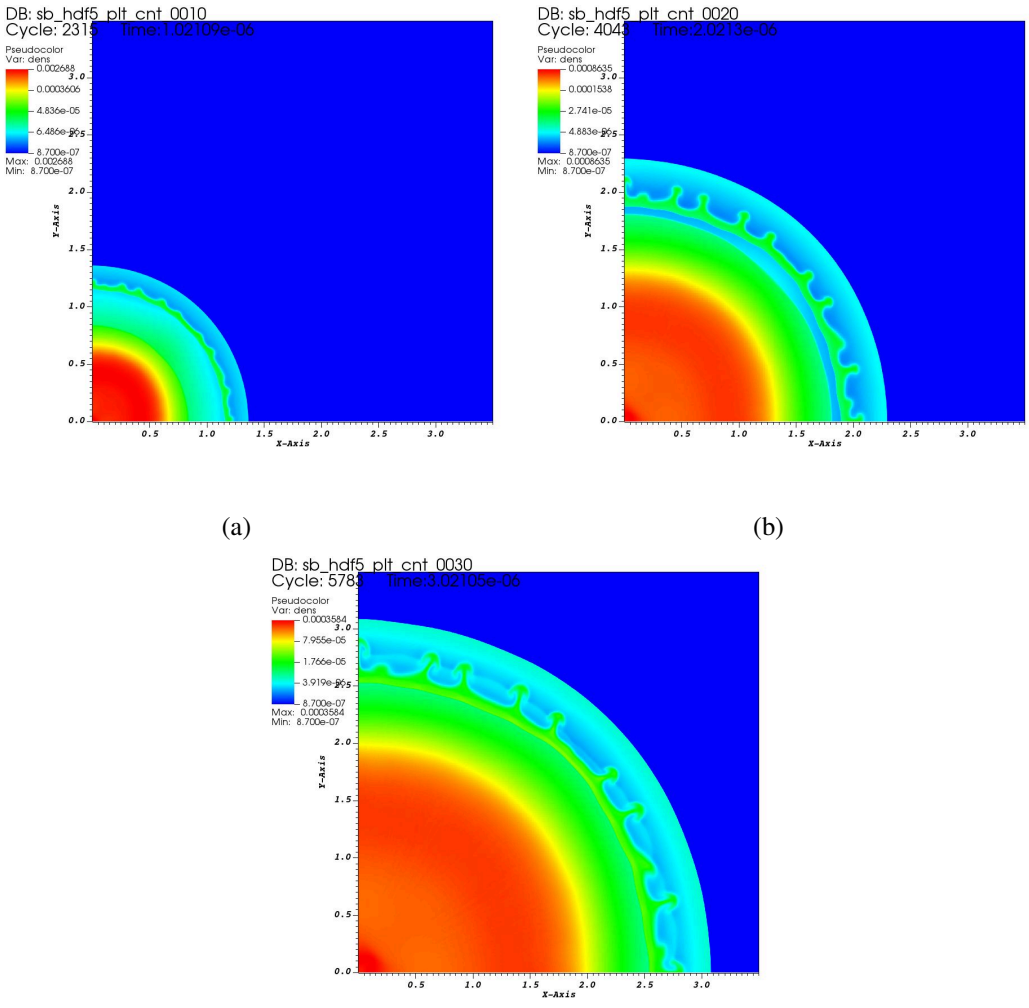

Figure 4.17: Results from the base disk simulation of the impact plume showing the onset of an instability. All plots show density in CGS units. Times are shown in each image in seconds.

From these images it is clear that a shock forms out in front of the plume as the front of the plume bunches up at the contact surface. This shock was expected, but this simulation is is the first time any information about it can be gained. As expected, it is out in front of the contact surface by a few tenths of a cm and gets further away as the simulation time increases. Whether or not this shock location matches the observed propagation of the outer plume would require a simulation

with a larger domain and longer runtime. This simulation does not directly capture the outer plume as it is likely a surface interaction and electrostatic phenomena.

The instability can be seen to transition from rounded structures to the spikes seen in the high speed images, such as in Figure 4.2, after the Kelvin-Helmholtz instability. Just as was seen in the high-speed the full instability onset is between 2 and 3 μs after impact at a distance of around 2 cm from the impact point.

Slowing and bunching of the plume due to the background as shown in these simulations complicates not only the interpretation of the plume but also the dust measurements. Significant drag on the dust can result as it moves through the plume. A plume slowed and bunched up by the background will therefore slow dust further than it would in a vacuum. Based on the drag analysis and the density of the plume in these simulations, a velocity change on the order of 100 m/s/μs should be expected. The bunching of the plume also means bunching of charge. Dust could also pick up more charge from a bunched plume than it would in vacuum.

The simulation shows that the bunching of the plume at the contact surface, along with the shock, causes a rise in temperature of the plume, as shown in Figure 4.18. This explains the observation of the bright contact surface. The peak temperature is at the interface between the plume and background. The edge of the plume is 3 eV at its edges while behind the shock can be over 5 eV. It should be noted that these simulations likely over approximate the temperature rise due to the simulation being only 2D. In 3D energy and momentum would be able to be dissipated by vertical movement of the plume and curvature of the shock.

Fundamentally this observation makes sense. In an ideal gas the temperature change in a fluid that changes velocity can be found by 4.14 where T is temperature, c_p is the specific heat at constant pressure and V is the velocity. As a fluid is slowed, as the plume is do to collisions with the background gas, the temperature has to increase. In the case of these experiments the velocity change is a few km/s. This is enough for a few eV rise in temperature. Such a rise in temperature may be enough to cause additional ionization in the plume after the impact ionization. Given that the ionization energy of nitrogen is roughly 14.5 eV it is unlikely that the nitrogen is significantly ionized. Aluminum only has an ionization energy of roughly 5 eV, so significant additional ionization may occur. It is therefore possible that the target voltage measurements are partly a response from collisionally ionized particles.

$$c_p T_1 + \frac{V_1^2}{2} = c_p T_2 + \frac{V_2^2}{2} \tag{4.14}$$

Effect of Profile

Input profiles to the base simulation were based on first order modeling of the jetting process. Validation of these models as input profiles not only checks the accuracy of the simulation but also checks the model. A simulation was performed with the density input profile as convex, instead of the linear profile shown above, with everything else held the same. The result of this simulation are in Figure 4.19. Density distribution is clearly important. The spikes of the instability are very different between the two cases. They are much thinner in this new simulation. Temperature also differs between the two cases with temperature being higher in the convex profile.

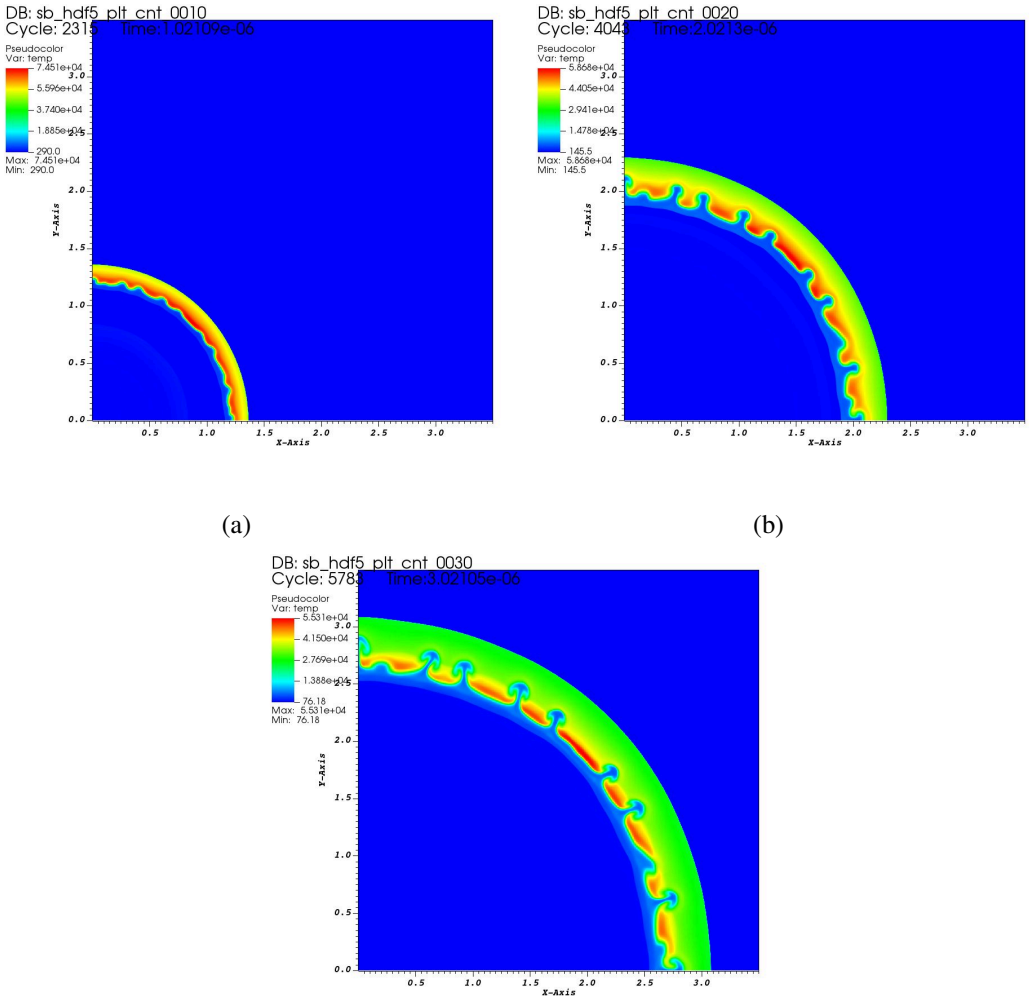

Figure 4.18: Temperature at a few different times for the base disk FLASH simulation. All plots show temperature in Kelvin. Times are shown in each image in seconds.

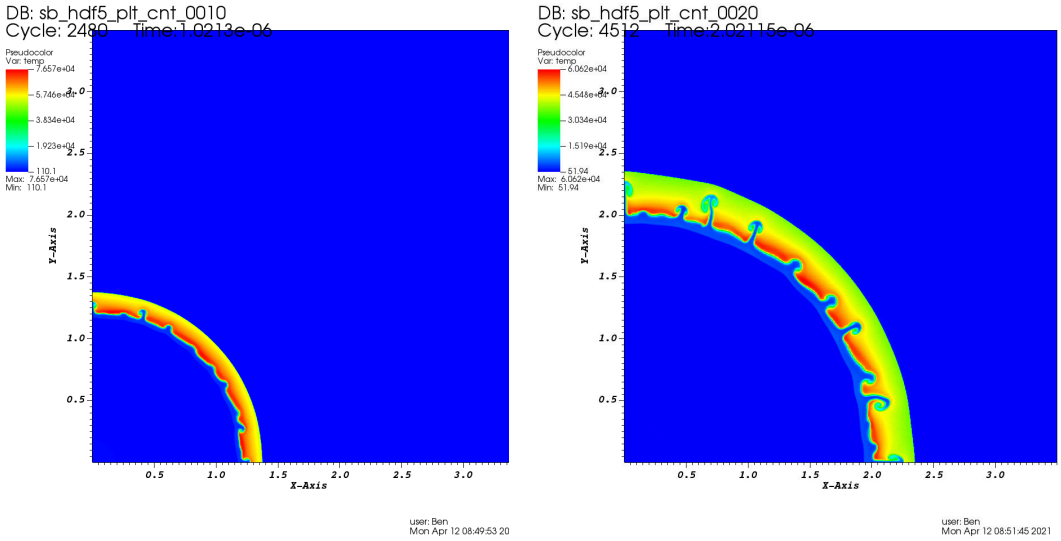

(a) (b)

Figure 4.19: Temperature at a few different times for a FLASH simulation with an improper density distribution. All temperatures are given in Kelvin. Times are shown in each image in seconds.

Material Influence

Next, the effect of the material was tested. Velocity and density were kept the same as was used for the base aluminum simulation. In reality these two parameters would be different for an impact on copper at the same velocity. Making this assumption allows for the affect of material, namely atomic mass in the case of these simulations, to be investigated. The results of this simulation can be seen in Figure 4.20.

Material does not appear to have much influence on the propagation speed of the plume. The main differences appear in the temperature and spikes of the instability. Copper has thicker and hotter spikes than than the aluminum while peak temperature is lower in copper than aluminum. It appears that more energy is going into the copper plume than into the aluminum plume, likely due to an increased collision rate in copper due to it being larger. These observations agree with the observations of the comparison made between the cubesat and solar panel plumes.

Background Pressure Influence

The final alteration performed was raise and lower the background pressure by an order of magnitude to understand how much changing the background pressure will alter experimental results. Figure 4.21 shows results from both the higher and lower background density.

The position of the plume in the higher density background simulation is less than that in the base case and the position is further in the lower density case, as expected. In comparison to the base simulation the peak temperature is lower in the high density case and higher in the low density case. This is the result of a difference in the shocks as this peak temperature is in the background gas behind the shock. As the plume can move much quicker in the low density case the shock is stronger and therefore results in a higher temperature. Bunching of the plume is also different

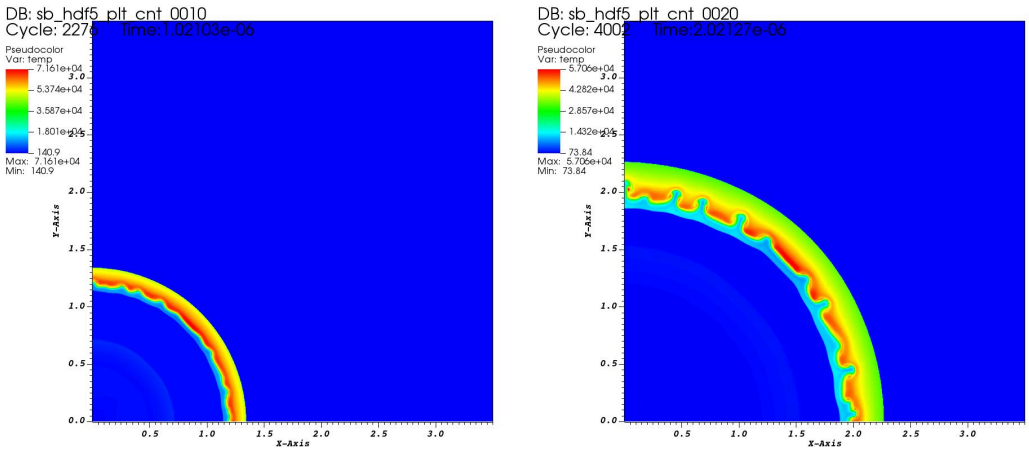

(a) (b)

Figure 4.20: Temperature at a few different times for a FLASH simulation with copper instead of aluminum. All temperatures are given in Kelvin. Times are shown in each image in seconds.

with the different background densities. In the high density background the contact surface is much thicker than in the low density background due to an increase in collisions.

To extend on these results, a similar result to the low density background is obtained when the plume density increases by an order of magnitude. Increased density can result in an oblique impact such as at the first AVGR experiments. An oblique impact results in all the plume traveling in one direction instead of in a ring around the impact point leading to a higher density plume even if the overall mass of vaporized material is the same. This higher plume density allows for the plume to expand further and therefore bunch up less. This is seen in the 2015 AVGR experiments where the plume thickness is much lower than observed during the 2019 tests and the contact surface is much smaller. This smaller contact surface means that less plume material is being heating and less additional ionization should occur. The thinner contact surface should also influence the optical measurements less, leading to a more accurate measurement of the plume temperature.

4.3.3 Impact Modeling

The simulations in the previous section showcased how important the initial plume properties are with respect to the interaction of the plume with the background gas and the subsequent evolution of the plume. The main shortcoming of these simulations was the inaccurate way material is released. A better simulation would model the impact and the propagation of the plume. This was attempted to be done using FLASH, although FLASH is not the best code for simulating an impact for a number of reasons that will be explained. That said, an approximation of the impact process will still give insights into how the gas dynamics evolve and are dependent on the impact parameters.

There is some precedent for using FLASH to model impacts. Liu [59] used FLASH to model the impact of planetary bodies. Other similar codes, such as Athena and Rage, have been adapted to be used for impact simulations.

The primary problem with using FLASH to simulate an impact is that FLASH is inherently a

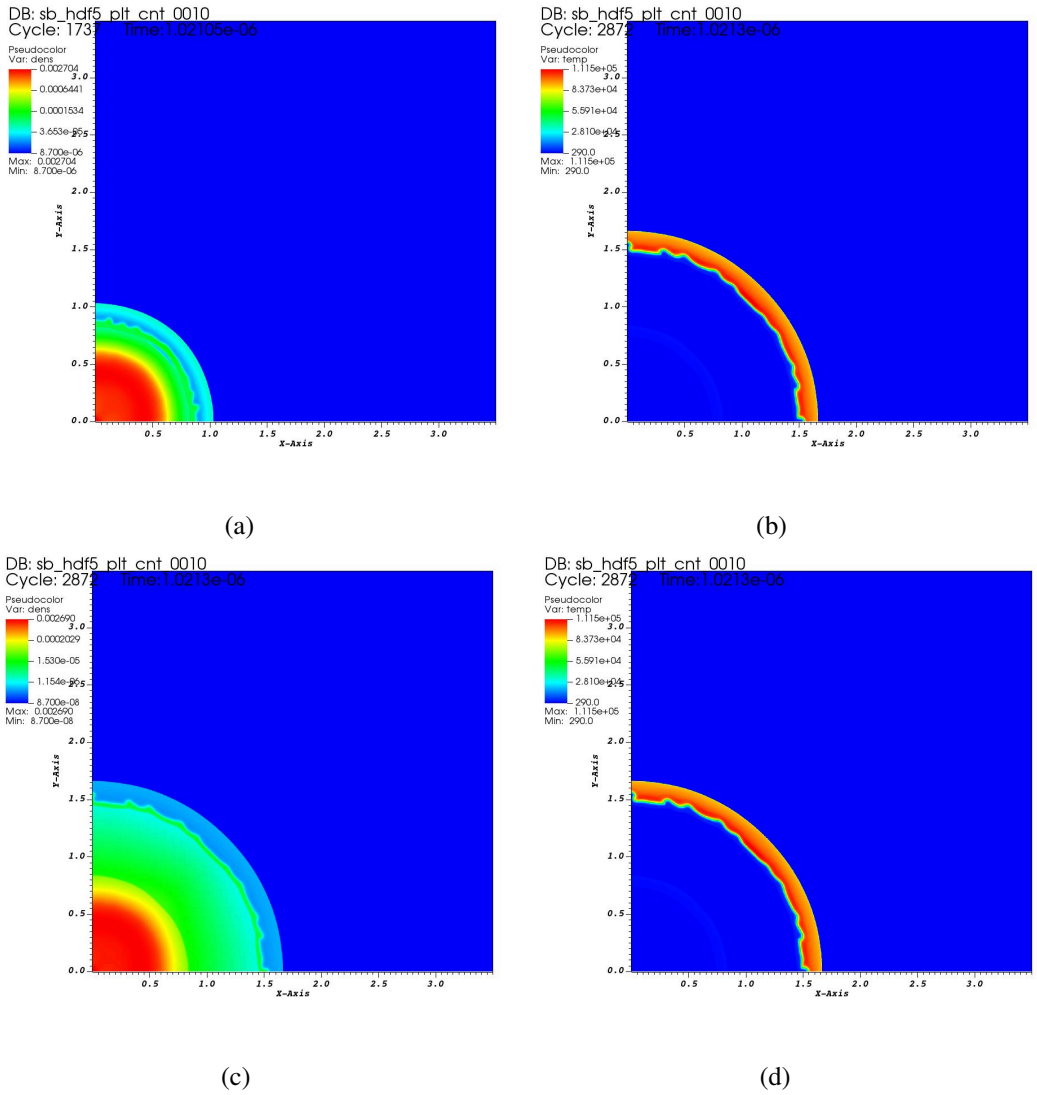

(a) (b)

(c) (d)

Figure 4.21: (a) density profile with a higher background density (b) temperature profile with a higher background density (c) density profile with a lower background density (d) temperature profile with a lower background density. Times are shown in each image in seconds.

fluid code. First of all, this means that if a material sees a pressure or density gradient the material will expand. As such, the projectile and target both tend to expand into the background gas as soon as the simulation is started. Secondly, no internal material forces such as strength or bond energy are available.

The expansion of the target can be contained by initially setting the top layer cells of the target as a solid boundary. This boundary is then changed back to a fluid concurrently with the point of intersection between the target and the projectile. Additionally, if any cell below or to the side of a solid boundary goes above the solid density value, 2.7 g/cm^3, then that cell will also be released as a fluid. This is to account for a shock propagating through the material. What this means is the initial bit of jetting will not be modeled. That said, as was mentioned previously, the initial jet is infinitely thin and has 0 mass, so it would not be captured anyways unless the grid resolution was infinitely small.

In contrast to the target there is no good way to contain the expansion of the projectile. Multiple methods were attempted, but all caused more issues with the simulation than they fixed. The primary idea attempted was to create a boundary around the projectile with logic checks to remove projectile material that entered that boundary and then replenish the material in the projectile. This was found to cause problems with the equation of state in and around the projectile. When it did run this logic did not have an appreciable influence on the result. Other methods such as increasing the background gas density or velocity around the projectile were also tried. These also appeared to have little effect. As such, the projectile was allowed to expand freely. This effect will decrease as the projectile velocity increases, as there is less time for ablation before the impact completes.

Another area where FLASH falls short for this application is in the equation of state. The code does have the ability to read in tabulated equation of state tables in the form of IONMIX tables. These can only be used in the three temperature implementation of FLASH, which introduces more complexity than is needed here due to the low ionization fraction in the AVGR like impacts. Using the tables would allow for better energy partitioning and tracking as the energy needed to ionize is taken into account, but this is again a low amount of energy in the cases of interest. Better energy tracking could be done with a full material model which includes energy for disassociation and vaporization, but that is not possible in FLASH. Additionally, using these tables would give a more accurate speed of sound in the solid density materials, leading to better shock propagation modeling. That said, the crater is not of interest in these simulations just the behavior of the plume. There will be an error in the jetting velocity due to incorrect sound speeds, but there will already be errors from the unwanted material movement from the projectile expanding.

It was intended to use the SESAME tables from Los Alamos, which can be converted to the IONMIX format, in these simulations to be as complete as possible but the request for access was never answered. Future work on this simulation can add this feature in and explore how the simulation changes. Without the SESAME tables the base equation of state implementation for FLASH was used. This consists of a two gamma equation of state where the gammas are set for each species in the simulation; there is functionality for the solver to evolve the gammas based on the temperature. These gammas are formulated as follows

$$\gamma_1 = \frac{\rho}{P}\frac{\delta P}{\delta \rho} \tag{4.15}$$

$$\gamma_2 = 1 + \frac{P}{\rho \varepsilon} \tag{4.16}$$

The first one relates the change in pressure to the change in density while the second one relates the pressure to the internal energy. 1.67 for both gammas was used for the aluminum in the simulations while 1.4 was used for diatomic nitrogen. This is a large approximation for the solid state aluminum part of the simulation. This will lead to, as stated above, the cratering and shock propagation being inaccurate. Once the material has vaporized then this γ value is a good approximation. As the main interest of this simulation is to observe the behavior of the plume, and not the cratering, this is an acceptable approximation. There will be some error in the initial conditions of the plume due to this approximation, but the general dynamics and properties are expected to be largely correct.

As with the previous simulations the parameters were initially set to simulate shots 7 and 10. The initial state of the simulation is shown in Figure 4.22. The projectile is started just touching the target and moves downwards at 5.4 km/s. Other than releasing the boundary on the top of the target the simulation is let to evolve freely.

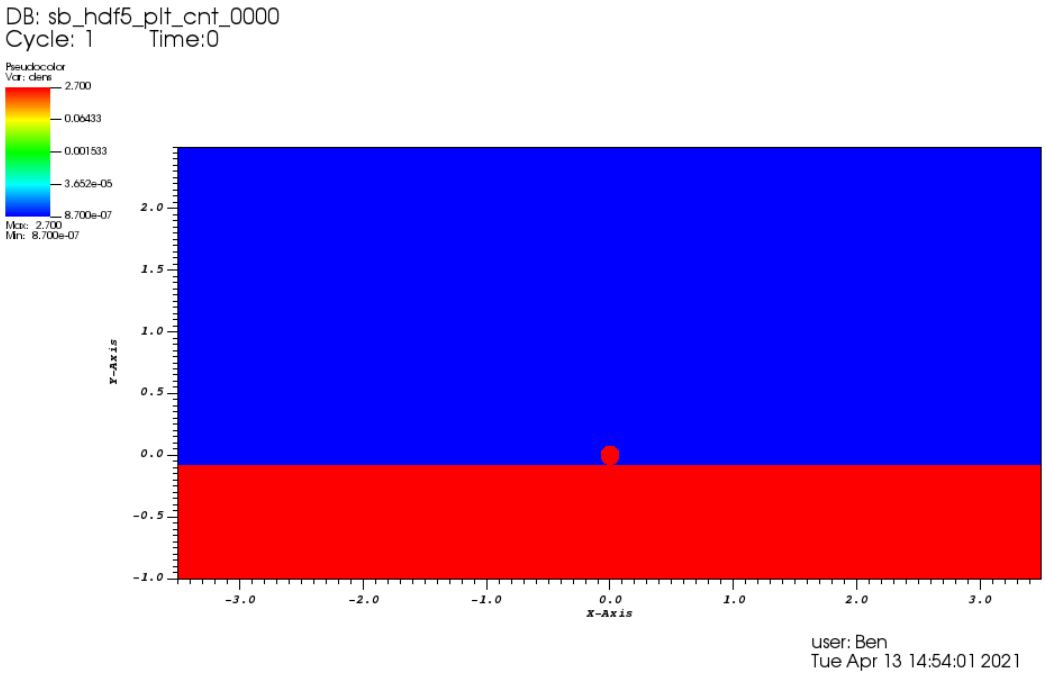

Figure 4.22: Starting density profile for the impact simulation.

Base Impact

Useful information can be gained from these simulations on the temperature of the plume, density distribution, and evolution. Snapshots of the base simulation results are shown in Figure 4.23. The timing of these snapshots allows for the presentation of a few key features. It should be noted that the max velocity of the jet is around 11 km/s, but velocity is not shown in any images. From the early images it can be seen that the expansion of the projectile does interfere slightly with the initial jetting. As previously mentioned, this is seemingly unavoidable. What seems to occur is some of the projectile material is pinched between the projectile and target leading to the material being

accelerated laterally. Additionally, the increased density around the projectile somewhat slows the initial jetting from the target, by what extent is difficult to determine.

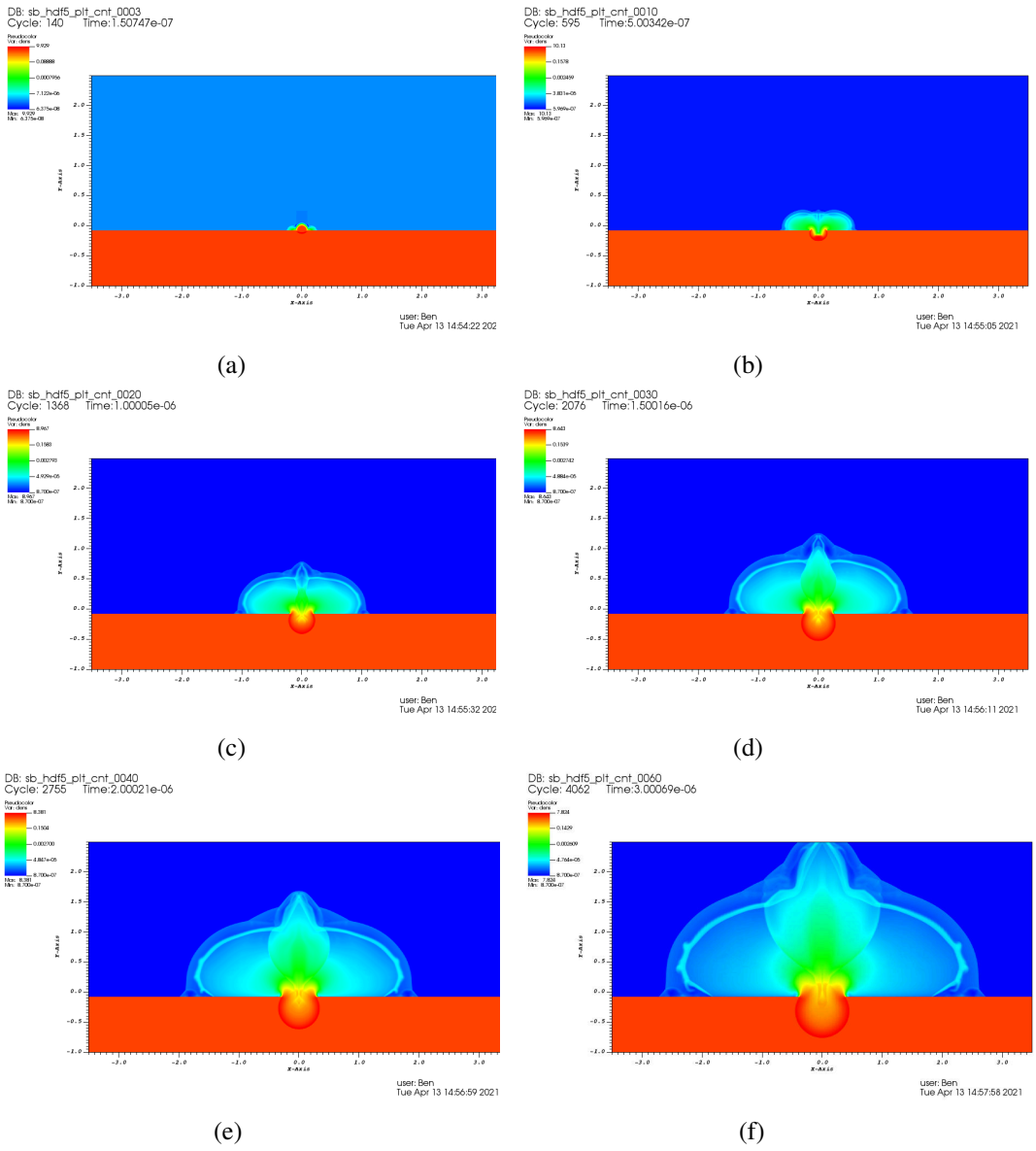

Figure 4.23: Density evolution of an impact with the base conditions.

Due to the downward movement of the projectile a low density region is left behind in its wake. The plume tries to expand into this region, but does so at a higher point due to the expansion of the projectile. Without the projectile expansion the density behind the projectile should be lower and therefore the expansion into this region more rapid.

The later stages of the impact behave much more as expected. The bulk of the plume moves horizontally forming a shock and contact surface with the background gas. At the later times the plume is at roughly the position observed in the experiments. If the expansion was not stopped and the simulation was allowed to continue, the entirety of the target material would expand outwards,

which is not realistic. This additional material will push forward the contact surface from behind leading to unrealistic values in position and velocity. Simulations with a solid boundary in the target with dimensions of the crater observed in the experiments were done to check how the limited amount of material changed the results. It was found that, for the length of simulation performed, the results were negligible. That is to say that the density and temperature of the plume was equivalent with the boundary in place. The additional boundary caused shock reflection into the plume, which also is not ideal. A proper equation of state would be slightly more correct as the shock propagation in the solid material would be more accurate leading to the proper amount of material becoming heated. That said, additional material would still expand into the plume given enough time. Given that the simulation hardly changed with a restricted crater size it is likely that a different equation of state would not lead to an appreciable change. It should also be noted that the density in these simulations approximates the density found from the first order contact surface analysis. Meaning the velocity, position, and density all seem to be fair approximations of observations, regardless of the improper equation of state.

One result that was unintended was the observation of the purely vertical part of the plume. This was observed in the high speed images between the dust jets, such as Figure 3.6, but the cause of it was unknown. From this simulation it is now clear that this part of the plume forms due to the coalescing of the plume in the impact crater as material is ablated from the walls. Dust jets may constrain the width of this vertical plume as it appears wider in these simulations than in the high-speed imagery. A code that captures the dust formation and the plume dynamics would be needed to confirm this.

As with the disk simulation, this simulation also shows a rise in temperature of the plume at the contact surface. Expanding on the results from the disk this temperature rise appears to be on all outer points of the plume, not just the front edge that is expanding horizontally. This strengthens the argument that this is what is causing the unexpected temperature measurement in the AVGR experiments.

Temperature at a few times in the simulation are shown in Figure 4.24. The region of hottest temperature is the mixing region between the plume and background gas, as was observed in the previous simulations. Additionally, it can be seen that the vertical plume structure also has an elevated temperature. This explains why it is visible in the high speed images. Temperature for both the plume front and shock heated background is lower in this simulation than in the 2D disk simulation. Likely this is due to the plume being able to expand vertically away from the target, something it could not do in the previous simulation.

In this simulation we see that not only does the plume bunch up and the front heat, but the top of the plume is heated as well. This explains why in early high-speed images from the AVGR tests the plume appeared to be a solid ellipsoid as seen in 4.14. Ejected dust would therefore not only move through a more dense plume, as explained from the results of the other simulations, but also an additional region of ionization on the top of the plume. Potentially this could cause the dust to transport more charge than it would in vacuum as it would collide with this additional area of ionization.

Cold Aluminum

Figure 4.25 shows simulation results an initial temperature of only 50.0K for the aluminum of the target and impactor. Lowering the initial temperature lowers the initial energy in the system. As bond energy and radiation energy losses are not accounted for in the base simulations, this gives

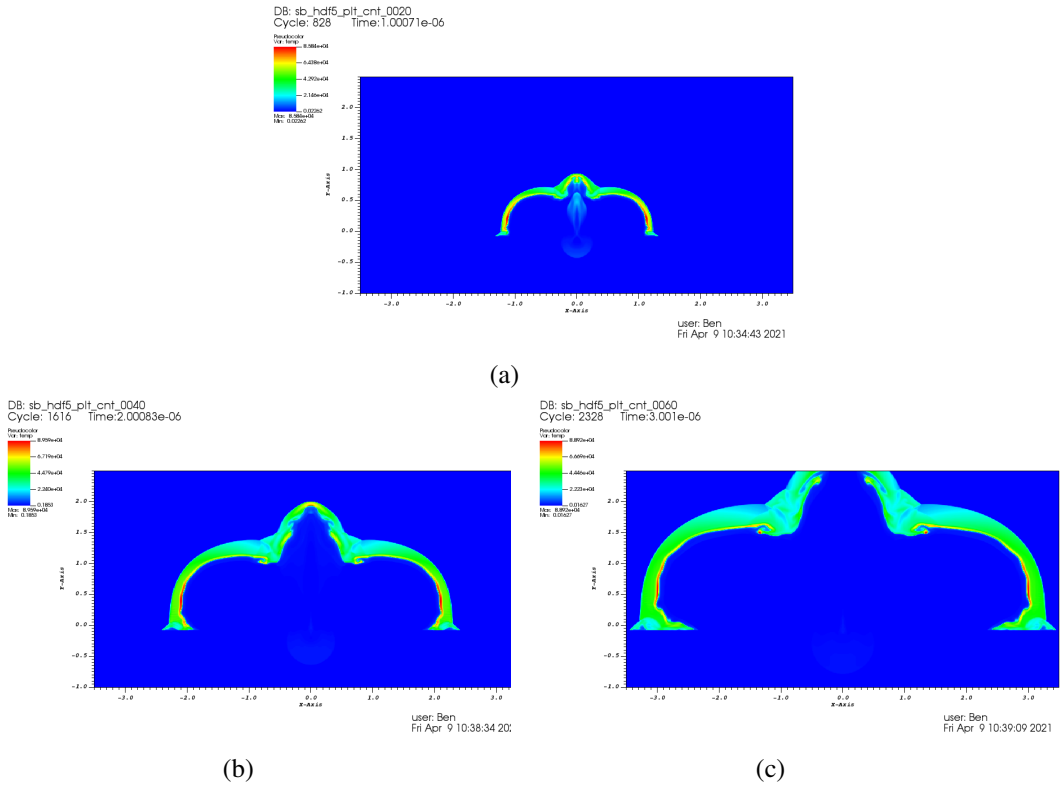

(a)

(b) (c)

Figure 4.24: Temperature evolution of the plume from an impact with base conditions.

some idea as to how a more accurate energy model would perform. Only the temperature data is presented here as the density data is similar to an order of magnitude. As can be see, the plume does not propagate as far or as fast as with the other temperature due to the lower amount of initial energy. Therefore, we can assume that the values of the base simulation are likely a slight over-approximation.

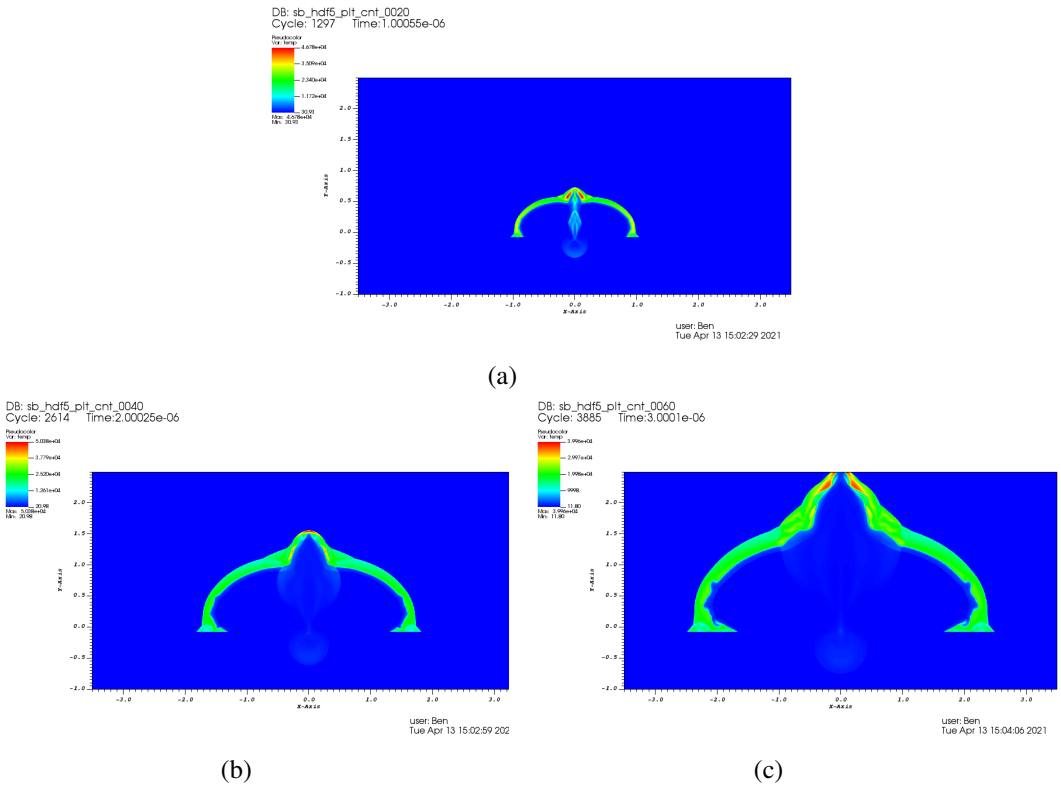

Figure 4.25: Temperature evolution of the plume from an impact with lower aluminum starting temperatures.

Solver Influence

One thing to note about FLASH, and these simulations in particular, is that there are a number of different solvers and solver options, such as slope limiters, to choose from. Choosing different solvers will change the simulation results as seen in Figure 4.26. These images are the same simulation parameters as has been presented, just using a different solver. Plume features, position, and temperature are all different from the previous simulation. Therefore, it should be emphasized that these simulations are intended to be representative of the impact and expansion, and not perfect descriptors.

An interesting feature from the results with the new solver is the clearer high temperature region at the front of the plume near the target surface. In the other simulations this region was present, but not as pronounced. The material in this region is from the onset of jetting. As can be seen in Figure 4.27 it is composed of both the target and the projectile. In reality it should just be the target, as the jetting starts from the target, but the projectile material is in there from the expansion of the

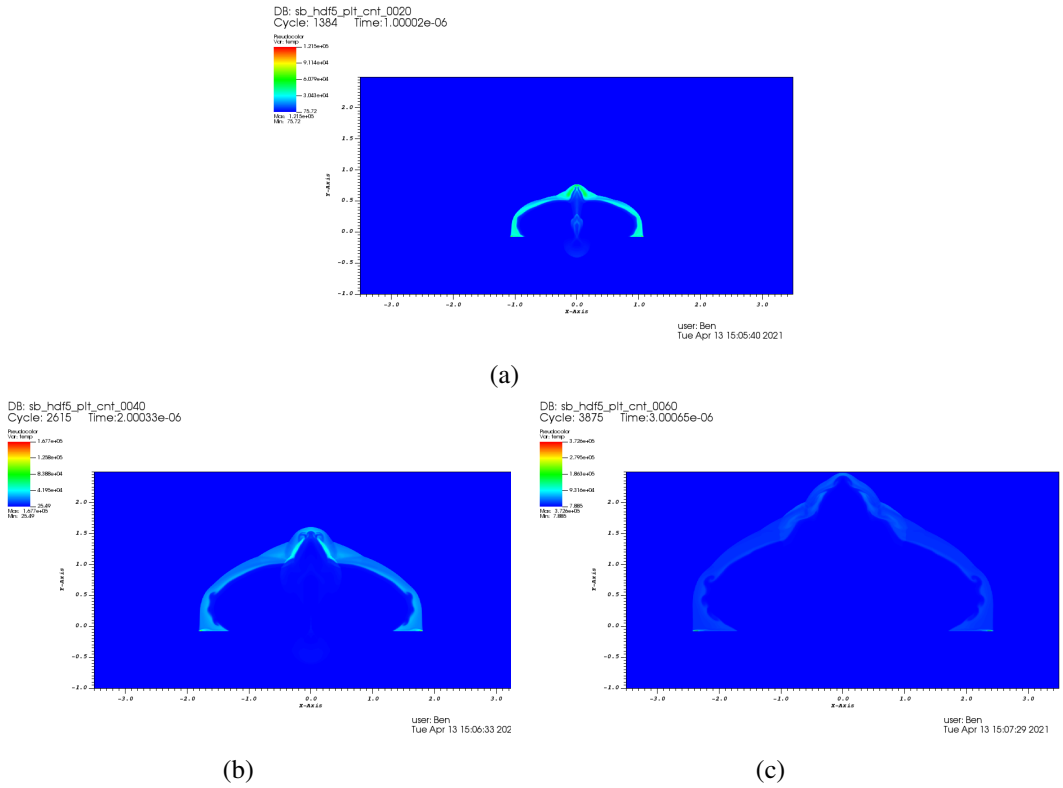

Figure 4.26: Temperature evolution of the plume using the base conditions but a different solver in FLASH.

projectile. The material in this plume travels at a horizontal velocity of around 10 km/s and does not seem to be slowed like the contact surface. This behaviour is what was observed from the outer expansion. Therefore, it is likely that this plume feature may evolve into the outer expansion part of the plume, especially when combined with the acceleration from the electron front, seen in the high speed images.

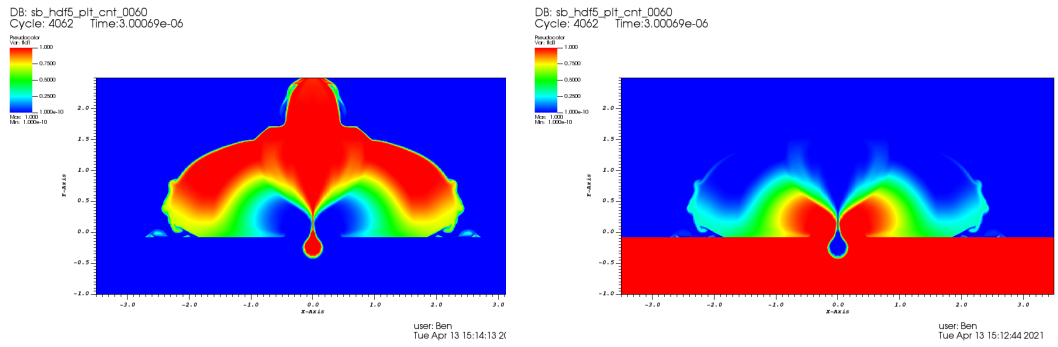

(a) (b)

Figure 4.27: (a) Fraction of impactor material (b) fraction of target material

Low Background Pressure

To determine the overall effect of the background gas on the plume geometry an impact simulation was performed with a background pressure of 5×10^{-6} Torr. This approximates the MPI background pressure. The density result of this simulation 0.5 μs after impact is presented in Figure 4.28. In order to have the plume geometry be accurate the initial temperature of the aluminum was set to 10 K. This reduced the expansion of the projectile which was significant with the lower pressure background and allowed the jetting angles to be more correct. As observed in the 50 K aluminum case above this does limit the energy in the system, slowing the plume, but the plume still expands significantly faster than in the 0.5 Torr background.

At 0.5 μs after impact the plume has already expanded to almost 1 cm from the impact site in the X direction, something that took over 1.0 μs in the base simulation. This horizontal expansion of the plume is still due to the jetting. The spikes on the sides of the plume are the extent of jetting while the two vertical lobes are from vapor expanding. Compare this to the base simulation where the vapor expanded mostly horizontally. It appears that this horizontal expansion was the result of the jetted material sweeping the background gas and creating a void for the expanding vapor to fill.

Plume Geometry with Dust

The potential for the condensed and heated plume from gas dynamics to influence the dust charge and trajectory has been described above. Additionally, as observed in the tungsten shot, the dust can also influence the plume geometry. In Figure 3.17 the inner plume can be observed to have a peak in the middle of its radial distribution. This peak is the result of dust that can be clearly viewed in the later stages of the expansion. FLASH simulations on an impact on tungsten showed the same general geometry as observed in the aluminum simulations, an expanding ellipsoid when viewed in 2D. The additional features observed in the high speed images are just a consequence

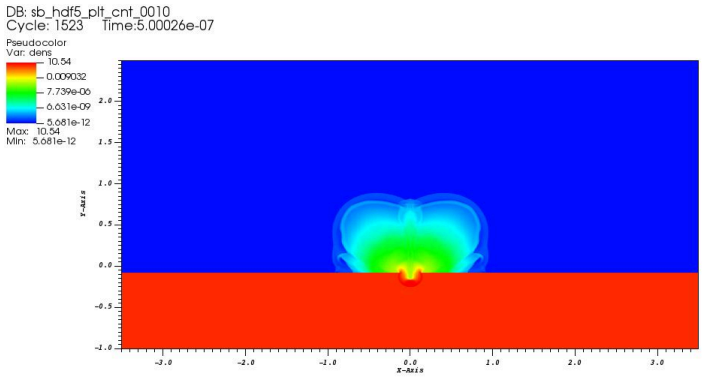

Figure 4.28: Plume density 0.5 μs after impact in a micro-Torr pressure background.

of the large dust particles that are visible. In this case the dust is clearly separating components of the plume which could lead to charge separation and RF radiation. Additionally, the plasma around this dust will oscillate at a different frequency than the plasma without dust due to altered density distributions and the electric potential that the dust accumulates. It is likely that the dust also altered the evolution of the RTI. Dust moves plume material away from the impact plane and concentrates it around the dust, lessening the amount of material at the contact surface. This could cause the RTI to occur sooner in the expansion process. Unfortunately this cannot be confirmed with FLASH due to the inability to model dust.

4.3.4 FLASH Modeling Summary

Hydrodynamic modeling of the hypervelocity impact plume dynamics observed during the AVGR experiments was performed using the FLASH code. Both a top view of the instability dynamics and a side view of the impact plume formation and propagation were obtained. These simulations used basic hydrodyamics without ionization and solid material properties. A simple fluid equation of state was utilized which is accurate for the portions of the simulations of interest.

From both simulation types the slowing of the plume due to interaction with the background was observed. In addition, the Rayleigh-Taylor instability very clearly occurred. The position of the plume approximated what was observed in experiment. This slowing lead to the density of the plume becoming increased at the plume front and consequently the temperature of the plume rising at the plume front due to collisions. The bunching and heating could lead to increased charge concentration in the plume as the impact produced charge bunches and more charge particles are produced due to additional ionization from the heated plume. These effects have a significant effect on the dust as the dust would propagate through more density and more charge than would occur in a vacuum. Additionally, this heating on the plume front explains the observed light from the plume.

4.4 Dust charging

Condensed phase impact debris will acquire a surface charge due to interactions with the plasma, potentially leading to dusty plasma effects. Light gas gun impacts, which generally occur at suborbital velocities, produce a significant quantity of condensed phase material. Such impacts have been

described as dusty for decades [15]. Experimental data show evidence of charged dust in the form of impulsive plasma signals, both positive and negative, and charge attachment may drive macroscopic charge separation and long range electric fields [12, 17, 23]. Moreover, a significant quantity of plasma is dragged along the dust trajectory, modifying the plume geometry. If charge attachment is sufficient, localized electron depletion occurs, fundamentally altering the plasma evolution and associated waves, oscillations, and emissions. The presence of a "slow" dust species may mitigate RF emissions compared with a purely electron-ion plasma, but charged macroscopic particles may pose a direct threat to electronics in their path.

Hydrodynamic simulations using a simple model for charge attachement to the condensed phase show qualitative agreement with experimental data [14], but no previous study has attempted to explicitly model the charging and evolution of condensed phase particles in an impact-generated plasma. Dust charging and transport, however, has seen increased attention in the context of Tokamaks, where material ablated from the reactor walls poses a serious operational hazard [75, 8, 92]. Impact plasmas typically have temperatures on the order of 0.5–2 eV, and span many orders of magnitude in density as they expand into the vacuum, decaying from an initial density that may exceed $10^{23}\,\mathrm{m}^{-3}$ depending on impact conditions [32, 58, 46, 102, 35]. Temperatures on the order of 10–20 eV and densities of 10^{19}–$10^{21}\,\mathrm{m}^{-3}$ typical of Tokamak edge plasma [8, 76, 91] are comparable to conditions in the expanding plasma. Flow velocities of up to a few km/s peak and dust velocities on the order of 1 km/s in Tokamak edge plasma [75, 80] are also similar to those in impact-generated plasmas; impact studies show plasma and ejecta velocities up to a few km/s [17, 23, 46]. Models of dust charging and transport in Tokamaks typically rely on orbital motion limited (OML) theory due to its analytic simplicity. The limitations of OML, however, necessitate modifications to account for large dust, flowing plasma, emissions, ablation, and other physical processes.

We make the first explicit estimates of dust charging in hypervelocity impacts using experimental observations of plasma conditions and the ejecta particle size distribution combined with a dust charging and dynamics model based on OML. The model includes modifications to extend dust charging theory to the post-impact environment. In particular, we focus on impacts on aluminum and regolith targets, which serve as analogues for spacecraft and small solar system bodies, respectively. We compare model predictions with data from light gas gun impact campaigns and predict that a sufficient proportion of electrons attach to dust shortly after impact that dusty plasma effects are likely.

4.4.1 Plasma expansion model

The impact and subsequent expansion are complex, three-dimensional phenomena and the plume velocity and geometry depend on the impactor and target materials, target bias, and impactor mass and velocity [86, 33, 23]. The expansion requires both hydrodynamic and kinetic theory to fully characterize due to coupling between the ejecta, plasma, and neutral components. Analytic models typically attempt to capture general properties of the expansion in space and time by assuming one-dimensional, spherically symmetric expansion. For example, Close et al. [12] used a time-dependent model for the electron density at the surface of the expanding plasma

$$n_\mathrm{e}(t) = \frac{n_{\mathrm{e}0}}{\left(1 + {}^{c_s t}/_{r_0}\right)^3}, \tag{4.17}$$

where $n_{\mathrm{e}0}$ is the initial electron density, r_0 is the initial radius, and $c_\mathrm{s} = \sqrt{{}^{\gamma k T_e}/_{m_i}}$ is the acoustic speed given specific heat ratio γ. Ju et al. [46] suggest an alternative, spatially-dependent model for

the density in the "fully-formed" plasma

$$n_{\mathrm{e}} = \left(\frac{r_0}{r}\right)^3 n_{\mathrm{e}0} \frac{1}{\left(1 + v_{\mathrm{exp}} t_{\mathrm{for}}\right)}, \tag{4.18}$$

where v_{exp} is the plasma expansion velocity and $t_{\mathrm{for}} = {}^{D_{\mathrm{p}}}/_{v_{\mathrm{p}}}$ is the formation time for a projectile with diameter D_{p} impacting at velocity v_{p}.

We instead propose using an analytic renormalization-group (RG) symmetry model for an expanding plasma bunch [52, 51] modified to account for an initial expansion speed. Derived from kinetic theory, such a model has the advantage of providing the velocity distribution function as a function of both space and time. We define the frequency variable $\Omega = v_{ti}/L_0$ assuming an initial scale length L_0 and initial ion thermal speed $v_{ti} = \sqrt{{}^{kT_{i0}}/_{m_i}}$. Integrating over the velocity distribution, the density and bulk velocity are

$$n_\alpha(r,t) = \frac{n_{\alpha 0}}{\left(1+\Omega^2 t^2\right)^{3/2}} \exp\left(-\frac{1}{2}\frac{\Omega^2}{1+\Omega^2 t^2}\left(\frac{r - v_0 t}{C_{\mathrm{s}}}\right)^2\right) \tag{4.19}$$

$$v_{\mathrm{exp}}(r,t) = \frac{\Omega^2 r t + v_0}{1+\Omega^2 t^2}, \tag{4.20}$$

where v_0 is the initial expansion velocity, $C_{\mathrm{s}} = \sqrt{\frac{kT_{\mathrm{i}0} + Z_{\mathrm{i}} kT_{\mathrm{e}0}}{m_{\mathrm{i}} + Z_{\mathrm{i}} m_{\mathrm{e}}}}$ is the initial ion acoustic speed for ions with charge $Z_{\mathrm{i}} e$, and $n_{\alpha 0}$ is the initial density of species α. To enforce quasineutrality, $n_{e0} = Z_i n_{i0}$.

Asymptotically, the density predicted by the RG model shows cubic decay in time, as expected in a 3D expansion; the RG model deviates from cubic decay in space because the velocity of the plasma front is non-constant, as Figure 4.29 shows. Note the RG model prediction that the plasma rapidly cools to $T \sim 0$ after a few microseconds is inconsistent with experimental observations. The temperature discrepancy may be due to interactions with neutrals or another mechanism. Assuming a constant temperature throughout the expansion is reasonable to order-of-magnitude.

Specifying the scale length L_0, initial velocity v_0, and quantity of charge produced Q_{imp} closes the system. The charge produced is approximately [64]

$$Q_{\mathrm{imp}} = 0.1 m_{\mathrm{p}} \left(10^{11}\, m_{\mathrm{p}}\right)^{0.02} \left(0.2\, v_{\mathrm{p}}\right)^{3.48}, \tag{4.21}$$

where Q_{imp} is the charge produced in C, and m_{p} and v_{p} are the projectile mass and velocity in g and km/s, respectively. We approximate the scale length using the crater radius, $L_0 = r_{\mathrm{c}}$. Cratering in impacts on solid aluminum agrees well with [26]

$$r_{\mathrm{c}} = k m_{\mathrm{p}}^{0.352} \rho_{\mathrm{t}}^{1/6} v_{\mathrm{p}}^{2/3}, \tag{4.22}$$

where the r_{c} is the crater radius in cm, m_{p} and v_{p} are again in g and km/s, ρ_{t} is the target density in g/cm^3, and k is a material constant ($k = 0.42$ for aluminum). For the powdered regolith simulant, we estimate the scale length using experimental observations and approximate m_{i} using the weighted average atomic mass of the constituent species. Given L_0 and Q_{imp}, the initial density at $r = 0$ to close (4.19) assuming hemispheric expansion is

$$n_{\mathrm{e}0} = \frac{Q_{\mathrm{imp}}}{\sqrt{2\pi^3} e} \left(\frac{\Omega}{C_{\mathrm{s}}}\right)^3. \tag{4.23}$$

To close (4.18) we simply compute $n_{\mathrm{e}0}$ by dividing total charge produced by crater volume.

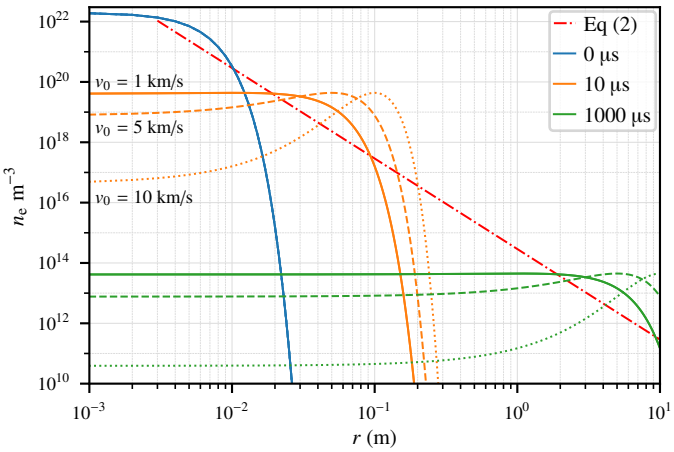

Figure 4.29: Density profile computed using the RG model (4.19) for select times and choices of v_0 compared with the profile obtained using (4.18) with $v_{exp} = 10\,\mathrm{km/s}$ [46]. Profiles assume a $5.25\,\mathrm{km/s}$ aluminum-on-aluminum impact with $m_p = 6\,\mathrm{mg}$. We use (4.21) and (4.22) to compute the charge produced and crater radius.

In Figure 4.30 we compare currents observed by the plasma sensors with the density predicted by (4.19) at those radial positions. Shots 2, 4, and 7 correspond to aluminum targets biased to 0 V, +300 V, and −300 V respectively, while shot 12 corresponds to the unbiased powdered regolith simulant. Results from the ejecta curtain correspond sensors 60° from the horizontal for aluminum impacts and vertically from the target for the regolith impact. Contrary to the spherical expansion assumption the expanding plasma is highly anisotropic. The bulk plasma jets in a plane nearly parallel to the target surface. Plasma readings in the ejecta curtain are due to condensed phase material pushing through the plume and dragging a portion of the plasma [23].

We find $v_0 \approx 10\,\mathrm{km/s}$ and $T_{e0} = T_{i0} \approx 1\,\mathrm{eV}$ result in a time to peak density and peak width that agrees well with observations from the aluminum-on-aluminum impacts. Using $v_0 \approx 1\,\mathrm{km/s}$ and $T_{e0} = T_{i0} \approx 0.33\,\mathrm{eV}$ results in reasonable time to peak and density values in the ejecta curtain, and the slower decay time is consistent with observations. A possible explanation is that condensed phase debris are ejected slightly after the bulk plasma and pass through plasma that has had time to cool slightly. At both sensor locations, the powdered regolith impact shows a delayed time-to-peak, likely because impact, cratering, and ejection occurs over a much longer time in the granular medium.

We also apply a simple peak detection algorithm based on the wavelet transform to search for possible dust impacts; dots on the timeline in Figure 4.30 indicate such peaks. We previously found evidence of impulses, which may indicate dust, in plasma sensor data from the ejecta curtain, and these measurements show up as thin bands when the passing the data through a wavelet transform [23, 78]. We detect such impulses by first computing the wavelet transform using Morlet wavelets [88] and rectifying the power spectrum to eliminate bias towards low frequencies [60]. We then integrate the power spectrum in frequency space and use a peak detection algorithm to identify impulses, which appear as narrow, prominent peaks in the integrated power. This method effectively separates impulses from slower variation.

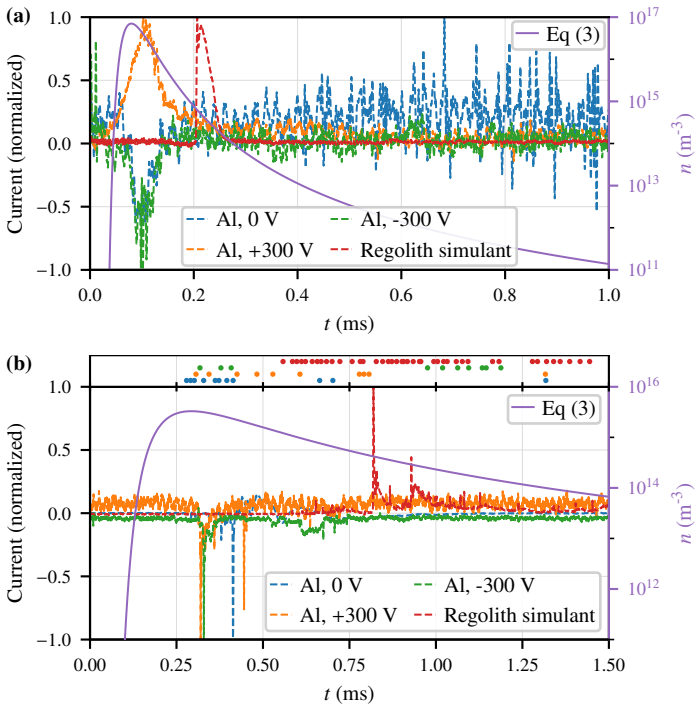

Figure 4.30: Currents measured by the plasma sensors and density at the sensor predicted by (4.19). Currents are normalized by the peak value recorded by the sensor for each shot. The modeled density profiles correspond to a 5.25 km/s aluminum-on-aluminum impact with $m_p = 6\,\text{mg}$ using (4.21) and (4.22) to compute the charge produced and crater radius. Impact parameters for the regolith simulant yield a qualitatively qualitatively similar density profile. **(a)** Readings at the sensor positioned 10° from the horizontal along with (4.19) assuming $v_0 = 10\,\text{km/s}$ and $T_{e0} = T_{i0} = 1\,\text{eV}$. **(b)** Readings from the ejecta curtain along with (4.19) assuming $v_0 = 1\,\text{km/s}$ and $T_{e0} = T_{i0} = 0.33\,\text{eV}$. Dots correspond to impulses in the signal, which may indicate secondary impacts by charged dust.

4.4.2 Dust charging and dynamics model

Orbital motion (OM) theory gives the exact solution for the equilibrium currents and potential distribution around particle immersed in a stationary, Maxwellian plasma [55, 49], including when electron emission is significant [18]. In practice, however, dust models seldom use the full OM theory because it is computationally complex and breaks down in drifting systems due to loss of spherical symmetry. Instead, dust charging models typically use the orbital motion limited (OML) theory developed by Mott-Smith and Langmuir [69]. OML solves for the surface potential and plasma currents to a charged particle immersed in a stationary plasma in the absence of potential barriers assuming particles approach from infinity and conserve angular momentum and kinetic energy. The resulting charging collision cross-section is easily integrated for Maxwellian species to obtain analytic expressions for the currents and solve for the floating potential [3, 49].

OML is only strictly valid when particles are vanishingly small compared to the screening length and there are no potential barriers [4]. In practice, however, OML produces reasonable estimates of the surface potential and plasma currents for particles up to a few Debye lengths in size when $T_\mathrm{i} \sim T_\mathrm{e}$ [49, 21]. Moreover, with appropriate modifications, OML-like models reasonably approximate the surface potential of large dust and particles immersed in a drifting Maxwellian plasma [96, 97]. Integration over the momentum and kinetic energy of incoming particles leads to expressions for the OML contributions to the drag force and energy balance [79].

Describing the evolution of dust particles requires accounting for additional terms beyond OML [61, 75, 80, 8]. Electron reflection and thermionic and secondary electron emission may play a significant role in determining the dust charge and surface potential in high energy density systems, leading to positive surface charge under certain conditions. We neglect secondary emission and electron reflection effects, as the contribution is small for $T_\mathrm{e} \lesssim 1$ eV [8, 90], but thermionic emission may play an important role in impact plasma conditions. The force balance includes drag due to ions scattered by coulomb collisions, momentum transfer from direct collisions, and terms due to external fields [79]. Finally, energy balance at the dust surface includes the OML contribution, energy lost to emitted particles, and surface processes, such as thermal radiation, neutralization and recombination at the surface, and ablation [61]. These terms are illustrated in Figure 4.31.

Accounting for all of these terms leads to a set of coupled ODEs for the dust charge Q_d, velocity v_d, specific enthalpy h_d, and mass m_d as functions of time

$$\dot{Q}_\mathrm{d} = \sum_\alpha I_{\mathrm{c},\alpha} - I_\mathrm{th} \tag{4.24}$$

$$m_\mathrm{d}\dot{v}_\mathrm{d} = \sum_\alpha F_{\mathrm{c},\alpha} + F_\mathrm{sc,i} + F_\mathrm{ext} \tag{4.25}$$

$$m_\mathrm{d}\dot{h}_\mathrm{d} = \sum_\alpha P_{\mathrm{c},\alpha} + P_\mathrm{th} + P_\mathrm{surf} + P_\mathrm{abl} \tag{4.26}$$

$$\dot{m}_\mathrm{d} = \Gamma_\mathrm{acc} - \Gamma_\mathrm{abl}. \tag{4.27}$$

Γ, I, F and P correspond to the mass, charge, momentum, and energy fluxes, respectively. Subscript "c,α" indicates the contribution due to OML collection by species α, including neutrals, and subscript "th" corresponds to the thermionic electron current. $F_\mathrm{sc,i}$ is the drag due to Coulomb scattering of ions, F_ext is the sum of body forces due to interactions with external fields, P_surf and P_abl account for contributions to the energy balance by surface processes and ablation, and Γ_acc and Γ_abl correspond to mass fluxes due to like particle collection and ablation. Enthalpy is related to

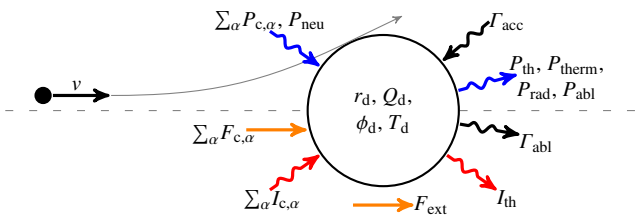

Figure 4.31: Schematic of a dust particle experiencing a grazing OML collision with an incoming particle with velocity v, annotated with the charge (red), momentum (orange), energy (blue), and mass (black) fluxes included in the model.

the temperature T_d by $h_d = \int_0^{T_d} m_d c_p(T) dT$, where c_p is the heat capacity. Dust mass and radius are related by $m_d = \frac{4}{3}\pi\rho_t r_d^3$ when ejecta are of the target material.

Dust charging occurs much faster than other processes of interest, and terms in the current, force, energy, and mass balance depend on the surface potential ϕ_d, not the charge Q_d. In practice, we solve for the equilibrium potential holding all other terms constant instead of integrating (4.24) and evolve the remaining terms using standard ODE integration techniques. Many of the terms depend on the dust material and closing the system requires a material model; the properties of aluminum are well characterized, but this is non-trivial for complex materials, such as regolith. We approximate the regolith simulant using a material model for silica (SiO_2), which has comparable average atomic mass and qualitatively similar properties, and assume a single ion species with the average atomic mass of 20 proton masses. The following subsections describe the solution of the surface potential, calculation of the force and energy balance, and relation between the surface potential and dust charge.

Current balance and the surface potential

Assuming plasma particles approach a small spherical grain with radius r_d and surface potential ϕ_d from infinite distance leads to the well-known OML currents [3, 49]. We normalize the currents $j = |I|/\sqrt{8\pi} r_d^2 e n_{e\infty} v_{te}$, where $n_{e\infty} = Z_i n_{i\infty}$ is the electron density in the bulk plasma assuming a single ion species and $v_{t\alpha} = \sqrt{kT_\alpha/m_\alpha}$ is the thermal speed of species α. In a stationary plasma the normalized currents are

$$j_{c,e}^{OML}(\varphi_d) = \begin{cases} \exp(\varphi_d), & \varphi_d < 0 \\ 1 + \varphi_d, & \varphi_d > 0 \end{cases} \tag{4.28}$$

$$j_{c,i}^{OML}(\varphi_d) = \begin{cases} \sqrt{\beta_i \mu_i^{-1}}\left(1 - Z_i \beta_i^{-1} \varphi_d\right), & \varphi_d < 0 \\ \sqrt{\beta_i \mu_i^{-1}} \exp\left(-Z_i \beta_i^{-1} \varphi_d\right), & \varphi_d > 0 \end{cases}, \tag{4.29}$$

where $Z_i e$ is the ion charge, $\beta_\alpha = T_\alpha/T_e$, $\mu_\alpha = m_\alpha/m_e$, and $\varphi = e\phi/kT_e$.

Non-zero drift velocity violates spherical symmetry assumption inherent to OML and wake formation leads to an anisotropic potential distribution [40, 41, 98, 97]. The OML charging cross-section, however, remains integrable for a drifting Maxwellian plasma, yielding shifted OML (SOML) expressions for the ion currents. When the flow speed is small compared to the electron thermal speed, (4.28) is a good approximation of the electron current and the normalized ion current is

[79, 80]

$$j_{\mathrm{c,i}}^{\mathrm{SOML}}(\varphi_{\mathrm{d}}) = \begin{cases} \frac{1}{2}\sqrt{\beta_{\mathrm{i}}\mu_{\mathrm{i}}^{-1}}\left(\sqrt{\frac{\pi}{2}}\left(u^{-1}+u_{\mathrm{i}}\right)\mathrm{erf}\left(u_{\mathrm{i}}/\sqrt{2}\right)+\exp\left(-u_{\mathrm{i}}^2/2\right)-\right. & \\ \left.\sqrt{2\pi}u_{\mathrm{i}}^{-1}Z_{\mathrm{i}}\beta_{\mathrm{i}}^{-1}\varphi_{\mathrm{d}}\,\mathrm{erf}\left(u_{\mathrm{i}}/\sqrt{2}\right)\right), & \varphi_{\mathrm{d}}<0 \\ \sqrt{\frac{\pi}{32}}\sqrt{\beta_{\mathrm{i}}\mu_{\mathrm{i}}^{-1}}u_{\mathrm{i}}^{-1}\left(\left(1+u_{\mathrm{i}}^2-2Z_{\mathrm{i}}\beta_{\mathrm{i}}^{-1}\varphi_{\mathrm{d}}\right)\left(\mathrm{erf}\left(u_{\mathrm{i}+}\right)+\mathrm{erf}\left(u_{\mathrm{i}-}\right)\right)+\right. & \\ \left.\frac{2}{\sqrt{\pi}}\left(u_{\mathrm{i}+}\exp\left(-u_{\mathrm{i}-}^2\right)+u_{\mathrm{i}-}\exp\left(-u_{\mathrm{i}+}^2\right)\right)\right), & \varphi_{\mathrm{d}}>0 \end{cases} \tag{4.30}$$

where $u_\alpha = |v_{\mathrm{d}} - v_\alpha|/v_{\mathrm{t}\alpha}$ is the relative flow speed normalized by the thermal speed, and $u_{\mathrm{i}\pm} = u_{\mathrm{i}}/\sqrt{2} \pm \sqrt{Z_{\mathrm{i}}\beta_{\mathrm{i}}^{-1}\varphi_{\mathrm{d}}}$. Taking the limit $u_{\mathrm{i}} \to 0$ recovers the standard OML ion current from the SOML expression.

OML and SOML yield a reasonable surface potential for particles up to a few Debye lengths in radius when β_{i} is of order unity ($T_{\mathrm{i}} \sim T_{\mathrm{e}}$) [49, 41]. Shortly after impact, however, the Debye length is on the order of nanometers, orders of magnitude smaller than the ejecta of interest. In the thin sheath limit, the sheath geometry is approximately planar, but the thick pre-sheath must be treated in a spherical coordinate system [96, 97]. Using the sounds speed as the Bohm condition, ions enter the sheath with speed $v_{\mathrm{se}} = \sqrt{\mu_{\mathrm{i}}^{-1}v_{\mathrm{te}}^2 + Z_{\mathrm{i}}\gamma v_{\mathrm{ti}}^2}$, and the normalized potential drop across the sheath in the absence of electron emission is [83]

$$\Delta\varphi = \frac{1}{2}\ln\left(2\pi\mu_{\mathrm{i}}^{-1}\left(1+Z_{\mathrm{i}}\gamma\beta_{\mathrm{i}}\right)\right). \tag{4.31}$$

The adiabatic specific heat ratio $\gamma = 5/3$ empirically yields the best estimate of the floating potential [97]. Assuming ions entering the sheath reach the dust surface, we compute the ion current using the OML expression at the sheath edge; in the thin-sheath limit $j_{\mathrm{c,i}}^{\mathrm{TS}}(\varphi_{\mathrm{d}}) = j_{\mathrm{c,i}}^{\mathrm{OML}}(\varphi_{\mathrm{d}} - \Delta\varphi)$. Substituting $\varphi_{\mathrm{d}} - \Delta\varphi$ into (4.29) and (4.30) and solving for the equilibrium potential results in the modified OML (MOML) and shifted, modified OML (SMOML) potentials, respectively.

Secondary electron emission, photoemission, and thermionic emission all play a role in dust charging under certain conditions [79]. In hypervelocity impact plasma conditions, however, thermionic emission is the dominant emission mechanism. OML currents decrease and the relative contribution of the thermionic current becomes significant as the plasma density drops off away from the impact site.

The thermionic current for negatively charged dust is given by the Richardson-Dushmann equation [81]

$$I_{\mathrm{th},0} = \lambda_{\mathrm{R}}\frac{16\pi^2 r_{\mathrm{d}}^2 e m_{\mathrm{e}} k^2 T_{\mathrm{d}}^2}{h^3}\exp\left(-\frac{W}{kT_{\mathrm{d}}}\right), \tag{4.32}$$

where h is the Planck constant, λ_{R} is a material-dependent factor, and W is the material work function. We use $W = 4.08\,\mathrm{eV}$ for aluminum and $W = 4.16\,\mathrm{eV}$ for silica. Normalizing as before, we define $\hat{j}_{\mathrm{th}} = I_{\mathrm{th},0}/\left(\sqrt{8\pi}r_{\mathrm{d}}^2 e n_{\mathrm{e},\infty} v_{\mathrm{te}}\right)$. When the dust charge is negative $j_{\mathrm{th}} = \hat{j}_{\mathrm{th}}$.

A potential well forms near the dust surface and the charge becomes positive when the thermionic current is large [19]. For finite-size dust, the potential well formation and positive charging occurs at a negative surface potential φ_{d}^*, beyond which reabsorption of emitted electrons due to the potential well reduces the net thermionic current [20]; failure to account for the formation of the potential

well results in a significant overestimate of the heat flux and underestimate of dust lifetimes [90]. Defining $\tau = T_\mathrm{d}/T_\mathrm{e}$ and j_th^* as the critical thermionic current for which $Q_\mathrm{d} = 0$, the normalized thermionic current is

$$j_\mathrm{th} = \hat{j}_\mathrm{th}\left(1 + \frac{\varphi_\mathrm{d} - \varphi_\mathrm{d}^*}{\tau}\right)\exp\left(-\frac{\varphi_\mathrm{d} - \varphi_\mathrm{d}^*}{\tau}\right) \tag{4.33}$$

when $\hat{j}_\mathrm{th} > j_\mathrm{th}^*$ [81, 20].

We must address the effect of emission on the sheath potential drop in the thin-sheath limit. Defining the ratio of emitted to OML electrons $\delta = j_\mathrm{th}/j_\mathrm{c,e}$, the sheath drop is approximately $\Delta\varphi = \Delta\varphi|_{j_\mathrm{th}=0} - \ln(1-\delta)$ for moderate values of δ [83]. The relation is singular, however, for $\delta \to 1$. Alternatively, one can use analytic expressions for a planar source-collector-sheath system to estimate the sheath drop even after a potential well forms [7]. Computing $\Delta\varphi$ in this manner enables reasonable estimates of the floating potential for strongly emitting particles, but underestimates the sheath drop and floating potential compared with (4.31) in the absence of emission. When a potential well exists $\Delta\varphi \approx 0$ [7]. We therefore propose a simplified model for the sheath drop in which we apply a linear correction to (4.31) in the presence of emission

$$\Delta\varphi = \begin{cases} \Delta\varphi = \frac{1-\delta/\delta^*}{2}\ln\left(2\pi\mu_\mathrm{i}^{-1}\left(1+\gamma\beta_\mathrm{i}\right)\right) - \left(\ln(1-\delta) - \frac{\delta}{\delta^*}\ln(1-\delta^*)\right), & \delta < \delta^* \\ 0, & \delta \geq \delta^* \end{cases}. \tag{4.34}$$

This expression converges to the appropriate value of $\Delta\varphi$ in the absence of electron emission, reasonably approximates the sheath drop for large, emitting grains, and alleviates the need to explicitly solve for the planar sheath drop.

The floating potential is the solution to the equilibrium current balance $j_\mathrm{c,i} = j_\mathrm{c,e} - j_\mathrm{th}$. The equilibrium condition for negatively charged dust takes the form $(c_0 - c_1\varphi_\mathrm{d})\exp(-\varphi_\mathrm{d}) = c_2$ in the OML limit. This has the explicit solution $\varphi_\mathrm{d} = -W\left(\frac{c_2}{c_1}\exp\left(\frac{c_0}{c_1}\right)\right) + \frac{c_0}{c_1}$, where $W(x)$ is the principal branch of the Lambert-W function. The thin-sheath potential also follows this form if $\Delta\varphi$ is specified explicitly.

The potential drop across the sheath in the presence of electron emission depends on the equilibrium potential implicitly via the ratio of collected to emitted electrons $\delta = j_\mathrm{th}\exp(-\varphi_\mathrm{d})$. We therefore must simultaneously solve for the δ and φ_d that yield a self-consistent equilibrium solution for negatively charged dust in the thin-sheath limit. φ_d has an explicit solution once δ is specified. We recast the problem as the solution to $\delta - j_\mathrm{th}\exp(-\varphi_\mathrm{d}(\delta)) = 0$, solve for δ using standard numerical root-finding methods, and analytically compute the corresponding φ_d.

We interpolate between the OML and thin-sheath solutions in the transition regime using [96]

$$\varphi_\mathrm{d}(\rho) = \begin{cases} \varphi_\mathrm{d}^\mathrm{OML}, & \rho \leq \rho_\mathrm{OML} \\ \varphi_\mathrm{d}^\mathrm{TS}, & \rho \geq \rho_\mathrm{TS} \\ \frac{\varphi_\mathrm{d}^\mathrm{TS} - \varphi_\mathrm{d}^\mathrm{OML}}{\ln(\rho_\mathrm{TS}) - \ln(\rho_\mathrm{OML})}\ln\left(\frac{\rho}{\rho_\mathrm{TS}}\right) + \varphi_\mathrm{d}^\mathrm{TS}, & \rho_\mathrm{OML} < \rho < \rho_\mathrm{TS} \end{cases}, \tag{4.35}$$

where $\rho = r_\mathrm{d}/\lambda_\mathrm{De}$ is the dust radius normalized by the Debye length $\lambda_\mathrm{De} = \sqrt{\varepsilon_0 k T_\mathrm{e}/(n_\mathrm{e} e^2)}$, and $\varphi_\mathrm{d}^\mathrm{OML}$ and $\varphi_\mathrm{d}^\mathrm{TS}$ are the solutions to the equilibrium potential in the OML and thin-sheath limits, respectively. Using $\rho_\mathrm{OML} = 1.25\beta_\mathrm{i}^{0.4} + 0.37u_\mathrm{i}^{2.1}$ and $\rho_\mathrm{TS} = 50$ as limits for applying the OML and thin-sheath solutions, respectively, leads to predictions of the floating potential in good agreement with simulation over a wide range of conditions when $\beta_\mathrm{i} < 2$ [98].

Finally, j_{th} depends non-linearly on $\exp(-\varphi_{\text{d}})$ when the surface charge is positive, precluding an analytic solution. The exact form of the equilibrium condition depends whether $\varphi_{\text{d}}^* < \varphi_{\text{d}} < 0$ or $\varphi_{\text{d}} > 0$. Both cases, however, yield expressions easily solved numerically using Newton's method. The OML and thin-sheath potentials are identical in this regime because $\Delta\varphi \approx 0$ for positively charged dust.

Equilibrium solutions for negatively charged emitting grains in the thin-sheath limit and for positively charged grains in general require knowledge of the critical emission current j_{th}^* and corresponding potential φ_{d}^*. Assuming spherical symmetry, the potential distribution around a dust particle is the solution to the Poisson equation

$$\nabla^2\varphi(z) = \rho^2 \frac{n_{\text{e}} + n_{\text{th}} - n_{\text{i}}}{n_{\text{e},\infty}}, \tag{4.36}$$

where $z = r/r_{\text{d}}$, n_{e} and n_{i} are the plasma electron and ion densities, and n_{th} is the emitted electron density. The ratios $n_{\text{e}}(z,\varphi)/n_{\text{e},\infty}$, $n_{\text{i}}(z,\varphi)/n_{\text{e},\infty}$, and $n_{\text{th}}(z,\varphi)/n_{\text{e},\infty}$ have analytic forms under the OML assumptions as long as the potential is monotonic ($j_{\text{th}} \leq j_{\text{th}}^*$) [5, 21, 20].

The OML potential distribution is the solution to the two-point boundary value problem for the Poisson equation. At the grain surface, we enforce $\varphi(z=1) = \varphi_{\text{d}}^{\text{OML}}$. For $R >> 1, \rho^{-1}$, reasonable choices for the boundary condition are $\nabla\varphi(z=R) = 0$ or $\nabla\varphi(z=R) = -2\varphi(R)/R$ [20, 21]. We use the latter condition corresponding to a $1/r^2$ potential far from the dust. We solve for the value of j_{th}^* and corresponding φ_{d}^* by enforcing the additional constraint of $\nabla\varphi(r_d) = 0$ corresponding to the onset of a potential well [20, 90]. The value of j_{th}^* depends non-trivially on the dimensionless parameters μ_{i}, β_{i}, ρ, u_{i}, and τ, and solving a boundary value problem at every point in the time evolution of a dust grain is computationally impractical. Holding the mass and temperature ratios μ_{i} and β_{i} constant, we pre-compute a lookup table of critical emission current as a function of ρ, u_{i}, and τ, and use cubic spline interpolation between the precomputed points. This allows us to accurately estimate the values of j_{th}^* and φ_{d}^* over the parameter range of interest at minimal cost.

Surface charge

Predicting the initial degree of charge attachment shortly after impact and charge deposition by dust grains impacting the plasma sensors requires knowledge of both the surface potential and charge state of dust particles. Assuming a conducting spherical grain and spherically symmetric potential, Gauss's law yields the surface charge

$$Q_{\text{d}} = 4\pi\varepsilon_0 r_{\text{d}}^2 \left.\frac{d\phi}{dr}\right|_{r=r_{\text{d}}}. \tag{4.37}$$

We define the normalized charge $\mathscr{Q}_{\text{d}} = Q_{\text{d}}/\left(4\pi e n_{\text{e}\infty}\lambda_{\text{De}}^3\rho\right) = -\left.\frac{d\varphi}{dz}\right|_{z=1}$. This normalization has the convenient property that the normalized charge in the limit of infinite Debye length ($\rho \to 0$) is simply $\mathscr{Q}_{\text{d}} = \varphi_{\text{d}}$, and $\mathscr{Q}_{\text{d}}/\varphi_{\text{d}}$ is a metric of non-linearity in the dependence of surface charge on dust size.

The Debye-Hückel potential, obtained by solving the linearized Poisson equation, reasonably approximates the potential distribution around probes or particles of small but non-neglible size compared to the Debye length. Taking the derivative at the dust surface results in the Whipple approximation [95]

$$\mathscr{Q}_{\text{d}} = \left(1 + \rho\frac{\lambda_{\text{De}}}{\lambda_{\text{s}}}\right)\varphi_{\text{d}}. \tag{4.38}$$

Using the linearized Debye length $\lambda_l^{-2} = \lambda_{De}^{-2} + \lambda_{Di}^{-2}$ for the screening length λ_s results normalized charge $\left(1+\rho\sqrt{1+\beta_i^{-1}}\right)\varphi_d$. The Whipple approximation with $\lambda_s = \lambda_l$ well-approximates the charge when $\rho \ll 1$, but overestimates the surface charge for particles with radii approaching or exceeding the Debye length [85]. Solving the Poisson equation (4.36) with the OML surface potential φ_d^{OML} as the boundary condition results in potential distributions and surface charge predictions in good agreement with particle-in-cell (PIC) simulations for $\rho \lesssim 10$ in the absence of emission [21]. Applying an empirical modification to the screening length

$$\lambda_s = \lambda_l \left(1 + 0.48\sqrt{-\beta_i^{-3/2}\rho\varphi_d}\right)^{1/2} \tag{4.39}$$

also predicts the potential distribution and surface charge up to $\rho \sim 10$ with reasonable accuracy [77, 6].

Given a solution for the potential distribution, the surface charge is easy to extract in principle, but a limited subset of existing OM and PIC solutions report the surface charge; data for large dust or emitting grains are particularly lacking. We performed simulations using SCEPTIC[1], a 2D spherical PIC for dust charging [39, 40, 41], to examine the behavior of the surface charge of large, non-emitting grains. The simulations assume $\beta_i = 1$ and span the range of $0.01 \leq \rho \leq 200$ and $0 \leq 0 \leq 5$. Defining μ_p as the proton-to-electron mass ratio, we computed data for $\mu_i = \mu_p$ for validation and comparison to literature [41, 42, 21], and $\mu_i = 27\mu_p$ and $\mu_i = 20\mu_p$ for the representative materials, aluminum and silica.

In Figure 4.32 we compare the PIC results with the Whipple approximation using (4.38) and with empirical modifications to the screening length. The Whipple approximation using λ_l as the screening length overestimates the charge for $\rho \gtrsim 1$ and the error approaches a material-dependent constant factor in the limit of large ρ. In the extreme-size limit, the surface charge is proportional to the surface area, as predicted by (4.38), but with a smaller proportionality constant; the effective screening length approaches a constant value $\lambda_s > \lambda_l$. The empirical modification to λ_s of (4.39) predicts the surface charge to within a factor of two for a wide range of ρ, but will underestimate the charge as $\rho \to \infty$ due to the $\rho^{1/4}$ dependence in that limit.

Based on the PIC simulation data, we propose an alternative empirical fit for $\beta_i = 1$

$$\lambda_s = f_1(\rho, \varphi_d) f_2(\rho) \lambda_l. \tag{4.40}$$

Noting the Whipple approximation accurately predicts the charge for small ρ, and errs by a constant factor for large ρ, we find $f_1(\rho\varphi_d) = 1 + 3.30|\varphi_d|^{1/4}\rho/(\rho+1)$ results in accurate predictions of $\mathcal{Q}_d$ in the thin-sheath and thick-sheath limits, but underestimates the surface charge in the intermediate range. The remaining error after normalizing by $\|\varphi_d\|^{1/4}$ is nearly independent of ion mass in the range of μ_i probed. Empirically, a log-normal correction factor $f_2(\rho) = 1 - 2.32\exp\left(-(\ln(\rho) - 0.92)^2 / \left(2 \cdot 2.14^2\right)\right) / \left(2.14\sqrt{2\pi}\right)$ results in good agreement with PIC data in the range of ρ, μ_i, and u_i examined. SCEPTIC results for $\rho > 200$ were unreliable, but the predicted charge for larger ρ continued to agree closely with simulation data; we expect this empirical fit to give a reasonable estimate of the surface charge in the limit of $\rho \to \infty$.

In the absence of emission, using the analytic expressions instead of the PIC potential in the surface charge calculation incurs a negligible error. Computing the surface potential as described

[1]The version used in this work is available on GitHub at github.com/ihutch/sceptic/tree/9f44a09d9c4eeaa04409bae6a540ca3fdc51fd8f.

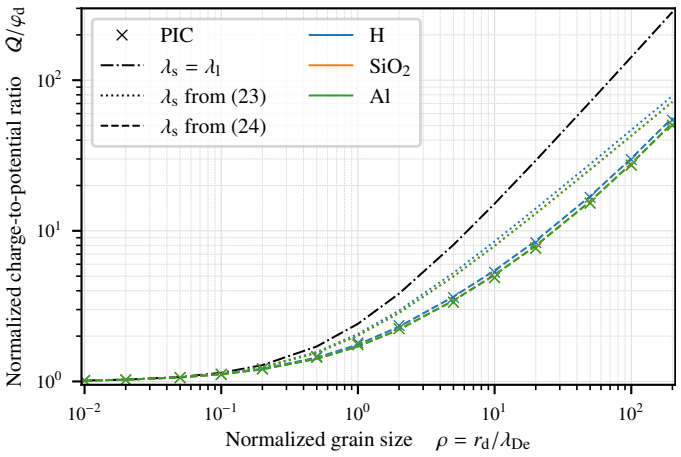

Figure 4.32: Nonlinearity of the surface charge as a function of ρ. PIC simulation data computed with SCEPTIC are compared with the Whipple approximation with different definitions of the effective screening length λ_s in the range $0.01 \leq \rho \leq 200$. For $\beta_i = 1$ and $1 \leq \mu_i/\mu_p \leq 27$, the effective screening length from (4.40) results in a surface charge nearly indistinguishable from PIC data.

in Section 4.4.2 results in agreement with PIC data to within a few percent. Variation of surface charge with drift velocity is nearly proportional to variation in surface potential for moderate values of u_i. The discrepancy between the PIC data and analytic expressions remains within 5% for $u_i \leq 2$ and within 15% for $u_i \leq 5$. Note these results are specific to $T_i = T_e$ ($\beta_i = 1$) and will be inaccurate for arbitrary β_i.

SCEPTIC assumes Boltzmann electrons and does not explicitly simulate electron motion and is unable to probe the effect of thermionic emission on the surface charge. Fortuitously, the thermionic current is negligible compared with the OML currents immediately after impact, and by the time ejecta reach the plasma sensors, the plasma density drops off sufficiently that $\rho \lesssim 1$ for ejecta particles of interest. Solving the Poisson equation using the OML expressions for the density yields reasonable predictions of the potential distribution and surface charge when ρ is order unity [21, 20]. Solving for the charge as a function of the thermionic emission current is a matter of solving the boundary value problem with boundary conditions $\varphi(z = 1) = \varphi_d$ and $\nabla\varphi(z = R) = -2\varphi(R)/R$ when $j_{th} < j^*_{th}$. Empirically, the surface charge is approximately

$$\mathcal{Q}_d(j_{th}) = \mathcal{Q}_d|_{j_{th}=0} \left(\frac{\varphi_d - \varphi^*_d}{\varphi_d|_{j_{th}=0} - \varphi^*_d} \right)^{0.9} \tag{4.41}$$

for a wide range of conditions when $0 \leq j_{th} \leq j^*_{th}$ (Figure 4.33). The potential is non-monotonic and OML density expressions are no longer valid when $j_{th} > j^*_{th}$. No data exist for the surface charge of positive dust grains and we must extrapolate using (4.41). We expect the extrapolation to be sufficiently accurate for order-of-magnitude estimates of the surface charge in this regime.

Force balance

A number of forces may drive the dynamics of charged dust depending on ambient conditions. Broadly, these include forces due to interactions with other particles and external forces due to the

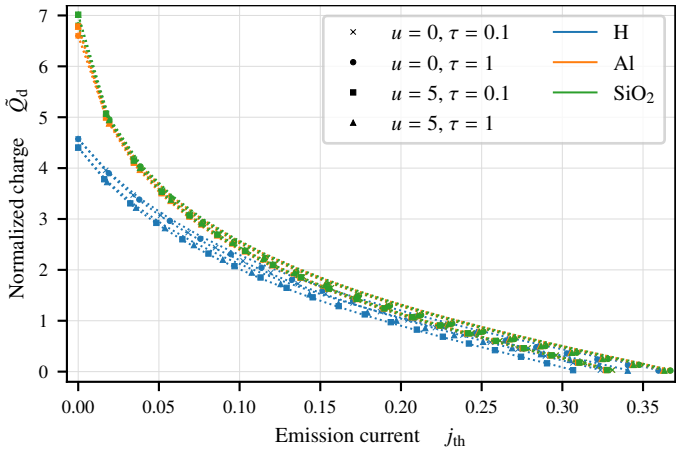

Figure 4.33: Variation of the surface charge with thermionic emission current for $0 \leq j_{th} \leq j_{th}^{*}$ for a range of conditions. Marks indicate solutions to the Poisson equation using the OML density expressions, and dotted lines correspond to predictions using (4.41). Solutions shown correspond to $\rho = 1$ and $\beta_i = 1$, but the empirical fit yields good surface charge estimates for a wide range of conditions.

environment. Particle forces include drag due to momentum transfer by direct collisions with ions, electrons, and neutrals, drag due to Coulomb scattering of ions and electrons, and interactions with other charged dust particles [79, 80]; we include only ion and neutral drag forces. The electron contribution is typically negligible due to the small mass and assumption that the drift velocity is much smaller than the electron thermal speed and our model implicitly assumes that the impact debris are sufficiently separated that dust particles act as isolated grains. Non-particle contributions to the force balance may include electromagnetic, pressure, gravitational, polarization, dipole, thermophoretic, radiation pressure, and rocket forces [79, 80, 6]. The OML-based model assumes unmagnetized species, and under impact plasma conditions magnetic fields are sufficiently weak that only the electric field component of the Lorentz force is relevant. Even in ground-based experiments the gravitational force is negligible over the expansion time scale of milliseconds; the role of gravity will be even less in impacts on spacecraft and small solar system bodies. Figure 4.34 shows the force contributions shortly after impact as a function of particle size.

The ion drag force includes both direct momentum transfer from collected particles and momentum exchange with ions scattered by Coulomb collisions. Integrating over a shifted Maxwellian,

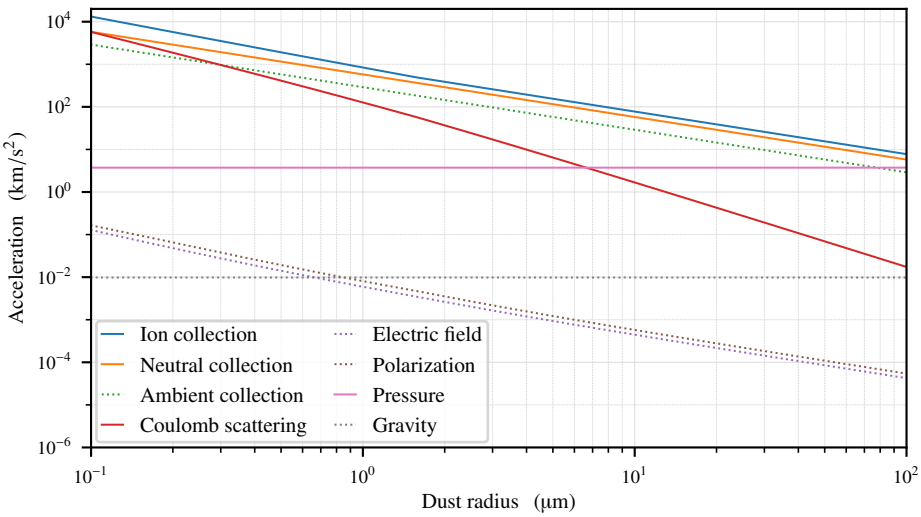

Figure 4.34: Acceleration shortly after impact due to the force terms as a function of dust size. Conditions are computed from the expansion model assuming an aluminum-on-aluminum impact with scale length on the order of the crater size. Particle drag forces assume a relative velocity of 1 km/s. The ambient neutrals are assumed to be air at 300 K and 0.5 Torr, representative of the partial vacuum in the AVGR environment. Solid lines indicate force in the direction of motion and dashed lines indicate a decelerating force. Forces due to the impact products are initially large, but decay rapidly as density drops off with distance and time; in lieu of an ambient neutral background, particles behave ballistically after the first few microseconds.

the OML collection force is [80, 41, 89]

$$\mathscr{F}_{\mathrm{c,i}}^{\mathrm{OML}} = \begin{cases} Z_{\mathrm{i}}^{-1}\beta_{\mathrm{i}}\left(\sqrt{\frac{2}{\pi}}\left(u_{\mathrm{i}}+u_{\mathrm{i}}^{-1}\left(1-2Z_{\mathrm{i}}\beta_{\mathrm{i}}^{-1}\varphi_{\mathrm{d}}\right)\right)\exp\left(-u_{\mathrm{i}}^{2}/2\right)+\right. & \\ \left.\left(2+u_{\mathrm{i}}^{2}-u_{\mathrm{i}}^{-2}-2Z_{\mathrm{i}}\beta_{\mathrm{i}}^{-1}\varphi_{\mathrm{d}}\left(1-u_{\mathrm{i}}^{-2}\right)\right)\mathrm{erf}\left(u_{\mathrm{i}}/\sqrt{2}\right)\right), & \varphi_{\mathrm{d}}<0 \\ Z_{\mathrm{i}}^{-1}\beta_{\mathrm{i}}\left(\frac{1}{\sqrt{2\pi}}\left(\left(u_{\mathrm{i}}+u_{\mathrm{i}}^{-1}-\left(1-u_{\mathrm{i}}^{-2}\right)\sqrt{2Z_{\mathrm{i}}\beta_{\mathrm{i}}^{-1}\varphi_{\mathrm{d}}}\right)\exp\left(-u_{\mathrm{i}+}^{2}\right)+\right.\right. & \\ \left.\left.\left(u_{\mathrm{i}}+u_{\mathrm{i}}^{-1}+\left(1-u_{\mathrm{i}}^{-2}\right)\sqrt{2Z_{\mathrm{i}}\beta_{\mathrm{i}}^{-1}\varphi_{\mathrm{d}}}\right)\exp\left(-u_{\mathrm{i}-}^{2}\right)\right)+\right. & \varphi_{\mathrm{d}}>0 \\ \left.\left(2+u_{\mathrm{i}}-u_{\mathrm{i}}^{-2}-2Z_{\mathrm{i}}\beta_{\mathrm{i}}^{-1}\varphi_{\mathrm{d}}\left(1-u_{\mathrm{i}}^{-2}\right)\right)\left(\mathrm{erf}\left(u_{\mathrm{i}+}\right)+\mathrm{erf}\left(u_{\mathrm{i}-}\right)\right)\right), & \end{cases} \tag{4.42}$$

where the normalized force in the relative drift direction is $\mathscr{F} = F/\left(\pi r_{\mathrm{d}}^{2} n_{\mathrm{e}\infty} k T_{\mathrm{e}}\right)$. In the OML limit and for positively charged dust we simply set $\mathscr{F}_{\mathrm{c,i}} = \mathscr{F}_{\mathrm{c,i}}^{\mathrm{OML}}$. The above expression, however overestimates the drag force for large, negatively charged dust grains due to sheath formation [41]. Computing ion currents at the sheath edge using the presheath potential in (4.42), $\mathscr{F}_{\mathrm{c,i}} = \mathscr{F}_{\mathrm{c,i}}^{\mathrm{OML}}(\varphi_{\mathrm{d}} - \Delta\varphi)$, yields a good estimate of the drag force in the thin-sheath limit [98]. There is no obvious definition of $\Delta\varphi$ for intermediate-size dust, so we define an effective potential by imposing current balance, $j_{\mathrm{c,i}}(\varphi_{\mathrm{eff}}) = j_{\mathrm{c,e}}(\varphi_{\mathrm{d}}) - j_{\mathrm{th}}$. Plugging into the ion current and solving for φ_{eff} yields

$$\varphi_{\mathrm{eff}} = \begin{cases} \sqrt{\frac{2\mu_{\mathrm{i}}\beta_{\mathrm{i}}}{\pi}}\frac{u_{\mathrm{i}}}{Z_{\mathrm{i}}\mathrm{erf}\left(u_{\mathrm{i}}/\sqrt{2}\right)}\left(j_{\mathrm{th}}-\exp\left(\varphi_{\mathrm{d}}\right)\right)+ & \\ \frac{\beta_{\mathrm{i}}u_{\mathrm{i}}}{\sqrt{2\pi}Z_{\mathrm{i}}}\left(\sqrt{\frac{\pi}{2}}\left(u_{\mathrm{i}}+u_{\mathrm{i}}^{-1}\right)+\frac{\exp\left(-u_{\mathrm{i}}^{2}/2\right)}{\mathrm{erf}\left(u_{\mathrm{i}}/\sqrt{2}\right)}\right), & u>0 \\ Z_{\mathrm{i}}^{-1}\beta_{\mathrm{i}}\left(1+\sqrt{\mu_{\mathrm{i}}\beta_{\mathrm{i}}^{-1}}\left(j_{\mathrm{th}}-\exp\left(\varphi_{\mathrm{d}}\right)\right)\right), & u=0. \end{cases} \tag{4.43}$$

The drag due to ions scattered by Coulomb collisions is [50, 42]

$$\mathscr{F}_{\mathrm{sc,i}} = 4\beta_{\mathrm{i}}\left(Z_{\mathrm{i}}\beta_{\mathrm{i}}^{-1}\varphi_{\mathrm{d}}\right)^{2}u_{\mathrm{i}}^{-2}\left(\mathrm{erf}\left(u_{\mathrm{i}}/\sqrt{2}\right)-\sqrt{\frac{2}{\pi}}u_{\mathrm{i}}\exp\left(-u_{\mathrm{i}}^{2}/2\right)\right)\ln\Lambda, \tag{4.44}$$

Setting the upper impact parameter cutoff such that the distance of closest approach is equal to some effective screening length λ_{sc}, the Coulomb logarithm is

$$\ln\Lambda = \ln\left(\frac{b_{90}+\lambda_{\mathrm{sc}}}{b_{90}+r_{\mathrm{d}}}\right), \tag{4.45}$$

where b_{90} is the large angle scattering parameter. A great deal of ambiguity remains with respect to

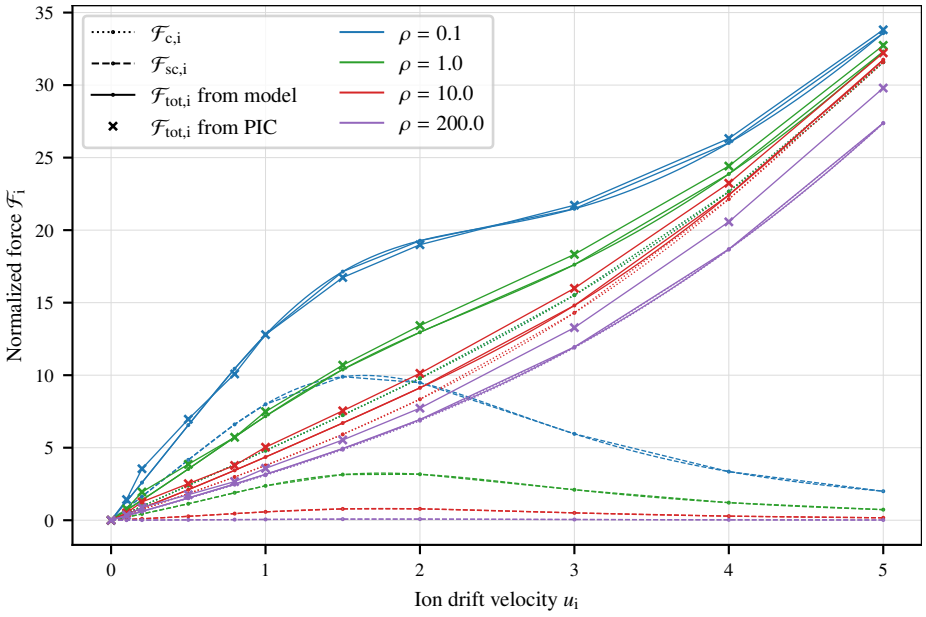

Figure 4.35: Comparison of the normalized ion forces computed with SCEPTIC and using the analytic expressions. Results shown are for hydrogen, but data for other mass ratios show similar trends.

the optimal definitions of b_{90} and λ_{sc} [42]. We take an approach similar to [6] and define

$$\frac{b_{90}}{r_d} = |\varphi_d|\beta_i^{-1}(1+u_i)^{-1} \tag{4.46}$$

$$\frac{\lambda_{sc}}{r_d} = \rho^{-1}\frac{\lambda_s}{\lambda_{De}} + 1, \tag{4.47}$$

where we compute λ_s using (4.40).

As Figure 4.35 shows, computing the ion forces in this manner gives reasonable agreement with PIC simulation over a broad range of u_i and ρ when $\beta_i = 1$. We find a minor underestimate of the drag force in the thin sheath limit, where the scattering component is negligible and the collection force dominates. Adding $u_i/2$ to the normalized force accounts for the discrepancy in the thin-sheath limit remarkably well [98]. We do not include this correction, however, because the physical motivation is unclear and the $<$10% error has minimal effect on dust dynamics.

Setting $\varphi_d = 0$ in (4.42) gives the neutral drag force

$$\mathscr{F}_{c,n} = \beta_n \frac{n_n}{n_{e\infty}}\left(\sqrt{\frac{2}{\pi}}\left(u_n + u_n^{-1}\right)\exp\left(-u_n^2/2\right) + \left(2 + u_n^2 - u_n^{-2}\right)\operatorname{erf}\left(u_n/\sqrt{2}\right)\right). \tag{4.48}$$

Neutral drag includes both contributions from material vaporized on impact and from gases present in the ambient environment, and may dominate other forces depending on ambient and impact conditions.

The ion and neutral drag forces dominate throughout the expansion under most plausible conditions. We include contributions due to the electric field, pressure, and polarization forces for

completeness, however, as they may be non-negligible immediately after impact depending on conditions. These forces, neglecting higher order terms, are [30, 6]

$$F_{\mathrm{E}} = Q_{\mathrm{d}} E \tag{4.49}$$

$$F_{\mathrm{p}} = -\frac{4}{3}\pi r_{\mathrm{d}}^3 \frac{\partial p}{\partial r} \tag{4.50}$$

$$F_{\mathrm{pol}} = -\frac{Q_{\mathrm{d}}^2}{8\pi\varepsilon_0\left(\lambda_{\mathrm{s}}^2 + r_{\mathrm{d}}^2\right)} \frac{\partial \lambda_{\mathrm{s}}}{\partial r}, \tag{4.51}$$

where F_{E} is the force due to the electric field, F_{p} is the force due to the pressure gradient, and F_{pol} is the force due to surface charge polarization by the electric and pressure fields. The total body force due to external fields is $F_{\mathrm{ext}} = F_{\mathrm{E}} + F_{\mathrm{p}} + F_{\mathrm{pol}}$.

Taking the gradient of the potential, the electric field consistent with the expansion model is

$$E(r,t) = -\frac{d\Phi}{dr} = -\frac{2}{r - v_0 t}\Phi(r,t). \tag{4.52}$$

The pressure is $p = \sum_\alpha n_\alpha k T_\alpha$ and the gradient is $dp/dr = \sum_\alpha k T_\alpha dn_\alpha/dr$. For impact-generated species the density gradient is

$$\frac{dn_\alpha}{dr} = -\frac{\Omega^2(r - u_0 t)}{C_{\mathrm{s}}^2\left(1 + \Omega^2 t^2\right)} n_\alpha(r,t). \tag{4.53}$$

The gradient of $\lambda_{\mathrm{De}} = \sqrt{\varepsilon_0 k T_{\mathrm{e}} / \left(n_{\mathrm{e}\infty} e^2\right)}$ is

$$\frac{\partial \lambda_{\mathrm{s}}}{\partial r} = \frac{\Omega^2\left(r - u_0 t\right)}{2C_{\mathrm{s}}^2\left(1 + \Omega^2 t^2\right)} \lambda_{\mathrm{s}}. \tag{4.54}$$

as long as $\lambda_{\mathrm{s}}/\lambda_{\mathrm{De}}$ varies much more gradually than the density.

Energy and mass balance

The energy flux from collected particles, assuming all kinetic energy is converted to heat and transferred to the dust surface, consists of the kinetic energy of the particles in the bulk plasma and the energy gained or lost in the sheath

$$P_{\mathrm{c},\alpha} = P_{\mathrm{k},\alpha} + P_{\mathrm{s},\alpha}. \tag{4.55}$$

Defining the normalized energy flux $\mathscr{P} = P/\left(\sqrt{8\pi} r_{\mathrm{d}}^2 n_{\mathrm{e}\infty} k T_{\mathrm{e}} v_{\mathrm{te}}\right)$ and accounting for the chosen sign convention, the sheath contributions to the electron and ion energy fluxes, respectively, are $\mathscr{P}_{\mathrm{s,e}} = j_{\mathrm{e}}\varphi_{\mathrm{d}}$ and $\mathscr{P}_{\mathrm{s,i}} = -j_{\mathrm{i}}\varphi_{\mathrm{d}}$. Integrating over a Maxwellian distribution yields the kinetic flux at zero drift velocity [80]

$$\mathscr{P}_{\mathrm{k,e}}^{\mathrm{OML}} = \begin{cases} (2 - \varphi_{\mathrm{d}})\exp(\varphi_{\mathrm{d}}), & \varphi_{\mathrm{d}} < 0 \\ 2 + \varphi_{\mathrm{d}}, & \varphi_{\mathrm{d}} > 0 \end{cases} \tag{4.56}$$

$$\mathscr{P}_{\mathrm{k,i}}^{\mathrm{OML}} = \begin{cases} Z_{\mathrm{i}}^{-1}\beta_{\mathrm{i}}^{3/2}\mu_{\mathrm{i}}^{-1/2}\left(2 - Z_{\mathrm{i}}\beta_{\mathrm{i}}^{-1}\varphi_{\mathrm{d}}\right), & \varphi_{\mathrm{d}} < 0 \\ Z_{\mathrm{i}}^{-1}\beta_{\mathrm{i}}^{3/2}\mu_{\mathrm{i}}^{-1/2}\left(2 + Z_{\mathrm{i}}\beta_{\mathrm{i}}^{-1}\varphi_{\mathrm{d}}\right)\exp\left(-Z_{\mathrm{i}}\beta_{\mathrm{i}}^{-1}\varphi_{\mathrm{d}}\right), & \varphi_{\mathrm{d}} > 0, \end{cases} \tag{4.57}$$

and, integrating over a drifting Maxwellian when $u > 0$ results in

$$\mathscr{P}_{\mathrm{k,i}}^{\mathrm{OML}} = \begin{cases} \frac{1}{4} Z_{\mathrm{i}}^{-1} \beta_{\mathrm{i}}^{3/2} \mu_{\mathrm{i}}^{-1/2} \Bigg(\left(5 + u_{\mathrm{i}}^2 - 2 Z_{\mathrm{i}} \beta_{\mathrm{i}}^{-1} \varphi_{\mathrm{d}}\right) \exp\left(-u_{\mathrm{i}}^2/2\right) + \\ \qquad \sqrt{\frac{\pi}{2}} \left(3u_{\mathrm{i}}^{-1} + 6u_{\mathrm{i}} + u_{\mathrm{i}}^3 - 2\left(u_{\mathrm{i}} + u_{\mathrm{i}}^{-1}\right) Z_{\mathrm{i}} \beta_{\mathrm{i}}^{-1} \varphi_{\mathrm{d}}\right) \times \\ \qquad \mathrm{erf}\left(u_{\mathrm{i}}/\sqrt{2}\right) \Bigg), & \varphi_{\mathrm{d}} < 0 \\ \frac{1}{8} Z_{\mathrm{i}}^{-1} \beta_{\mathrm{i}}^{3/2} \mu_{\mathrm{i}}^{-1/2} \Bigg(\left(5 + u_{\mathrm{i}}^2 - \left(3u_{\mathrm{i}}^{-1} + u_{\mathrm{i}}\right) \sqrt{2 Z_{\mathrm{i}} \beta_{\mathrm{i}}^{-1} \varphi_{\mathrm{d}}}\right) \exp\left(-u_{\mathrm{i}+}^2\right) + \\ \qquad \left(5 + u_{\mathrm{i}}^2 + \left(3u_{\mathrm{i}}^{-1} + u_{\mathrm{i}}\right) \sqrt{2 Z_{\mathrm{i}} \beta_{\mathrm{i}}^{-1} \varphi_{\mathrm{d}}}\right) \exp\left(-u_{\mathrm{i}-}^2\right) + \\ \qquad \sqrt{\frac{\pi}{2}} \left(3u_{\mathrm{i}}^{-1} + 6u_{\mathrm{i}} + u_{\mathrm{i}}^3 - 2\left(u_{\mathrm{i}} + u_{\mathrm{i}}^{-1}\right) Z_{\mathrm{i}} \beta_{\mathrm{i}}^{-1} \varphi_{\mathrm{d}}\right) \times \\ \qquad \left(\mathrm{erf}\left(u_{\mathrm{i}+}\right) + \mathrm{erf}\left(u_{\mathrm{i}-}\right)\right) \Bigg), & \varphi_{\mathrm{d}} > 0. \end{cases} \tag{4.58}$$

To account for the decreased ion flux to large dust due to sheath formation, we compute $P_{\mathrm{k,i}}$ with the effective potential φ_{eff} previously defined. Evaluating at $\varphi = 0$, the energy flux due to neutral collection is

$$\mathscr{P}_{\mathrm{k,n}} = \begin{cases} 2 \frac{n_{\mathrm{n}}}{n_{\mathrm{e}\infty}} \beta_{\mathrm{n}}^{3/2} \mu_{\mathrm{n}}^{-1/2}, & u_{\mathrm{n}} = 0 \\ \frac{1}{4} \frac{n_{\mathrm{n}}}{n_{\mathrm{e}\infty}} \beta_{\mathrm{n}}^{3/2} \mu_{\mathrm{n}}^{-1/2} \Bigg(\left(5 + u_{\mathrm{n}}^2\right) \exp\left(-u_{\mathrm{n}}^2/2\right) + \\ \qquad \sqrt{\frac{\pi}{2}} \left(3u_{\mathrm{n}}^{-1} + 6u_{\mathrm{n}} + u_{\mathrm{n}}^3\right) \mathrm{erf}\left(u_{\mathrm{n}}/\sqrt{2}\right) \Bigg), & u_{\mathrm{n}} > 0. \end{cases} \tag{4.59}$$

The heat lost to thermionic electrons emitted at the dust surface temperature is, on average, $W + 2kT_{\mathrm{d}}$ per particle, so $\mathscr{P}_{\mathrm{th}} = -j_{\mathrm{th}} \left(W/kT_{\mathrm{e}} + 2\tau\right)$.

We account for recombination, thermalization, blackbody radation, and ablation at the dust surface $P_{\mathrm{surf}} = P_{\mathrm{neu}} + P_{\mathrm{therm}} + P_{\mathrm{rad}}$. Assuming all collected ions recombine and the dust surface absorbs the emitted energy, $P_{\mathrm{neu}} = U_{\mathrm{i}} I_{\mathrm{c,i}}/Z_{\mathrm{i}} e$, where U_{i} is the total energy to reach the ionization state Z_{i}; normalizing, $\mathscr{P}_{\mathrm{neu}} = Z_{\mathrm{i}}^{-1} j_{\mathrm{i}} U_{\mathrm{i}}/kT_{\mathrm{e}}$. Particles of unlike material leave the surface at the dust temperature [61], resulting in a cooling energy flux of $P_{\mathrm{therm,amb}} = -2kT_{\mathrm{d}} \Gamma_{\mathrm{n,amb}}/m_{\mathrm{n,amb}}$. We assume the dust is of like material to the ions and neutrals ejected on impact and the "unlike" contribution is due only to fluxes from ambient neutrals; recombined ions will also contribute to this term if the dust and ions are of unlike material. Computing the OML mass flux with $\varphi_{\mathrm{d}} = 0$,

$$\Gamma_{\mathrm{n}} = \begin{cases} \sqrt{8\pi} r_{\mathrm{d}}^2 m_{\mathrm{n}} n_{\mathrm{n}} v_{\mathrm{tn}}, & u_{\mathrm{n}} = 0 \\ \pi r_{\mathrm{d}}^2 m_{\mathrm{n}} n_{\mathrm{n}} v_{\mathrm{tn}} \left(\left(u_{\mathrm{n}} + u_{\mathrm{n}}^{-1}\right) \mathrm{erf}\left(u_{\mathrm{n}}/\sqrt{2}\right) + \sqrt{\frac{2}{\pi}} \exp\left(-u_{\mathrm{n}}^2/2\right) \right), & u_{\mathrm{n}} > 0. \end{cases} \tag{4.60}$$

Treating dust grains as blackbody radiators described by the Stefan-Boltzmann law,

$$P_{\mathrm{rad}} = -4\pi r_{\mathrm{d}}^2 \varepsilon_{\mathrm{d}} \sigma_{\mathrm{sb}} \left(T_{\mathrm{d}}^4 - T_{\mathrm{w}}^4\right), \tag{4.61}$$

where ε_d is the material emissivity and σ_{sb} is the Stefan-Boltzmann constant. We use $\sigma_{sb} = 0.63$ for aluminum and $\sigma_{sb} = 0.18$ for the regolith simulant. In space, $T_w \approx 0$, but in a confined environment the presence of a chamber wall at non-negligible temperature T_w reduces the heat lost to thermal radiation.

Ions and neutrals generated on impact are of the same material as the condensed phase debris, so $m_{n,imp} = m_i$ and the dust growth rate is $\Gamma_{acc} = m_i I_i / Z_i e + \Gamma_{n,imp}$. The cooling energy due to these particles thermalizing and combining with the dust surface is $P_{therm,acc} = -\Gamma_{acc} h_d$. If the heat flux to the surface is sufficient, dust particles will ablate, potentially leading to dust destruction. We model ablation at the surface using an evaporation model [99]

$$\Gamma_{abl} = 4\pi r_d^2 m_{mat} \frac{p_{sat}}{\sqrt{2\pi m_{mat} k T_d}}, \tag{4.62}$$

where m_{mat} is the molecular weight of the dust material and p_{sat} is the saturation pressure given by the Clausius-Clapeyron equation

$$p_{sat} = p \exp\left(\frac{m_{mat} \Delta h_{vap} (T_d - T_b)}{k T_d T_b} \right), \tag{4.63}$$

where Δh_{vap} is the heat of vaporization and T_b is the boiling point at pressure $p = \sum_\alpha n_\alpha k T_\alpha$. The associated energy flux is $P_{abl} = -\Gamma_{abl} \Delta h_{vap}$. Sputtering processes may significantly contribute to dust erosion [61, 75], but play a negligible role on temperature, density, and time scales relevant to impact plasma.

4.4.3 Dust modeling results

Dust survival

Ejected particles experience temperatures on the order of 1–2 eV and densities $n_e > 10^{23}\,\mathrm{m}^{-3}$ during the first few microseconds after impact. Under these conditions, rapid ablation may limit the survival time of nano-scale particles. We study the effect of plasma density and dust size on survivability by integrating (4.26) and (4.27), holding the ambient conditions constant. We define destruction as the point when $r_d < 10\,\mathrm{nm}$. The exact value of this parameter has minimal effect on the computed survival time because $m_d \propto r_d^2$ while the energy fluxes and ablation scale as r_d^2. Consequently, decreasing dust size leads to a positive feedback loop and accelerating destruction.

Figure 4.36 shows the effect of plasma density and dust radius on survival time in a 1 eV aluminum plasma. Particles that survive the first microseconds after impact will experience negligible ablation at later times because the plasma density and temperature drop rapidly; indeed, minor dust growth may occur due to particle collection. The conditions immediately after impact remain uncertain, but these results suggest ablation at early time may impose a lower bound on debris size. Ablation may also limit dusty plasma effects in micrometeoroid impacts because impacts by smaller particles traveling at greater relative velocities lead to less condensed phase ejecta and higher plasma densities.

Simulated dust trajectories

We compare results obtained from the dust model with experimental data by integrating dust trajectories using the dust charging and dynamics model with plasma conditions computed from the

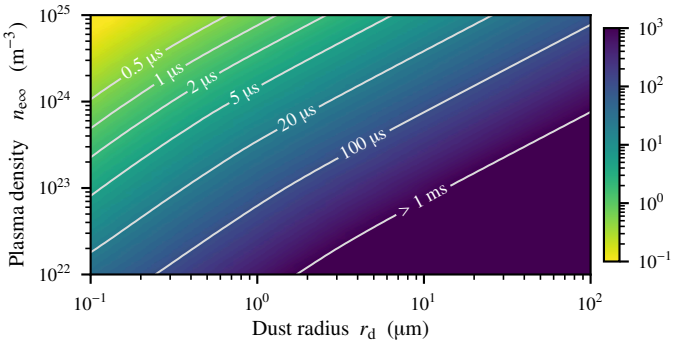

Figure 4.36: Dust survival time as a function of plasma density and initial dust radius for an aluminum dust particle immersed in an aluminum plasma with $T_i = T_e = 1\,\mathrm{eV}$. The results shown assume plasma and dust expanding at $1\,\mathrm{km/s}$ and an impact-generated gas density $n_{n,imp} = 100 n_e$. Computed survival times vary with the expansion velocity, $n_{n,imp}/n_e$, plasma conditions, and material, but results are qualitatively similar for reasonable choices.

renormalization-group expansion model. We use a plasma temperature of $T_i = T_e = 0.33\,\mathrm{eV}$, initial expansion velocity of $v_0 = 1\,\mathrm{km/s}$, and impact-generated neutral density $n_{n,imp} = 100 n_e$ unless otherwise noted. Ions are singly charged and we treat the regolith simulant as a ion species with the average atomic mass of 20 proton masses. We assume a 0.5 Torr background neutral population at 300 K, which corresponds roughly to $n_{n,amb} = 1.6 \cdot 10^{22}\,\mathrm{m}^{-3}$, to account for the low vacuum environment at AVGR.

We estimate the total charge produced using (4.21). The initial scale length for the aluminum impact is estimated by the crater radius computed using (4.22). The regolith impact occurs over a longer time scale and ejects much of the debris at later time and with lower velocity; the bulk of charge attachment, however, occurs shortly after impact. We therefore use the radius of the initial plume of fast, vertically traveling ejecta as the scale length. Based on high speed imagery, $L_0 \approx 1\,\mathrm{cm}$.

Dust charging occurs on short enough time scales that the surface potential and charge are quasi-equilibrium given r_d, T_d, and v_d. Evolution of the dust temperature and velocity, however, depends strongly on the ejection temperature T_{d0} and velocity v_{d0}. Experimental observations provide a rough bound on the ejection speed, but no data exist for the debris temperature after impact. We integrate many trajectories with initial conditions uniformly selected from $v_{d0}, T_{d0} \in [500, 2000]\,\mathrm{m/s} \times [1000, 2400]\,\mathrm{K}$ to study the effect of initial temperature and velocity. We conduct the simulation for particles with $r_d = 1\,\mu\mathrm{m}$ and $r_d = 5\,\mu\mathrm{m}$ to probe size effects.

In Figure 4.37 we overlay the surface potential as a function of distance from impact site from all integrated trajectories. The Debye length is on the order of tens of nanometers initially, so $r_d \gg \lambda_{De}$ and the thin-sheath limit applies. Plasma currents are sufficient that the thermionic current is negligible by comparison. As dust travels into regions of lower plasma density, however, the thermionic current may become dominant, and some particles charge positively. Small grains may cool sufficiently before reaching the sensor (roughly 1 m) that the surface charge changes twice. This suggests that both sensor location and ejection conditions determine the sign of charge observed.

Regolith grains charge positively under a wider range of conditions than aluminum due to thermionic emission. This is consistent with the observation of mostly negative charge in the plasma

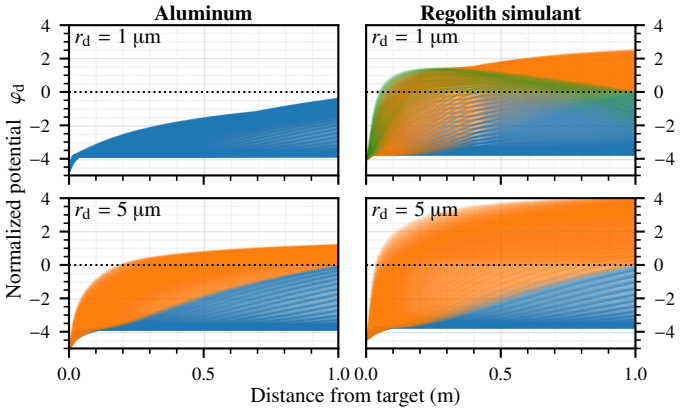

Figure 4.37: Normalized surface potential as a function of distance from target for aluminum and regolith particles ejected with varying initial temperature and velocity. Each trajectory corresponds to an initial condition uniformly sampled from the space $v_{d0}, T_{d0} \in [500, 2000]\,\mathrm{m/s} \times [1000, 2400]\,\mathrm{K}$. The surface charge may remain strictly negative (blue), transition from negative to positive (orange), or change signs twice before reaching the target (green).

data from aluminum impacts and positive charge in impacts on regolith simulant. The material dependence is especially evident for small grains; the charge on a $r_d = 1\,\mu\mathrm{m}$ aluminum particle remains strictly negative under most conditions, but regolith grains of the same size may charge positively. Reasons for this behavior are twofold. First, aluminum has much lower melting and boiling temperatures and heat loss due to ablation regulates the temperature. Second, the energy flux to the surface by collected particles is greater for the regolith because the atomic mass is less than aluminum. Ion and neutral collection power (4.58) and (4.59) depend on $\mu_{i,n}^{-1/2}$ and more massive ions lead to a more negative surface potential and decreased electron current and heat flux.

Figure 4.38 shows the surface charge at the plasma sensor distance of 1 m as a function of the initial temperature and velocity. The difference in surface charge trends is less pronounced for larger particles, but regolith debris tend to charge more positively. The surface charge of small ejecta exhibits a strong dependence on the initial velocity; fast particles have less time to cool enough that the surface charge returns to negative. The initial temperature such that grains reach the plasma sensors with positive surface charge is inversely related to grain size. Small grains, however, are ejected at higher velocities than larger debris and heat more rapidly after impact due to higher surface area-to-mass ratio. Conditions in the post-impact environment are sufficiently extreme to heat regolith grains with $r_d \lesssim 1$–$2\,\mu\mathrm{m}$ and aluminum grains with $r_d \lesssim 5\,\mu\mathrm{m}$ past the melting point within a few microseconds. This is consistent with evidence of liquid-phase ejecta in impacts on both materials [78].

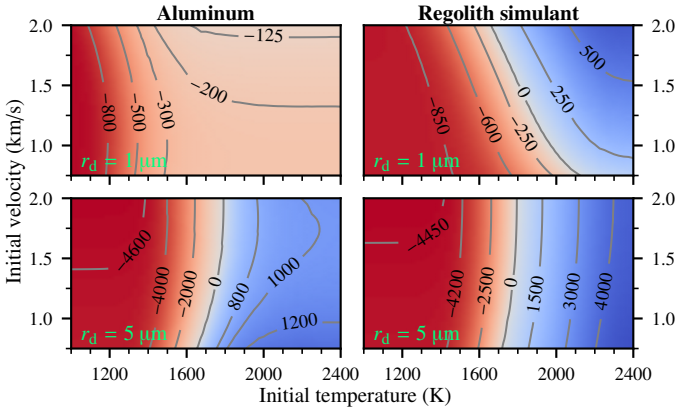

Figure 4.38: Surface charge 1 m from the target (approximately the distance to the plasma sensors) in units of electron charge (Q_d/e) for aluminum and regolith particles as a function of ejection temperature and velocity. The sign of charge strongly depends on grain size, material, and initial conditions.

5 Conclusions

Within this project, we developed and deployed a new suite of hypervelocity impact sensors, including RF antennas, plasma faraday cups, and witness plates. We executed a ground-based hypervelocity impact experiment at the AVGR to make measurements of impacts over a range of target materials and target bias. Finally, we developed new models to interpret these measurements. Restating our major findings:

1. The background gas slowed the expanding plasma plume from approximately 16 km/s to 10 km/s, which resulted in generation of a Rayleigh-Taylor instability. Using high-speed imagery, we found that the expanding, charged dust ring pulled the plasma, causing the plasma duration to increase by a factor of 10. The dusty plasma was highly negative with current densities up to 0.1 A/m^2, which is 1000 times denser than previously predicted. This has profound implications for spacecraft safety due to RF emission from dusty plasmas.

2. The dust distribution for regolith simulant followed power law with a D-value of 1.69, which is in agreement with results from disruption studies on solid basalt. We observed a transition with increasing ejecta size from circular to more irregular shapes, which provides information about the phase of the material.

3. Through extension of the OML theory, we were able to characterize the evolution of ejecta interactions with the background, accounting for physical terms important in high energy density environments, such as thermionic emission and radiation. The model outputs the charge, momentum, energy and mass flux across a range of physical regimes spanned by the expanding plasma.

This research has led to two peer-reviewed journal publications to date, with several more in progress, in addition to 11 conference and seminar presentations. We expect that the measurements gathered in the experimental campaign will continue to provide research opportunities for new students in the future. The OML dust charging model and hydrodynamics simulations developed through this project will be crucial in capturing dusty plasma effects and plasma expansion geometry both in future ground-based experiments as well as extrapolating this phenomena to the impacts experienced by spacecraft in the vacuum of space.

Bibliography

[1] A. Francesconi. Characterization of Ejecta From Hvi on Spacecraft Outer Surfaces. *IADC-11-05*, 2013. https://www.semanticscholar.org/paper/CHARACTERIZATION-OF-EJECTA-FROM-HVI-ON-SPACECRAFT-Francesconi/3fc7d0af1ff38325d0f6cd883af00c5d5ffb53c5.

[2] Esraa Mousa Ali, Nor Zaihar Yahaya, Perumal Nallagownden, and Bilal Hasan Alqasem. Enhanced Dickson voltage multiplier rectenna by developing analytical model for radio frequency harvesting applications. *International Journal of RF and Microwave Computer-Aided Engineering*, 29(1):e21657, jan 2019. http://doi.wiley.com/10.1002/mmce.21657.

[3] J. E. Allen. Probe theory - the orbital motion approach. *Physica Scripta*, 45(5):497–503, May 1992.

[4] J. E. Allen, B. M. Annaratone, and U. de Angelis. On the orbital motion limited theory for a small body at floating potential in a Maxwellian plasma. *Journal of Plasma Physics*, 63(4):299–309, May 2000.

[5] Ya L. Al'pert, A. V. Gurevich, and L. P. Pitaevskii. Space physics with artificial satellites. *American Journal of Physics*, 34(6):544–544, 1966.

[6] D. U. B. Aussems, S. A. Khrapak, İ. Doğan, M. C. M. van de Sanden, and T. W. Morgan. An analytical force balance model for dust particles with size up to several Debye lengths. *Physics of Plasmas*, 24(11):113702, November 2017.

[7] M. Bacharis. Floating potential of large dust grains with electron emission. *Physics of Plasmas*, 21(7):074501, 2014.

[8] Minas Bacharis, Michael Coppins, and John E. Allen. Dust in tokamaks: An overview of the physical model of the dust in tokamaks code. *Physics of Plasmas*, 17(4):042505, 2010.

[9] Constantine A. Balanis. Broadband Dipoles and Matching Techniques. In *Antenna Theory*, chapter 9, pages 497–548. Wiley, Hoboken, NJ, 3 edition, 2005.

[10] Constantine A. Balanis. Frequency Independent Antennas, Antenna Miniaturization, and Fractal Antennas. In *Antenna Theory*, chapter 11, pages 611–652. Wiley, Hoboken, NJ, 3 edition, 2005.

[11] Elmar Buhl, Frank Sommer, Michael H. Poelchau, Georg Dresen, and Thomas Kenkmann. Ejecta from experimental impact craters: Particle size distribution and fragmentation energy. *Icarus*, 237:131–142, 2014.

[12] S. Close, P. Colestock, L. Cox, M. Kelley, and N. Lee. Electromagnetic pulses generated by meteoroid impacts on spacecraft. *Journal of Geophysical Research: Space Physics*, 115(A12), December 2010.

[13] John Douglas Cockcroft and Ernest TS Walton. Experiments with high velocity positive ions.—(I) Further developments in the method of obtaining high velocity positive ions. *Proceedings of the royal society of London. Series A, containing papers of a mathematical and physical character*, 136(830):619—-630, 1932.

[14] David A. Crawford. Computational Modeling of Electrostatic Charge and Fields Produced by Hypervelocity Impact. *Procedia Engineering*, 103:89–96, 2015.

[15] David A. Crawford and Peter H. Schultz. Laboratory observations of impact–generated magnetic fields. *Nature*, 336:50, November 1988.

[16] David A. Crawford and Peter H. Schultz. Electromagnetic properties of impact-generated plasma, vapor and debris. *International Journal of Impact Engineering*, 23(1):169–180, 1999.

[17] David A. Crawford and Peter H. Schultz. Electromagnetic properties of impact-generated plasma, vapor and debris. *International Journal of Impact Engineering*, 23(1, Part 1):169–180, 1999.

[18] G. L. Delzanno, A. Bruno, G. Sorasio, and G. Lapenta. Exact orbital motion theory of the shielding potential around an emitting, spherical body. *Physics of Plasmas*, 12(6):062102, 2005.

[19] G. L. Delzanno, G. Lapenta, and M. Rosenberg. Attractive Potential around a Thermionically Emitting Microparticle. *Phys. Rev. Lett.*, 92(3):035002, January 2004.

[20] Gian Luca Delzanno and Xian-Zhu Tang. Charging and Heat Collection by a Positively Charged Dust Grain in a Plasma. *Phys. Rev. Lett.*, 113(3):035002, July 2014.

[21] Gian Luca Delzanno and Xian-Zhu Tang. Comparison of dust charging between orbital-motion-limited theory and particle-in-cell simulations. *Physics of Plasmas*, 22(11):113703, 2015.

[22] John F Dickson. On-Chip High-Voltage Generation in MNOS Integrated Circuits Using an Improved Voltage Multiplier Technique. *IEEE Journal of Solid-State Circuits*, SC-11(3):374–378, 1976.

[23] Ben Estacio, Gil Shohet, Sean A. Q. Young, Isaac Matthews, Nicolas Lee, and Sigrid Close. Dust and atmospheric influence on plasma properties observed in light gas gun hypervelocity impact experiments. *International Journal of Impact Engineering*, 151:103833, May 2021.

[24] Markus Flaig and Tomasz Plewa. Self-generated magnetic fields in blast-wave driven Rayleigh-Taylor experiments. *High Energy Density Physics*, 17:46–51, dec 2015.

[25] D A Freiwald and R A Axford. Approximate spherical blast theory including source mass. *Journal of Applied Physics*, 46(3):1171–1174, 1975. https://doi.org/10.1063/1.321722.

[26] V.C. Frost. Meteoroid damage assessment. Technical Report NASA SP-8042, NASA, May 1970.

[27] Akira Fujiwara, Goro Kamimoto, and Akimasa Tsukamoto. Destruction of basaltic bodies by high-velocity impact. *Icarus*, 31(2):277–288, June 1977.

[28] David B. Geohegan. Physics and diagnostics of laser ablation plume propagation for high-Tc superconductor film growth. *Thin Solid Films*, 220(1-2):138–145, nov 1992. https://www.sciencedirect.com/science/article/pii/004060909290562P.

[29] J Grun, J Stamper, C Manka, J Resnick, R Burris, and J Crawford. Instability of Taylor-Sedov Blast Waves Propagating through a Uniform Gas. *Physical Review Letters*, 66(21), 1991. https://journals.aps.org/prl/pdf/10.1103/PhysRevLett.66.2738.

[30] S. Hamaguchi and R. T. Farouki. Plasma–particulate interactions in nonuniform plasmas with finite flows. *Physics of Plasmas*, 1(7):2110–2118, July 1994.

[31] S. S. Harilal, C. V. Bindhu, M. S. Tillack, F. Najmabadi, and A. C. Gaeris. Internal structure and expansion dynamics of laser ablation plumes into ambient gases. *Journal of Applied Physics*, 93(5):2380–2388, mar 2003. http://aip.scitation.org/doi/10.1063/1.1544070.

[32] Dominic Heunoske, Martin Schimmerohn, Jens Osterholz, and Frank Schäfer. Time-resolved Emission Spectroscopy of Impact Plasma. *Procedia Engineering*, 58:624–633, 2013.

[33] Y. M. Hew and S. Close. Hypervelocity impact flash expansion geometry under various spacecraft surface electrical conditions. *International Journal of Impact Engineering*, 150:103792, April 2021.

[34] Y. M. Hew, A. Goel, S. Close, and N. Lee. Hypervelocity impact flash and plasma on electrically biased spacecraft surfaces. *International Journal of Impact Engineering*, 121:1–11, nov 2018. https://www.sciencedirect.com/science/article/pii/S0734743X17311429.

[35] Y. M. Hew, A. Goel, S. Close, and N. Lee. Hypervelocity impact flash and plasma on electrically biased spacecraft surfaces. *International Journal of Impact Engineering*, 121:1–11, 2018.

[36] Friedrich Hörz, Mark J. Cintala, Ronald P. Bernhard, and Thomas H. See. Dimensionally scaled penetration experiments to extract projectile sizes from space exposed surfaces. *International Journal of Impact Engineering*, 14(1):347–358, 1993.

[37] C. M. Huntington, A. Shimony, M. Trantham, C. C. Kuranz, D. Shvarts, C. A. Di Stefano, F. W. Doss, R. P. Drake, K. A. Flippo, D. H. Kalantar, S. R. Klein, J. L. Kline, S. A. Maclaren, G. Malamud, A. R. Miles, S. T. Prisbrey, K. S. Raman, B. A. Remington, H. F. Robey, W. C. Wan, and H. S. Park. Ablative stabilization of Rayleigh-Taylor instabilities resulting from a laser-driven radiative shock. *Physics of Plasmas*, 25(5):052118, may 2018. http://aip.scitation.org/doi/10.1063/1.5022179.

[38] Gregory J Hutchens. Approximate near-field blast theory: A generalized approach. *Journal of Applied Physics*, 88(6):3654–3658, 2000. https://doi.org/10.1063/1.1288785.

[39] I. H. Hutchinson. Ion collection by a sphere in a flowing plasma: I. Quasineutral. *Plasma Physics and Controlled Fusion*, 44(9):1953–1977, August 2002.

[40] I. H. Hutchinson. Ion collection by a sphere in a flowing plasma: 2. non-zero Debye length. *Plasma Physics and Controlled Fusion*, 45(8):1477–1500, July 2003.

[41] I. H. Hutchinson. Ion collection by a sphere in a flowing plasma: 3. Floating potential and drag force. *Plasma Physics and Controlled Fusion*, 47(1):71–87, December 2004.

[42] I. H. Hutchinson. Collisionless ion drag force on a spherical grain. *Plasma Physics and Controlled Fusion*, 48(2):185–202, January 2006.

[43] Andrii Ilienko. Continuous counterparts of Poisson and binomial distributions and their properties. *arXiv:1303.5990 [math]*, March 2013.

[44] N. L. Johnson, P. H. Krisko, J. C. Liou, and P. D. Anz-Meador. NASA's new breakup model of evolve 4.0. *Advances in Space Research*, 28(9):1377–1384, January 2001.

[45] Yuanyuan Ju, Qingming Zhang, Dongjiang Zhang, Renrong Long, Li Chen, Fenglei Huang, and Zizheng Gong. Theoretical model for plasma expansion generated by hypervelocity impact. *Physics of Plasmas*, 21(9):92112, 2014. https://doi.org/10.1063/1.4895592.

[46] Yuanyuan Ju, Qingming Zhang, Dongjiang Zhang, Renrong Long, Li Chen, Fenglei Huang, and Zizheng Gong. Theoretical model for plasma expansion generated by hypervelocity impact. *Physics of Plasmas*, 21(9):092112, 2014.

[47] Toshihiko Kadono and Akira Fujiwara. Observation of expanding vapor cloud generated by hypervelocity impact. *Journal of Geophysical Research E: Planets*, 101(E11):26097–26109, nov 1996. http://doi.wiley.com/10.1029/96JE02795.

[48] Daniel Kapitan and D. W Coutts. The dynamic properties of shock-waves formed during laser ablation at sub-atmospheric pressures. *Europhysics Letters*, 57(2):205–211, jan 2002. http://stacks.iop.org/0295-5075/57/i=2/a=205?key=crossref.d21ccc2c3ea10208742a872722d73062.

[49] R. V. Kennedy and J. E. Allen. The floating potential of spherical probes and dust grains. II: Orbital motion theory. *Journal of Plasma Physics*, 69(6):485–506, 2003.

[50] S. A. Khrapak. Ion drag force in complex plasmas. *Physical Review E*, 66(4), 2002.

[51] V. F. Kovalev and V. Yu. Bychenkov. Analytic solutions to the vlasov equations for expanding plasmas. *Physical Review Letters*, 90(18):185004, May 2003.

[52] V. F. Kovalev, V. Yu. Bychenkov, and V. T. Tikhonchuk. Particle dynamics during adiabatic expansion of a plasma bunch. *Journal of Experimental and Theoretical Physics*, 95(2):226–241, August 2002.

[53] C C Kuranz, R P Drake, E C Harding, M J Grosskopf, H F Robey, B A Remington, M J Edwards, A R Miles, T S Perry, B E Blue, T Plewa, N C Hearn, J P Knauer, D Arnett, and D R Leibrandt. Two-dimensional blast-wave-driven Rayleigh-Taylor instability: Experiment and simulation. *Astrophysical Journal*, 696(1):749–759, 2009. http://drakelab.engin.umich.edu/Papers/148{_}Two-DimensionalBlast-Wave-Driven.pdf.

[54] Kosuke Kurosawa, Yoichi Nagaoka, Hiroki Senshu, Koji Wada, Sunao Hasegawa, Seiji Sugita, and Takafumi Matsui. Dynamics of hypervelocity jetting during oblique impacts of spherical projectiles investigated via ultrafast imaging. *Journal of Geophysical Research E: Planets*, 120(7):1237–1251, jul 2015. http://doi.wiley.com/10.1002/2014JE004730.

[55] James G Laframboise. Theory of spherical and cylindrical Langmuir probes in a collisionless, Maxwellian plasma at rest. Technical report, TORONTO UNIV DOWNSVIEW (ONTARIO) INST FOR AEROSPACE STUDIES, 1966.

[56] N. Lee, S. Close, D. Lauben, I. Linscott, A. Goel, T. Johnson, J. Yee, A. Fletcher, R. Srama, S. Bugiel, A. Mocker, P. Colestock, and S. Green. Measurements of freely-expanding plasma from hypervelocity impacts. *International Journal of Impact Engineering*, 44:40–49, 2012. http://sess.stanford.edu/sites/default/files/IJIE2012-Measurementsoffreely-expandingplasmafromhypervelocityimpacts.pdf.

[57] Nicolas Lee, Sigrid Close, Ashish Goel, David Lauben, Ivan Linscott, Theresa Johnson, David Strauss, Sebastian Bugiel, Anna Mocker, and Ralf Srama. Theory and experiments characterizing hypervelocity impact plasmas on biased spacecraft materials. *Physics of Plasmas*, 20(3):032901, mar 2013. http://aip.scitation.org/doi/10.1063/1.4794331.

[58] Nicolas Lee, Sigrid Close, Ashish Goel, David Lauben, Ivan Linscott, Theresa Johnson, David Strauss, Sebastian Bugiel, Anna Mocker, and Ralf Srama. Theory and experiments characterizing hypervelocity impact plasmas on biased spacecraft materials. *Physics of Plasmas*, 20(3):032901, 2013.

[59] Shang Fei Liu, Yasunori Hori, D. N.C. Lin, and Erik Asphaug. GIANT IMPACT: AN EFFICIENT MECHANISM for the DEVOLATILIZATION of SUPER-EARTHS. *Astrophys. J.*, 812(2):164, oct 2015. https://iopscience.iop.org/article/10.1088/0004-637X/812/2/164https://iopscience.iop.org/article/10.1088/0004-637X/812/2/164/meta.

[60] Yonggang Liu, X. San Liang, and Robert H. Weisberg. Rectification of the Bias in the Wavelet Power Spectrum. *Journal of Atmospheric and Oceanic Technology*, 24(12):2093–2102, December 2007.

[61] J. D. Martin, M. Coppins, and G. F. Counsell. Motion and lifetime of dust grains in a tokamak plasma. *Journal of Nuclear Materials*, 337-339:114–118, 2005.

[62] D Masotti and A Costanzo. Start-up solutions for ultra-low power RF harvesting scenarios. In *2015 IEEE MTT-S International Conference on Numerical Electromagnetic and Multiphysics Modeling and Optimization (NEMO)*, pages 1–3, Ottowa, ON, Canada, aug 2015. IEEE. http://ieeexplore.ieee.org/document/7415021/.

[63] Diego Masotti, Alessandra Costanzo, Paolo Francia, Matteo Filippi, and Aldo Romani. A Load-Modulated Rectifier for RF Micropower Harvesting With Start-Up Strategies. *IEEE Transactions on Microwave Theory and Techniques*, 62(4):994–1004, apr 2014. http://ieeexplore.ieee.org/document/6742616/.

[64] N. McBride and J. a m McDonnell. Meteoroid impacts on spacecraft:: Sporadics, streams, and the 1999 Leonids. *Planetary and Space Science*, 47(8):1005–1013, 1999.

[65] N. McBride and J. A.M. McDonnell. Meteoroid impacts on spacecraft: Sporadics, streams, and the 1999 Leonids. *Planetary and Space Science*, 47(8-9):1005–1013, aug 1999.

[66] Jonathan M Mihaly, Jonathan D Tandy, A J Rosakis, M A Adams, and D Pullin. Pressure-Dependent, Infrared-Emitting Phenomenon in Hypervelocity Impact. *Journal of Applied Mechanics*, 82(1):011004, 2015. http://www.asme.org/about-asme/terms-of-use.

[67] A. R. Miles. Bubble merger model for the nonlinear Rayleigh-Taylor instability driven by a strong blast wave. *Physics of Plasmas*, 11(11):5140–5155, nov 2004. http://aip.scitation.org/doi/10.1063/1.1790498.

[68] P. Mora. Collisionless expansion of a gaussian plasma into a vacuum. *Physics of Plasmas*, 12(11):1–8, nov 2005. http://aip.scitation.org/doi/10.1063/1.2134768.

[69] H. M. Mott-Smith and Irving Langmuir. The Theory of Collectors in Gaseous Discharges. *Physical Review*, 28(4):727–763, October 1926.

[70] Akiko M. Nakamura, Akira Fujiwara, and Toshihiko Kadono. Velocity of finer fragments from impact. *Planetary and Space Science*, 42(12):1043–1052, 1994.

[71] Masahiro Nishida, Koichi Hayashi, Junichi Nakagawa, and Yoshitaka Ito. Influence of temperature on crater and ejecta size following hypervelocity impact of aluminum alloy spheres on thick aluminum alloy targets. *International Journal of Impact Engineering*, 42:37–47, April 2012.

[72] Masahiro Nishida, Yasuyuki Hiraiwa, Koichi Hayashi, and Sunao Hasegawa. Scaling laws for size distribution of fragments resulting from hypervelocity impacts of aluminum alloy spherical projectiles on thick aluminum alloy targets: Effects of impact velocity and projectile diameter. *International Journal of Impact Engineering*, 109:400–407, 2017.

[73] Masahiro Nshida, Naoto M Iyokawa, Koichi H Ayashi, Pauline F Aur, and Yasuhiro A Kahoshi. Influence of Temperature on Ejecta Size Resulting from Hypervelocity Impacts of Aluminum Alloy Spheres on Thick Aluminum Alloy Targets. pages 2–5, 2017. https://conference.sdo.esoc.esa.int/proceedings/sdc6/paper/91/SDC6-paper91.pdf.

[74] Andrew Nuttall, Mykel Kochenderfer, and Sigrid Close. Detection of hypervelocity impact radio frequency pulses through prior constrained source separation. *Radio Science*, 51(10):1660–1675, oct 2016. http://doi.wiley.com/10.1002/2016RS006108.

[75] A. Yu Pigarov, S. I. Krasheninnikov, T. K. Soboleva, and T. D. Rognlien. Dust-particle transport in tokamak edge plasmas. *Physics of Plasmas*, 12(12):122508, 2005.

[76] S. Ratynskaia, P. Tolias, I. Bykov, D. Rudakov, M. De Angeli, L. Vignitchouk, D. Ripamonti, G. Riva, S. Bardin, H. van der Meiden, J. Vernimmen, K. Bystrov, and G. De Temmerman. Interaction of adhered metallic dust with transient plasma heat loads. *Nuclear Fusion*, 56(6):066010, May 2016.

[77] I. L. Semenov, S. A. Khrapak, and H. M. Thomas. Approximate expression for the electric potential around an absorbing particle in isotropic collisionless plasma. *Physics of Plasmas*, 22(5):053704, May 2015.

[78] Gil Shohet, Ben Estacio, Isaac Matthews, Sean Young, Nicolas Lee, and Sigrid Close. Microscopic ejecta measurements from hypervelocity imapcts on aluminum and powdered regolith targets. *International Journal of Impact Engineering*, 152:103840, June 2021.

[79] P. K. Shukla and A. A. Mamun. *Introduction to Dusty Plasma Physics*. Series in Plasma Physics. IOP Publishing, Bristol, 2002.

[80] R. D. Smirnov, A. Yu Pigarov, M. Rosenberg, S. I. Krasheninnikov, and D. A. Mendis. Modelling of dynamics and transport of carbon dust particles in tokamaks. *Plasma Physics and Controlled Fusion*, 49(4):347, 2007.

[81] M. S. Sodha and S Guha. Advances in Plasma Physics. volume 4. Wiley, New York, 1971.

[82] Tolga Soyata, Lucian Copeland, and Wendi Heinzelman. RF Energy Harvesting for Embedded Systems: A Survey of Tradeoffs and Methodology. *IEEE Circuits and Systems Magazine*, 16(1):22–57, 2016. http://ieeexplore.ieee.org/document/7404333/.

[83] P. C. Stangeby. *The Plasma Boundary of Magnetic Fusion Devices*. Taylor & Francis, January 2000.

[84] Yasuhiko Takagi, Hitoshi Mizutani, and Shin-Ichi Kawakami. Impact fragmentation experiments of basalts and pyrophyllites. *Icarus*, 59(3):462–477, September 1984.

[85] Xian-Zhu Tang and Gian Luca Delzanno. Orbital-motion-limited theory of dust charging and plasma response. *Physics of Plasmas*, 21(12):123708, 2014.

[86] P. Tarantino, A. Goel, A. Corso, N. Lee, and S. Close. An electrostatic method to model the expansion of hypervelocity impact plasma on positively biased surfaces. *Physics of Plasmas*, 25(9):092103, September 2018.

[87] Geoffrey Ingram Taylor. The instability of liquid surfaces when accelerated in a direction perpendicular to their planes. I. *Proceedings of the Royal Society of London. Series A. Mathematical and Physical Sciences*, 201(1065):192–196, mar 1950. http://www.royalsocietypublishing.org/doi/10.1098/rspa.1950.0052.

[88] Christopher Torrence and Gilbert P. Compo. A Practical Guide to Wavelet Analysis. *Bulletin of the American Meteorological Society*, 79(1):61–78, January 1998.

[89] A. A. Uglov and A. G. Gnedovets. Effect of particle charging on momentum and heat transfer from rarefied plasma flow. *Plasma Chemistry and Plasma Processing*, 11(2):251–267, June 1991.

[90] L. Vignitchouk, G. L. Delzanno, P. Tolias, and S. Ratynskaia. Electron reflection effects on particle and heat fluxes to positively charged dust subject to strong electron emission. *Physics of Plasmas*, 25(6):063702, June 2018.

[91] L. Vignitchouk, S. Ratynskaia, M. Kantor, P. Tolias, M. De Angeli, H. van der Meiden, J. Vernimmen, F. Brochard, A. Shalpegin, E. Thorén, and J.-P. Banon. Validating heat balance models for tungsten dust in cold dense plasmas. *Plasma Physics and Controlled Fusion*, 60(11):115002, September 2018.

[92] L. Vignitchouk, S. Ratynskaia, P. Tolias, R. A. Pitts, G. De Temmerman, M. Lehnen, and D. Kiramov. Survival and in-vessel redistribution of beryllium droplets after ITER disruptions. *Nuclear Fusion*, 58(7):076008, May 2018.

[93] J. M. Walsh, R. G. Shreffler, and F. J. Willig. Limiting conditions for jet formation in high velocity collisions. *J. Appl. Phys.*, 24(3):349–359, mar 1953. http://aip.scitation.org/doi/10.1063/1.1721278.

[94] Xiaoshuai Wei, Juhua Liu, and Yunliang Long. Printed Log-Periodic Monopole Array Antenna with a Simple Feeding Structure. *IEEE Antennas and Wireless Propagation Letters*, 17(1):58–61, 2018.

[95] E. C. Whipple. Potentials of surfaces in space. *Reports on Progress in Physics*, 44(11):1197, November 1981.

[96] C. T. N. Willis, M. Coppins, M. Bacharis, and J. E. Allen. The effect of dust grain size on the floating potential of dust in a collisionless plasma. *Plasma Sources Science and Technology*, 19(6):065022, November 2010.

[97] C. T. N. Willis, M. Coppins, M. Bacharis, and J. E. Allen. Floating potential of large dust grains in a collisionless flowing plasma. *Physical Review E*, 85(3):036403, March 2012.

[98] Christopher Thomas Nigel Willis. *Dust in Stationary and Flowing Plasmas*. PhD Thesis, Imperial College London, November 2011.

[99] Xianfan Xu and David A. Willis. Non-Equilibrium Phase Change in Metal Induced by Nanosecond Pulsed Laser Irradiation. *Journal of Heat Transfer*, 124(2):293–298, November 2001.

[100] Sean Alden Quigg Young, Nicolas Lee, Benjamin Estacio, Isaac Matthews, Gil Shohet, Reid Bassette, Somrita Banerjee, and Sigrid Close. Electric Field Polarization of Electromagnetic Radiation from Micrometeoroid and Dust Impacts on Spacecraft. AGU, dec 2019.

[101] Jinhai Zhang, Jinlai Hao, Xu Zhao, Shuqin Wang, Lianfeng Zhao, Weimin Wang, and Zhenxing Yao. Restoration of clipped seismic waveforms using projection onto convex sets method. *Scientific Reports*, 6(1):39056, dec 2016. http://dx.doi.org/10.1038/srep39056http://www.nature.com/articles/srep39056.

[102] Kai Zhang, Renrong Long, Qingming Zhang, Yijiang Xue, and Yuanyuan Ju. Flash characteristics of plasma induced by hypervelocity impact. *Physics of Plasmas*, 23(8):083519, 2016.